Review & Perspectives

Active Polarized Proton Target

M. Biroth for the A2-Collaboration
Institute of Nuclear Physics, Mainz, Germany

A2 STRONG 2020 MAMI MAINZER MIKROTRON SFB 1044 THE LOW-ENERGY FRONTIER OF THE STANDARD MODEL JOHANNES GUTENBERG UNIVERSITÄT MAINZ

Probing the Inner Proton Structure

Protons have a complex structure from quarks, gluons and virtual pions

$1.6\ \mathrm{GeV}$ electron accelerator Mainz Mikrotron

- Electron scattering (A1 Collaboration)
- Real photon scattering (A2 Collaboration)

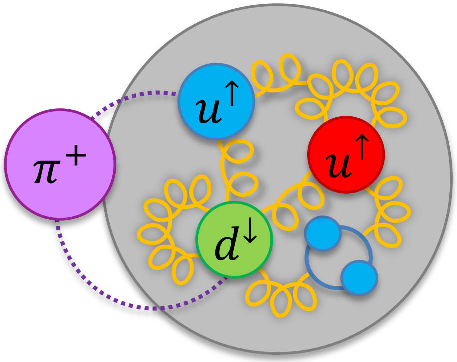

Probing the Inner Proton Structure

Protons have a complex structure from quarks, gluons and virtual pions

$1.6\ \mathrm{GeV}$ electron accelerator Mainz Mikrotron

- Electron scattering (A1 Collaboration)
- Real photon scattering (A2 Collaboration)

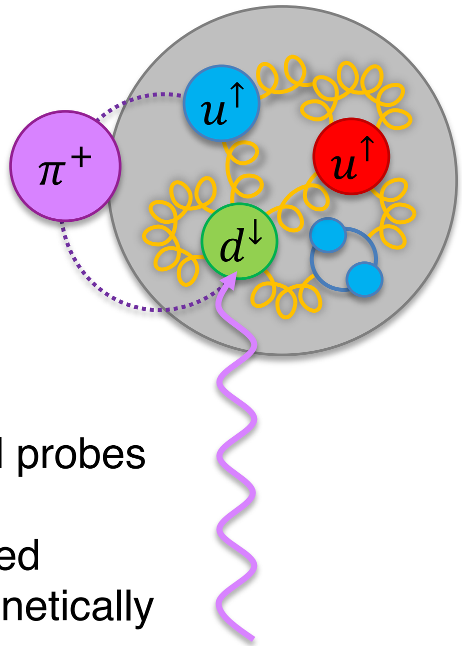

Real photons are ideal probes

- massless, uncharged
- interact electromagnetically

Probing the Inner Proton Structure

Protons have a complex structure from quarks, gluons and virtual pions

$1.6\ \mathrm{GeV}$ electron accelerator Mainz Mikrotron

- Electron scattering (A1 Collaboration)
- Real photon scattering (A2 Collaboration)

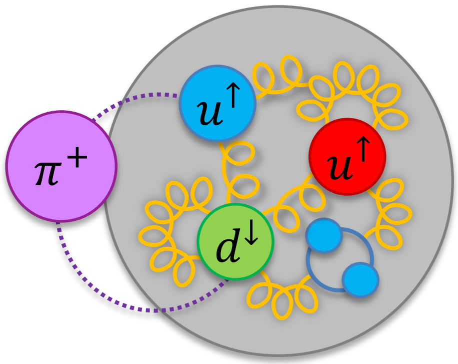

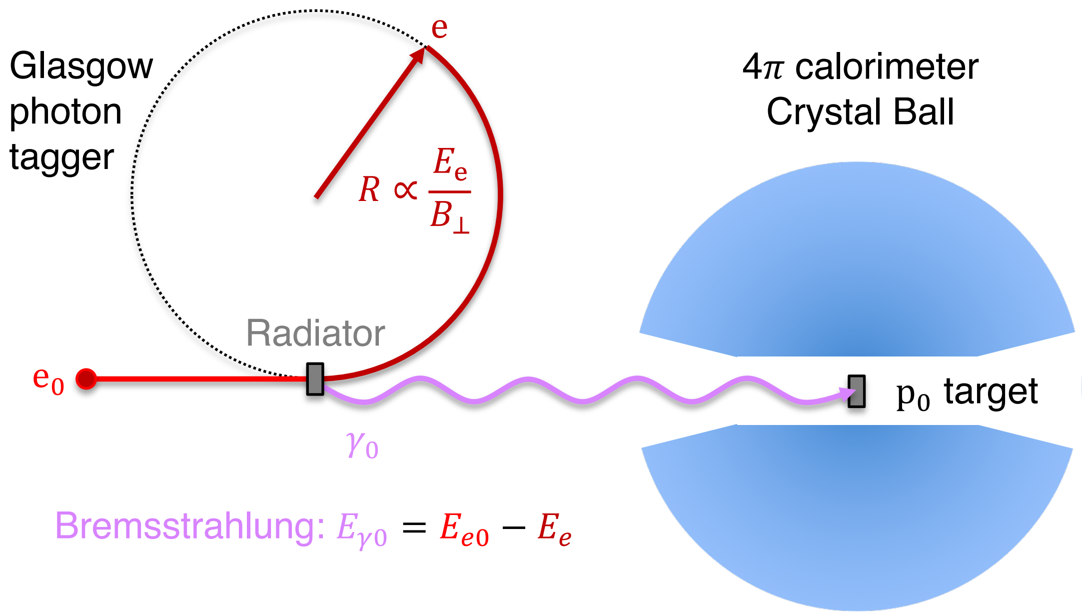

Possible experiments

- Unpolarized

Probing the Inner Proton Structure

Protons have a complex structure from quarks, gluons and virtual pions

$1.6\ \mathrm{GeV}$ electron accelerator Mainz Mikrotron

- Electron scattering (A1 Collaboration)
- Real photon scattering (A2 Collaboration)

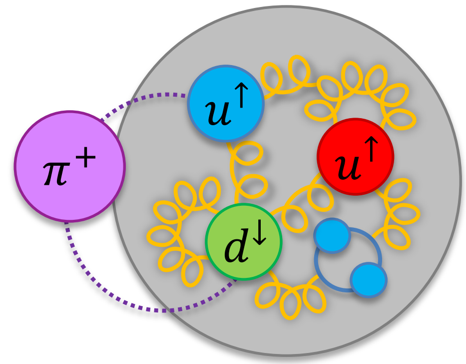

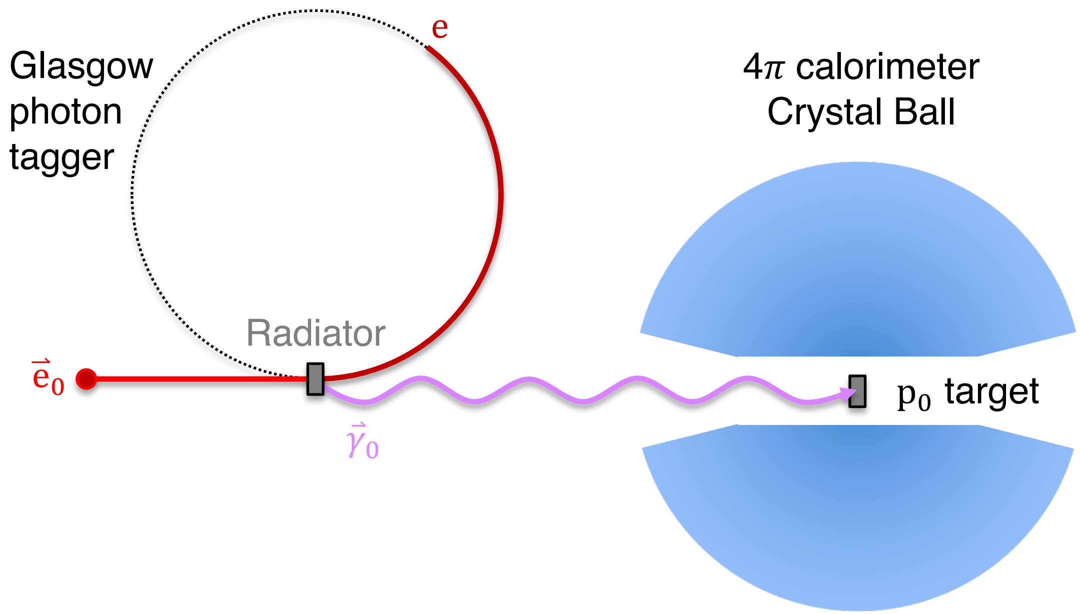

Possible experiments

- Unpolarized
- Polarized

Probing the Inner Proton Structure

Protons have a complex structure from quarks, gluons and virtual pions

$1.6\ \mathrm{GeV}$ electron accelerator Mainz Mikrotron

- Electron scattering (A1 Collaboration)
- Real photon scattering (A2 Collaboration)

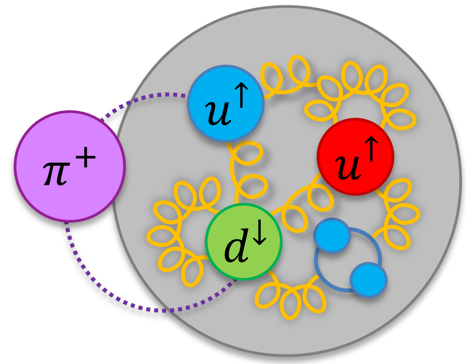

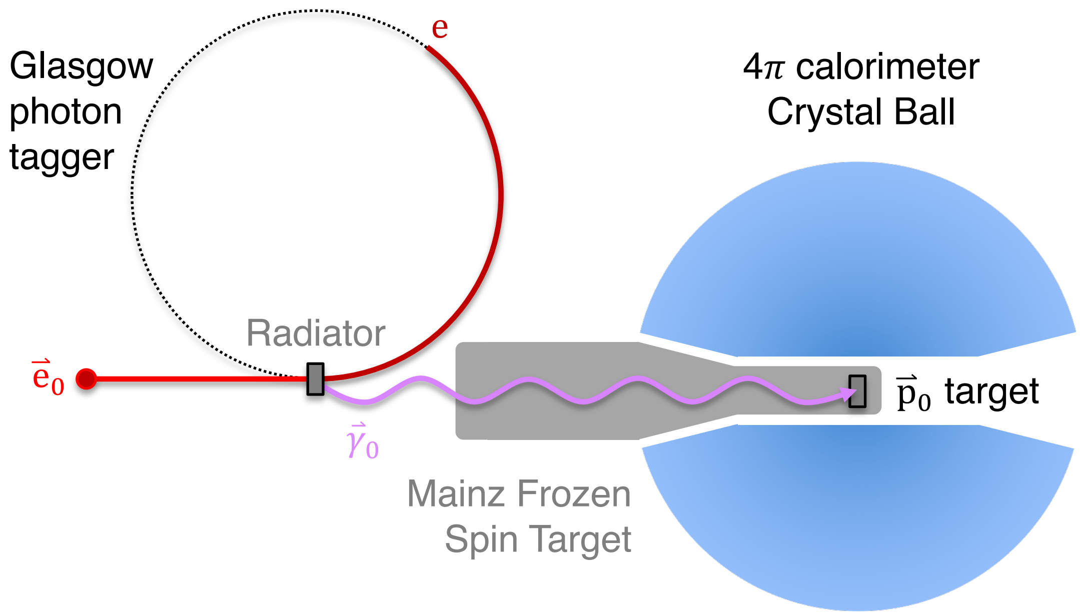

Possible experiments

- Unpolarized
- Polarized
- Double-polarized

Generation of Target Spin-polarization

- Spin states $|{\downarrow}\rangle$, $|{\uparrow}\rangle$ show (anti-)alignment in a magnetic field B
- Zeeman splitting ΔE leads to breakdown of the degeneracy

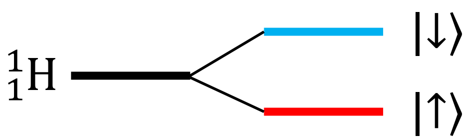

$$\Delta E = \hbar\, \gamma_{\mathrm{H}}\, B$$

(gyromagnetic ratio γ_{H})

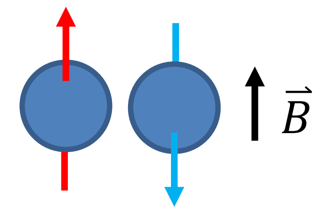

- Polarization P is the asymmetry of the occupied states N_s
- Thermal equilibrium population follows Boltzmann statistics

$$P = \frac{N_\uparrow - N_\downarrow}{N_\uparrow + N_\downarrow}$$

$$P_{\mathrm{TE}} = \tanh \frac{\Delta E}{2 k_{\mathrm{B}} T}$$

(Boltzmann const. k_{B})

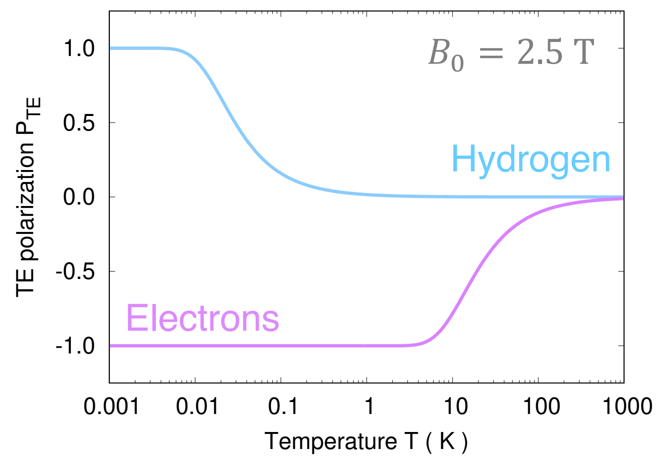

Solution: Dynamic Nuclear Polarization uses the high electron polarization to generate a high hydrogen polarization

Concept of Dynamic Nuclear Polarization

- Embedding of unpaired electron spins with density n
- Electron and hydrogen spins are super-hyperfinely coupled

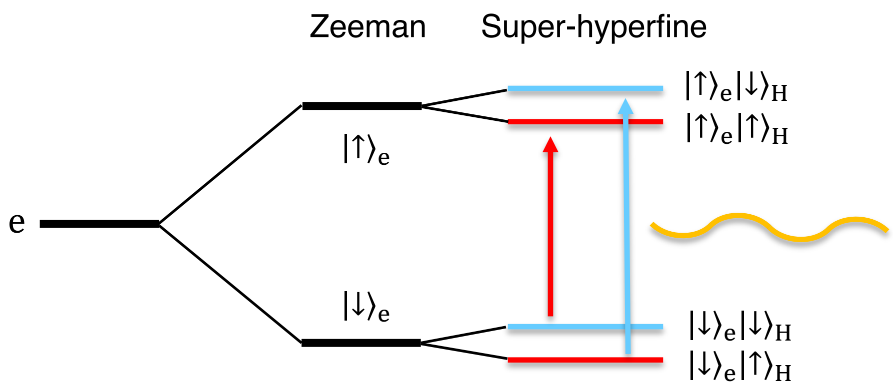

1. µWave irradiation ω_m excites transitions that induce coupled spin-flips

$$\omega_\mathrm{m}^{\pm} = (\gamma_\mathrm{e} \mp \gamma_\mathrm{H})\, B_0 = 2\pi \times \begin{cases} 70.0\ \mathrm{GHz} & + \\ 70.2\ \mathrm{GHz} & - \end{cases}$$

Gyromagnetic ratios of the electrons $\gamma_\mathrm{e} = g_\mathrm{e}/2\ e_0/m_\mathrm{e}$ and hydrogen $\gamma_\mathrm{H} = \kappa_\mathrm{p}\ e_0/m_\mathrm{p}$, magnetic field $B_0 = 2.5\ \mathrm{T}$

Maik Biroth, Institute of Nuclear Physics, Mainz, Germany
mbiroth@uni-mainz.de

Concept of Dynamic Nuclear Polarization

- Embedding of unpaired electron spins with density n
- Electron and hydrogen spins are super-hyperfinely coupled

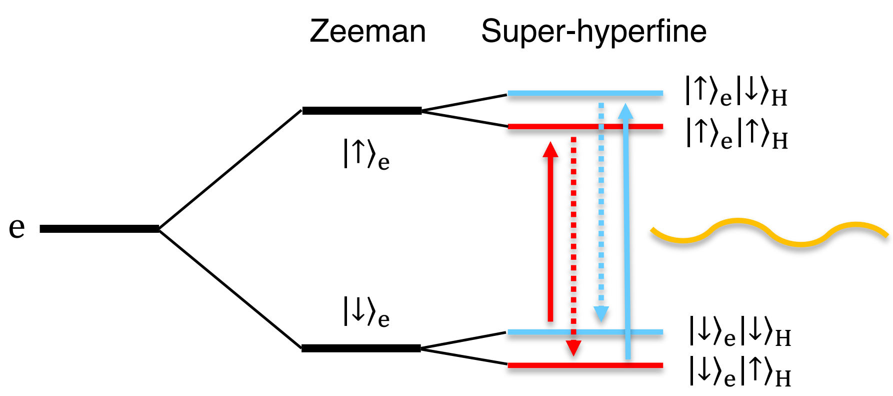

1. µWave irradiation ω_m excites transitions that induce coupled spin-flips

$$\omega_\mathrm{m}^{\pm} = (\gamma_\mathrm{e} \mp \gamma_\mathrm{H})\, B_0 = 2\pi \times \begin{cases} 70.0\ \mathrm{GHz} & + \\ 70.2\ \mathrm{GHz} & - \end{cases}$$

2. Electron spins relax during irradiation (dashed arrows)

Gyromagnetic ratios of the electrons $\gamma_\mathrm{e} = g_\mathrm{e}/2\ e_0/m_\mathrm{e}$ and hydrogen $\gamma_\mathrm{H} = \kappa_\mathrm{p}\ e_0/m_\mathrm{p}$, magnetic field $B_0 = 2.5\ \mathrm{T}$

Maik Biroth, Institute of Nuclear Physics, Mainz, Germany
mbiroth@uni-mainz.de

Concept of Dynamic Nuclear Polarization

- Embedding of unpaired electron spins with density n
- Electron and hydrogen spins are super-hyperfinely coupled

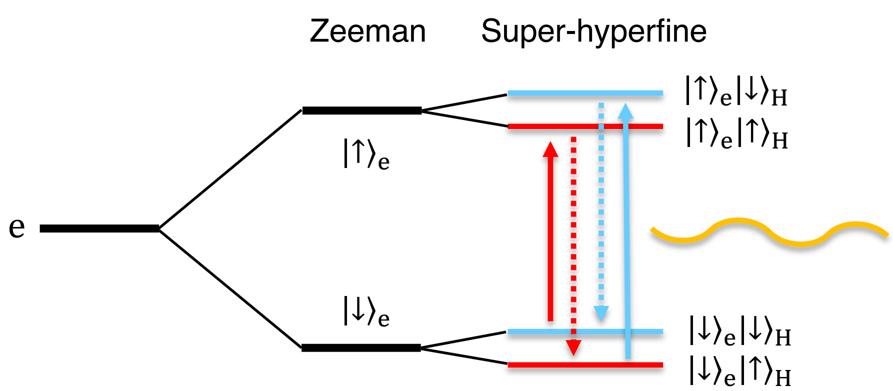

1. µWave irradiation ω_m excites transitions that induce coupled spin-flips

$$\omega_\mathrm{m}^{\pm} = (\gamma_\mathrm{e} \mp \gamma_\mathrm{H})\, B_0 = 2\pi \times \begin{cases} 70.0\ \mathrm{GHz} & + \\ 70.2\ \mathrm{GHz} & - \end{cases}$$

2. Electron spins relax during irradiation (dashed arrows)

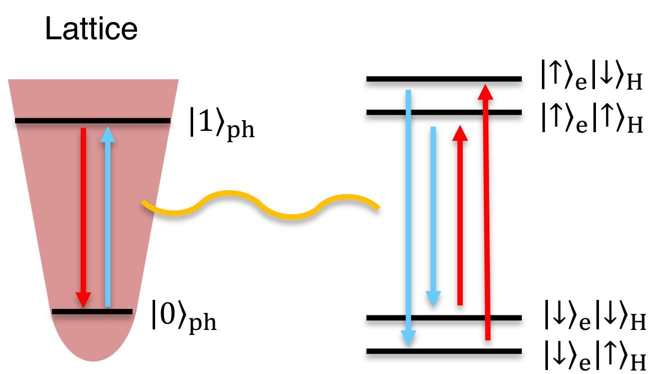

3. Polarization decays by phonon emission or absorption with the nuclear spin-lattice relaxation time τ_1 in the essential holding field B_HF

$$\tau_1 \propto \frac{1}{n} \frac{P_\mathrm{TE,e}^{1/4}}{1 - P_\mathrm{TE,e}^2} B_\mathrm{HF}^{3/4}$$

Gyromagnetic ratios of the electrons $\gamma_\mathrm{e} = (g_\mathrm{e}/2)\ e_0/m_\mathrm{e}$ and hydrogen $\gamma_\mathrm{H} = \kappa_\mathrm{p}\ e_0/m_\mathrm{p}$, magnetic field $B_0 = 2.5\ \mathrm{T}$

Maik Biroth, Institute of Nuclear Physics, Mainz, Germany
mbiroth@uni-mainz.de

Magnetic Fields for Transverse Target Polarization

The Mainz Frozen Spin Target provides 2 different fields:

High field B_0

- Superconducting solenoid, $\delta B_0/B_0 \leq 10^{-4}$
- Polarization build-up and measurement

Holding field B_{HF}

- Internal superconducting coil
- Saddle coil for transverse polarization

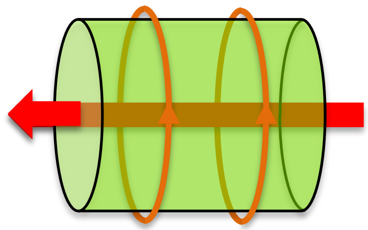

$\vec{B}_0 \coloneqq 2.5\ \mathrm{T} \times \vec{e}_z$

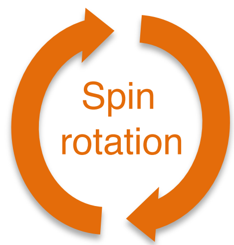

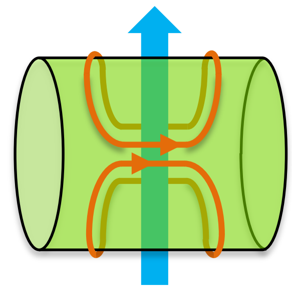

$\vec{B}_{\mathrm{HF}} \coloneqq 437.5\ \mathrm{mT} \times \vec{e}_x$

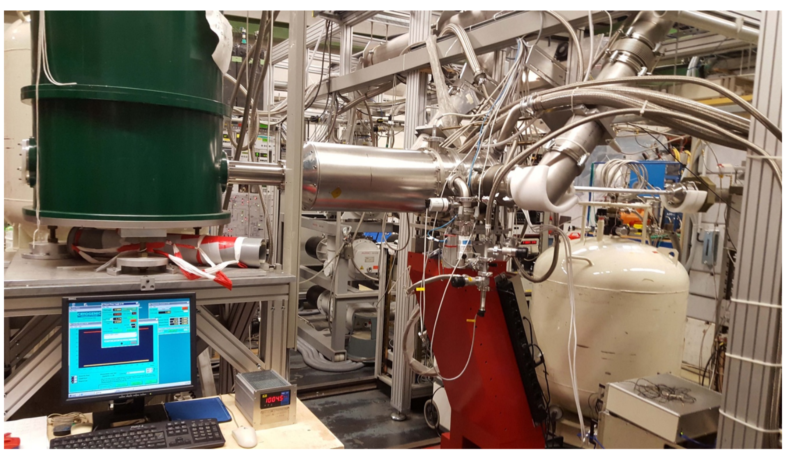

Motivation for the Active Polarized Proton Target

Standard setup of the Mainz Frozen Spin Target

- Dilution cryostat with thermal insulation
- Internal super-conducting holding coil
- Spin-polarizable target material

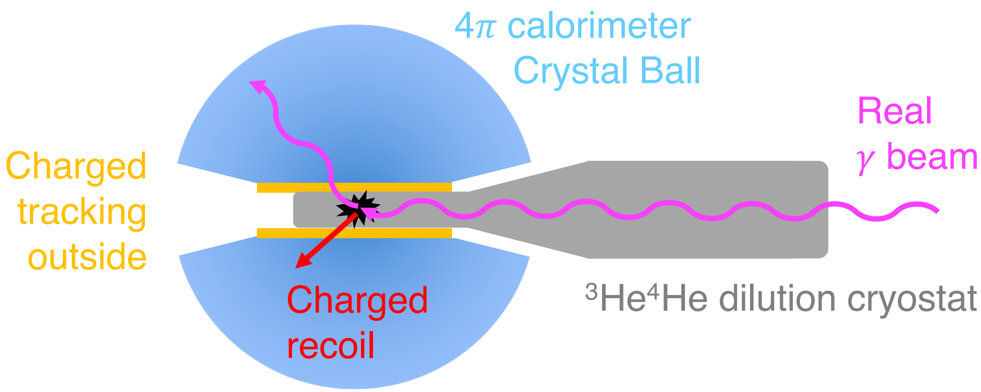

70 MeV threshold
for recoil protons

Kinetic energy of recoil protons
in Real Compton Scattering:

$$T_\mathrm{p} = E_{\gamma 0} - E_\gamma = \frac{Q^2}{2\,m_p}$$

Initial and final state photon energies $E_{\gamma 0}$, E_γ, proton mass m_p, square four-momentum transfer $Q^2 = -t$

Motivation for the Active Polarized Proton Target

Standard setup of the Mainz Frozen Spin Target

- Dilution cryostat with thermal insulation
- Internal super-conducting holding coil
- Spin-polarizable target material

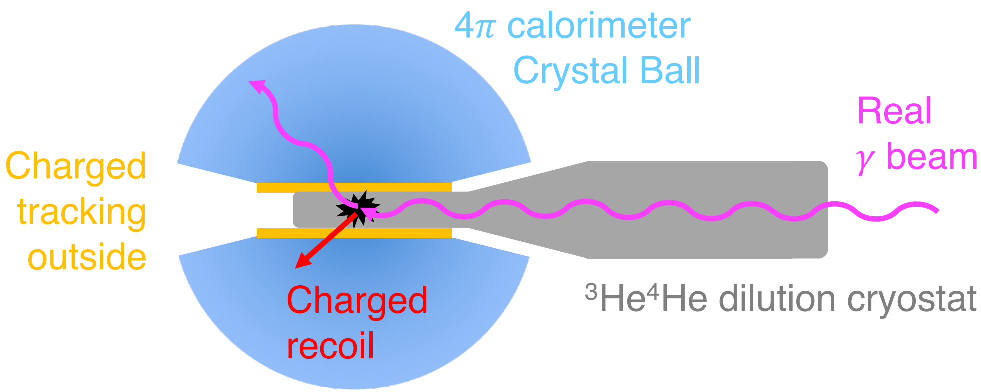

70 MeV threshold for recoil protons

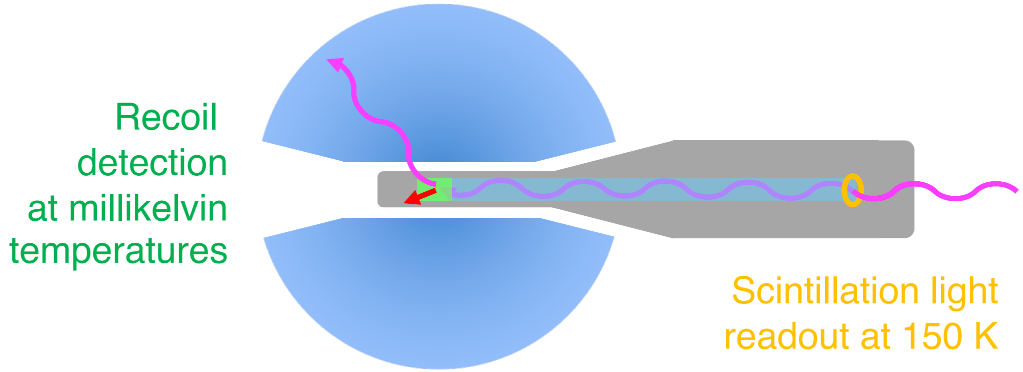

Solution: Replacing the target material by an internal spin-polarizable scintillation detector

Challenges in Combining Polarization and Scintillation

Spin-polarizable scintillating detector

- High degree of polarization / relaxation time
- High resolving power for energy / timing / angles

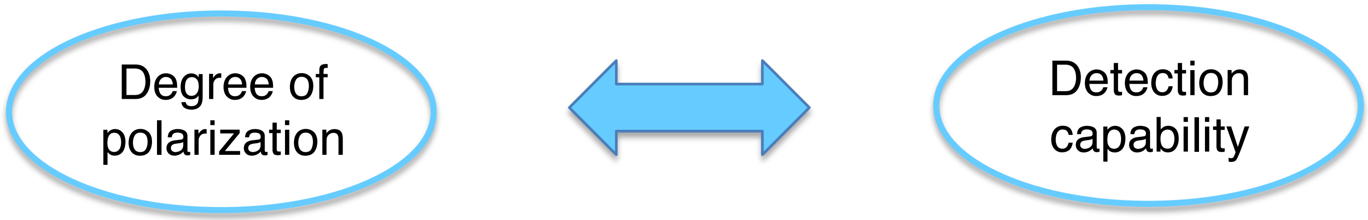

Minimum requirements for operation

- He-tightness under thermal cycling
- Minimum heat input / exchange
- Immunity to magnetic fields ~ 1 Tesla
- Tolerance to beam / µWave irradiation
- Acceptance of overall tiny dimensions

Concept of the Active Polarized Proton Target

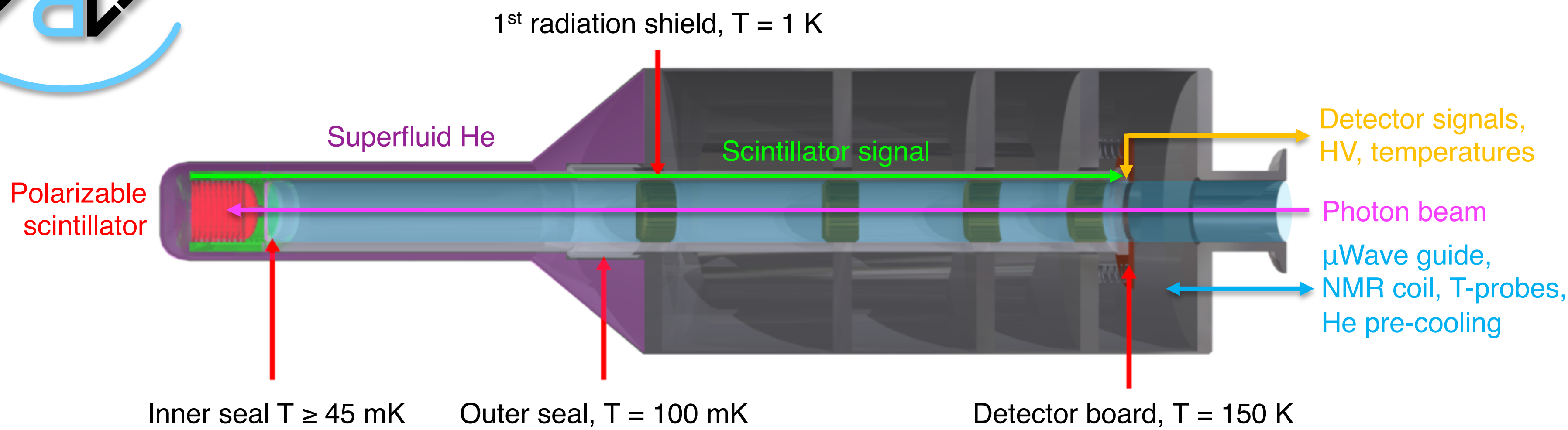

1. **Active target head**
   - Polarizable scintillator stack: Providing polarized hydrogen, emitting light for charged tracks
   - Light concentrating element: Distributing scintillation light into the beam / light guide tube

2. **Sealed beam / light guide tube**
   - Beam guide: Transport of the photon beam in vacuum in the inner volume
   - Light guide: Transport of the scintillation light between the surfaces inside the wall
   - Inner / outer seal: Separation of mixing chamber and beam vacuum, multiple feedthroughs

3. **Compensating detector board**
   - Optical detectors: Converting light to electric signals and distribute them to the amplifiers
   - Electronical compensation: Measuring the temperature for detector gain control
   - Mechanical compensation: Equalization of thermal contraction of the tube

4. **Custom frontend electronics and software**

Spin-polarizable Plastic Scintillator

Transparent base material with a high dilution factor

- Polystyrene C_8H_8, $d = 7.7\%$ (Butanol $C_4H_{10}O$, $d = 13.5\%$)

Standard scintillator components

- 1st scintillator: PPO / 2,5-Diphenyloxazole ($\lambda_{em} = 360$ nm)
- 2nd scintillator: Dimethyl-POPOP ($\lambda_{abs} = 360$ nm, $\lambda_{em} = 410$ nm)

Unpaired electron spins

- Doping with the paramagnetic free radical 4-Oxo-TEMPO
- Produced with 3 spin densities $n \in [1.5\,, 2.2\,, 3.0] \times 10^{19}\ \mathrm{cm}^{-3}$

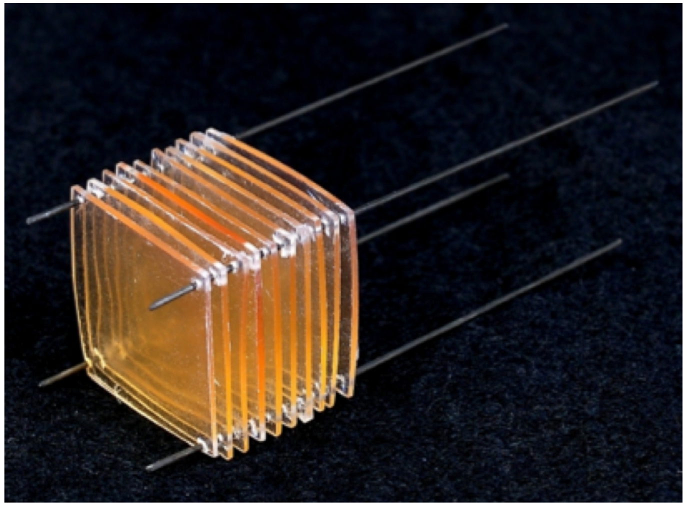

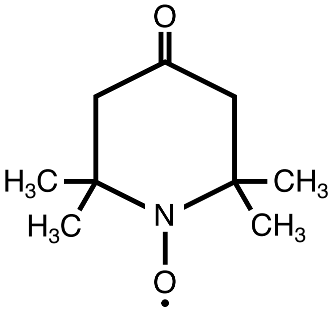

D. Von Maluski, R.R. Miskimen, et al. Polarizable Scintillator for Nuclear Targets. Technical report, Triangle Universities Nuclear Laboratory (TUNL), 2009

Dilution factor d = #hydrogen/#nucleon

Light Output of the Polarizable Scintillator

The electron radical density effects also the light output of the scintillator.

Component	Wavelength of max. absorption	Wavelength of max. emission
PPO/2,5-Diphenylloxazole	303 nm	358 nm
Dimethyl-POPOP	360 nm	411 nm

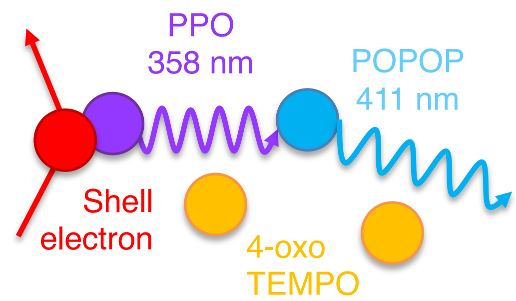

The radical deteriorates the quantum efficiency to 50% of a standard plastic scintillator

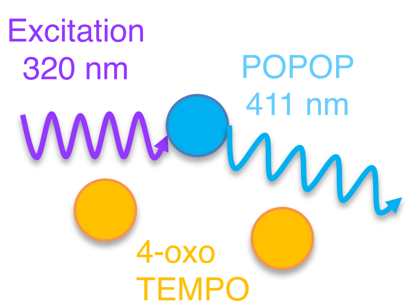

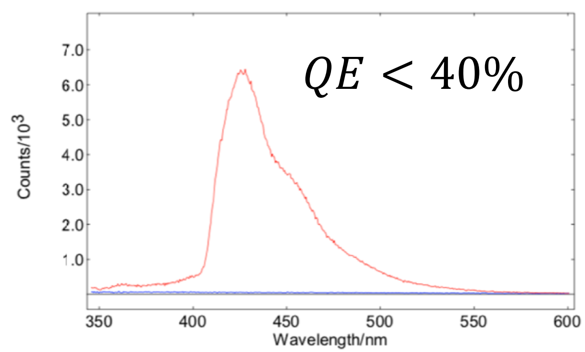

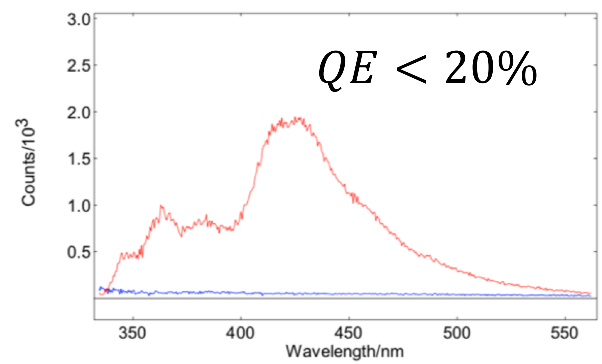

Light Output of the Polarizable Scintillator

The electron radical density effects also the light output of the scintillator.

Component	Wavelength of max. absorption	Wavelength of max. emission
PPO/2,5-Diphenylloxazole	303 nm	358 nm
Dimethyl-POPOP	360 nm	411 nm

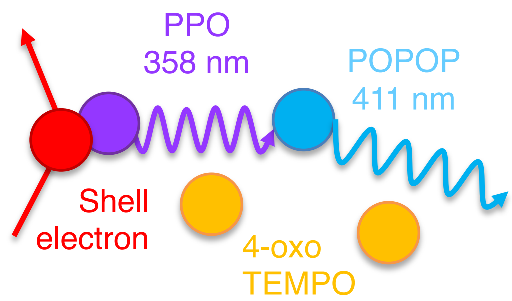

The radical deteriorates the quantum efficiency to 50% of a standard plastic scintillator or even lower, since wavelengths within the Stokes Shift does not excite the POPOP.

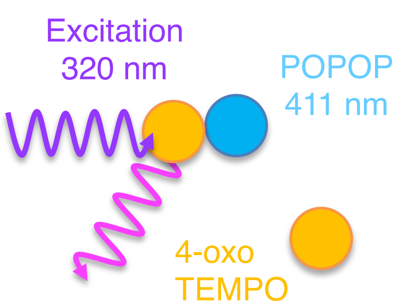

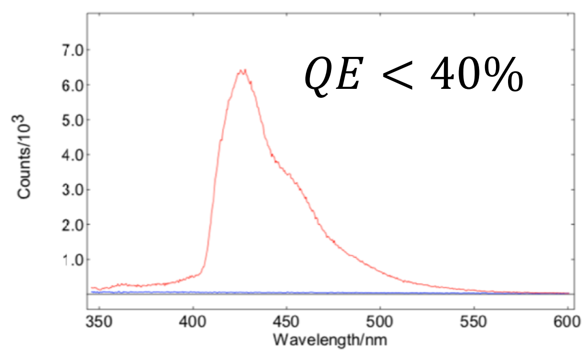

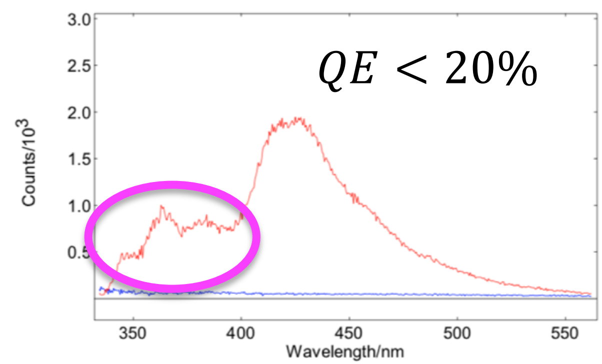

Light Concentrator Based on Wavelength Shifting

The electron radical density effects also the light output of the scintillator.

Component	Wavelength of max. absorption	Wavelength of max. emission
PPO/2,5-Diphenylloxazole	303 nm	358 nm
Dimethyl-POPOP	360 nm	411 nm
BC-482A (Saint-Gobain)	420 nm	494 nm

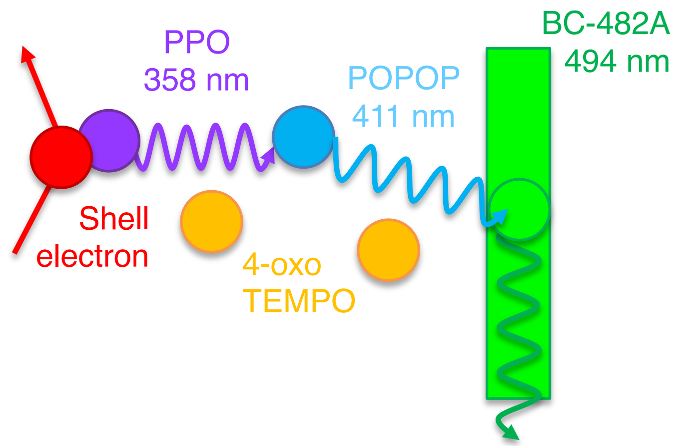

The WLS light concentrator consists of a hollow cylinder of wavelength-shifting material. The scintillation light is redistributed isotropically only if its wavelength matches the absorption spectrum.

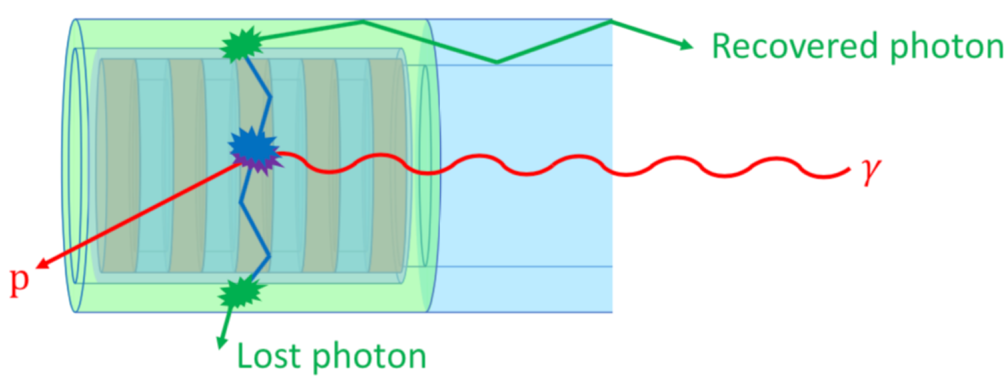

Light Concentrator Based on Wavelength Shifting

The electron radical density effects also the light output of the scintillator.

Component	Wavelength of max. absorption	Wavelength of max. emission
PPO/2,5-Diphenylloxazole	303 nm	358 nm
Dimethyl-POPOP	360 nm	411 nm
BC-482A (Saint-Gobain)	420 nm	494 nm

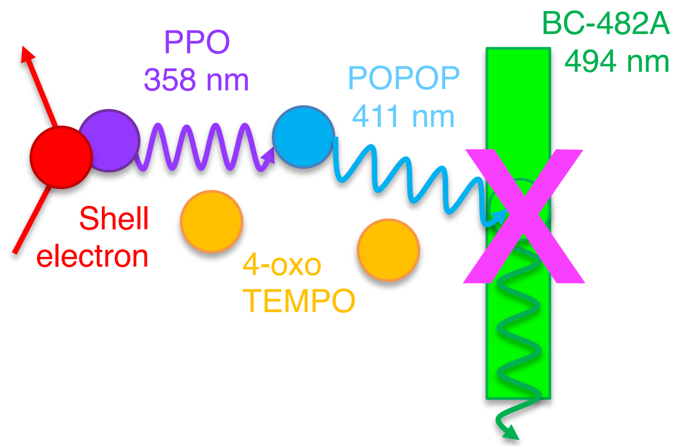

The WLS light concentrator consists of a hollow cylinder of wavelength-shifting material.
The scintillation light is redistributed isotropically only if its wavelength matches the absorption spectrum.

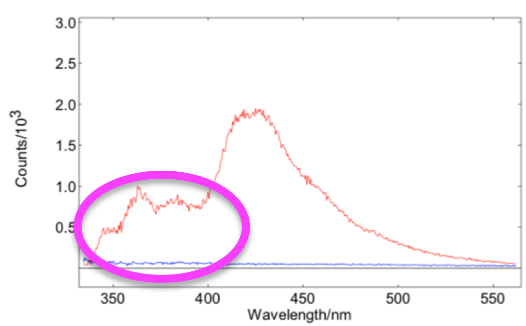

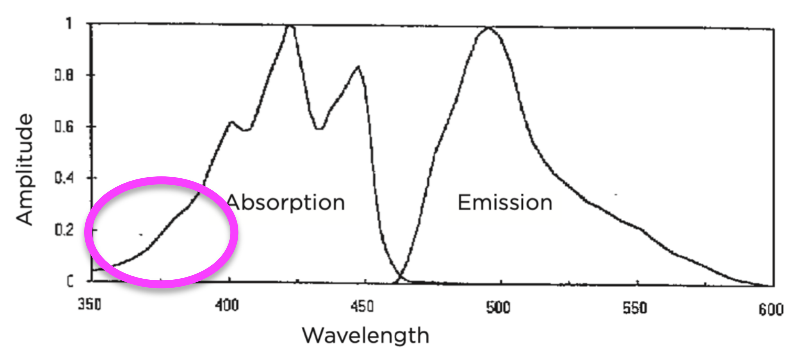

Light Concentrator Based on Total Reflexion

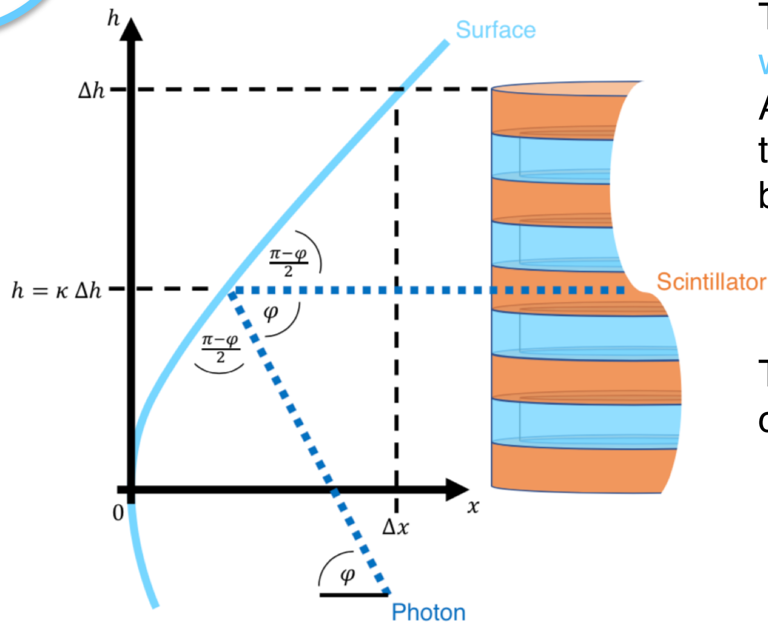

The light collection by a polished surface does only weak depend on the wavelength.
A linear interpolation between a straight track and traveling under $\varphi_{\text{tot}} = \sin^{-1} n^{-1}$ was selected as boundary condition for the incident angle φ.

$$\varphi = \varphi_{\text{tot}}(1-\kappa) + \frac{\pi}{2}\kappa = \sin^{-1} n^{-1} + \kappa \cos^{-1} n^{-1}$$

The surface parameterization was used for a computer-controlled manufacturing process.

The benefit in light collection efficiency is $+\,25\%$, already with standard plastic scintillator.

The increased outer diameter $26\text{mm} \rightarrow 38\text{mm}$ was problematic for mounting and cooling.

See: M. Biroth, et al., Design of the Mainz Active Polarized Proton Target, Proc. Sci. (PSTP 2015) 005, Refractive index of PMMA n

Active Target Operated in the Experiment

Photograph of the target part installed in the mixing chamber:

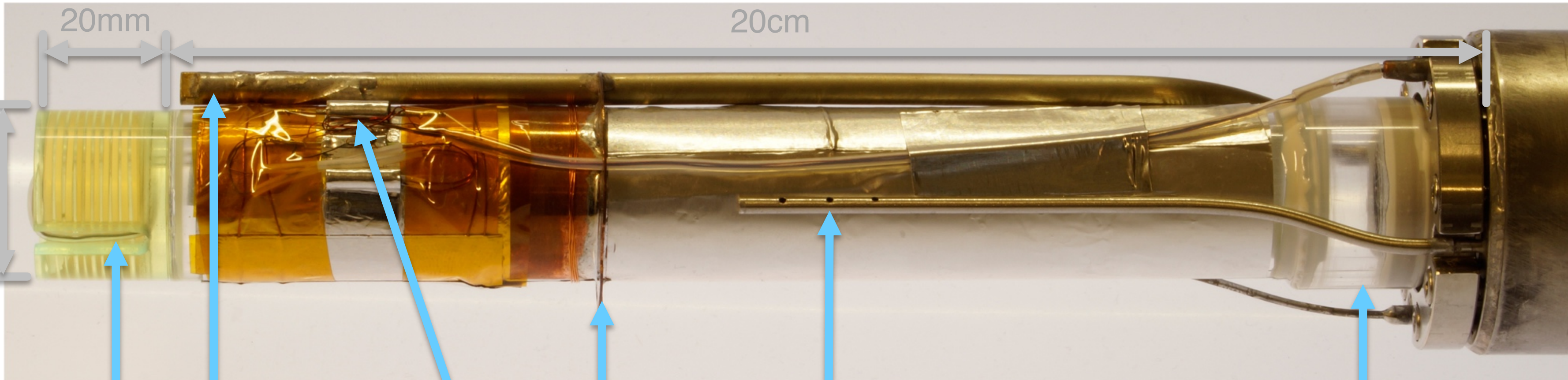

μWave guide with UHF tuner

Temperature probes

Outlet nozzle of the ^{4}He pre-cooling line

Outer He-vacuum seal and feedthrough

Target head with cooling slit and one-turn NMR saddle coil

μWave radiation shield

Active Target Operated in the Experiment

Photograph of the target part installed in the mixing chamber:

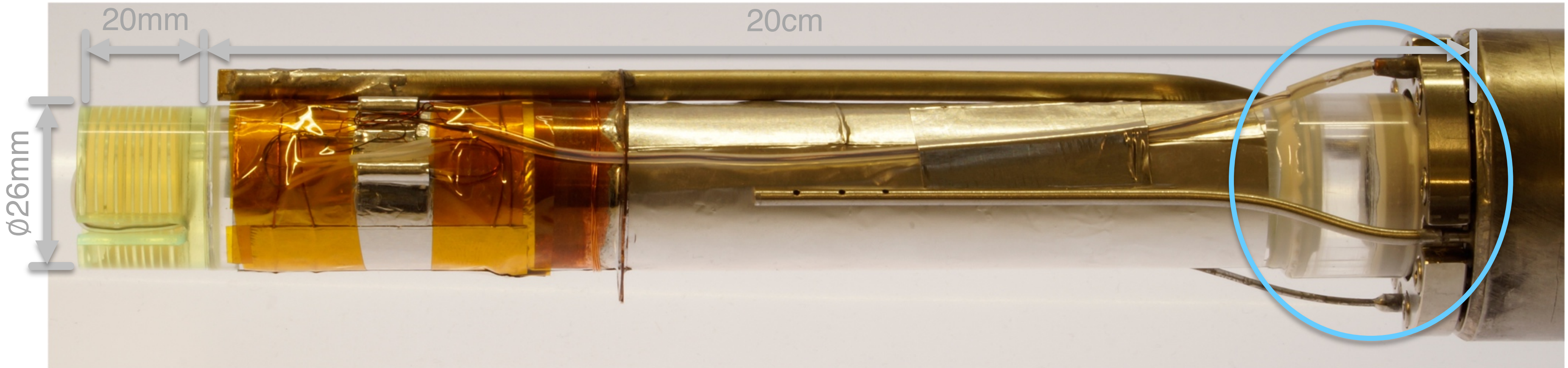

- Integral thermal expansion of PMMA : stainless steel (SS) is ×6

- Relaxation pod takes stress at the tube-flange connection

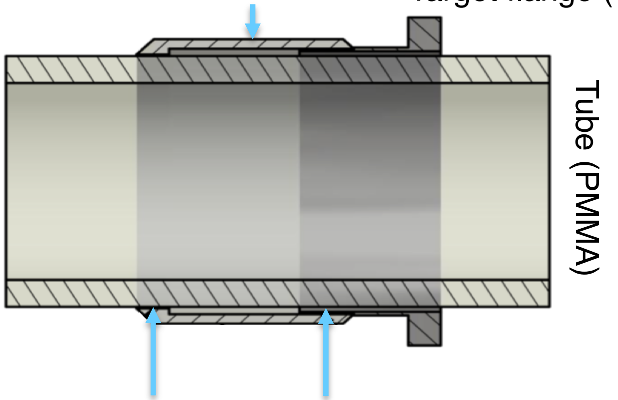

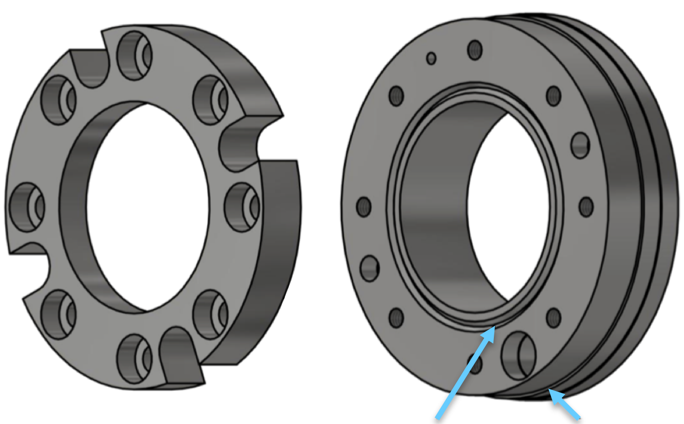

Modifications to the Beam / Light Guide Tube

Modification to the PMMA tube were necessary to enable dilution mode at $45\ \mathrm{mK}$.
Cooling-down took 5 days due to the low thermal conductivity of PMMA.

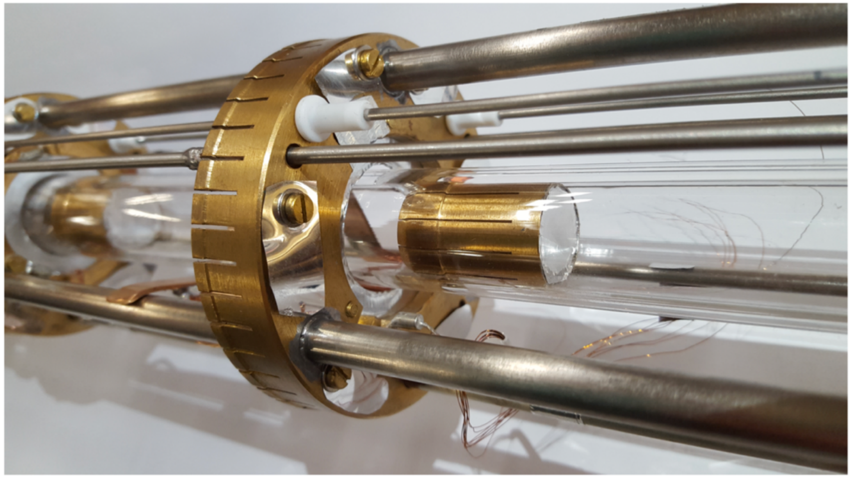

- Placing radiation shields in the beam path to block heat exchange $\dot{Q} \propto \varepsilon\, T^4$ (perfect mirror $\varepsilon = 0$, black body $\varepsilon = 1$).
- Setting thermal contacts by copper tape at the first radiation shield and by brass springs at the others.

Thermal radiation at temperature T follows the Stefan-Boltzmann law $\dot{Q} = \varepsilon\, A\, \sigma\, T^4$ with emission factor ε, area A, constant $\sigma = 56.7\ \mathrm{nW\,m^{-2}\,K^{-4}}$, thermal conductivity of PMMA $0.2\ \mathrm{W\,m^{-1}\,K^{-1}}$, glass $1\ \mathrm{W\,m^{-1}\,K^{-1}}$, SS $10\ \mathrm{W\,m^{-1}\,K^{-1}}$, copper $400\ \mathrm{W\,m^{-1}\,K^{-1}}$

Light Transport Inside the Beam / Light Guide Tube

- Monte Carlo simulation of single photons
- Ray tracing trough the $1.5\mathrm{m}$ light guide tube

Good path

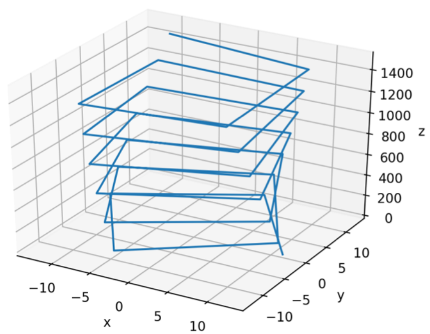

Bad path

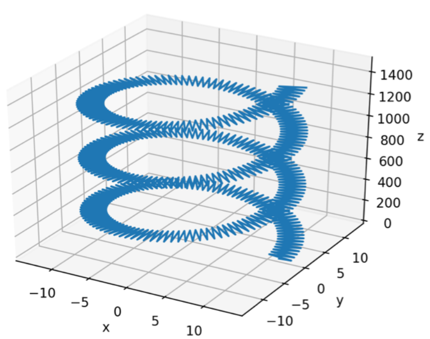

Material	Intensity I[L]		Attenuation λ / m	
	MC Sim.	Measured	MC Sim.	Measured
Borosilicate	36(1) %		1.47(4)	
PMMA	37(1) %		1.50(4)	

The intensity-weighted path lengths follow a Weibull distribution.

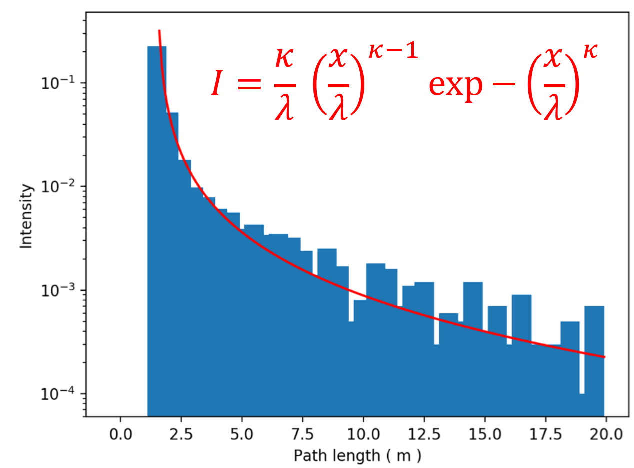

Refractive index of PMMA $n = 1.49$, refractive index of Borosilicate $n = 1.47$

Light Transport Inside the Beam / Light Guide Tube

- Monte Carlo simulation of single photons
- Ray tracing trough the $1.5\mathrm{m}$ light guide tube

Good path

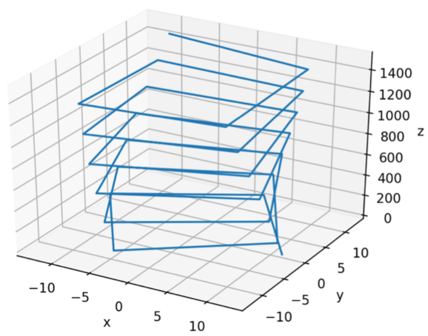

Bad path

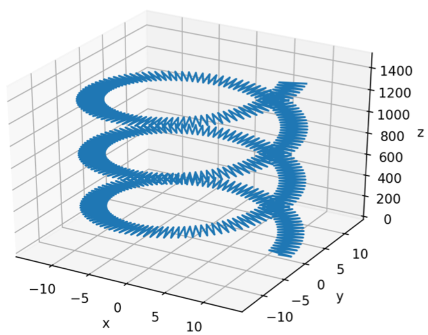

Material	Intensity $\mathrm{I[L]}$		Attenuation λ / m	
	MC Sim.	Measured	MC Sim.	Measured
Borosilicate	$36(1)$ %	$8.4(2)$ %	$1.47(4)$	$0.607(3)$
PMMA	$37(1)$ %	–	$1.50(4)$	–

The measurement of Borosilicate shows a drop in intensity by a factor of four because of imperfections in

- surface quality
- transparency

Scattering at the relaxation pod, the copper tape and at scratches from mounting lead to a further significant degradation of the energy resolution.

Refractive index of PMMA $n = 1.49$, refractive index of Borosilicate $n = 1.47$

Readout by the Compensating Detector Board

Mechanical compensation of the PMMA integral thermal contraction $\sim 1\%$.

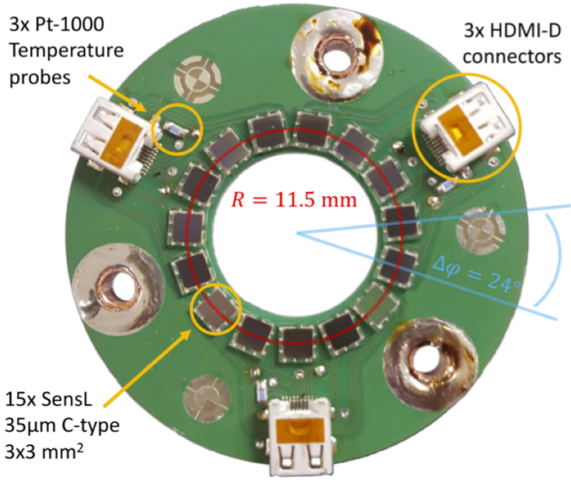

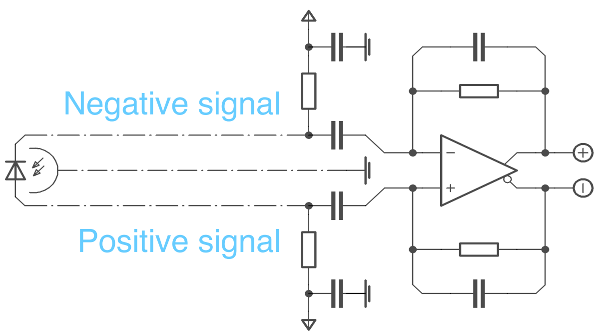

SiPM amplifiers: M. Biroth, et al., NIM A 787 (2015) 185-188

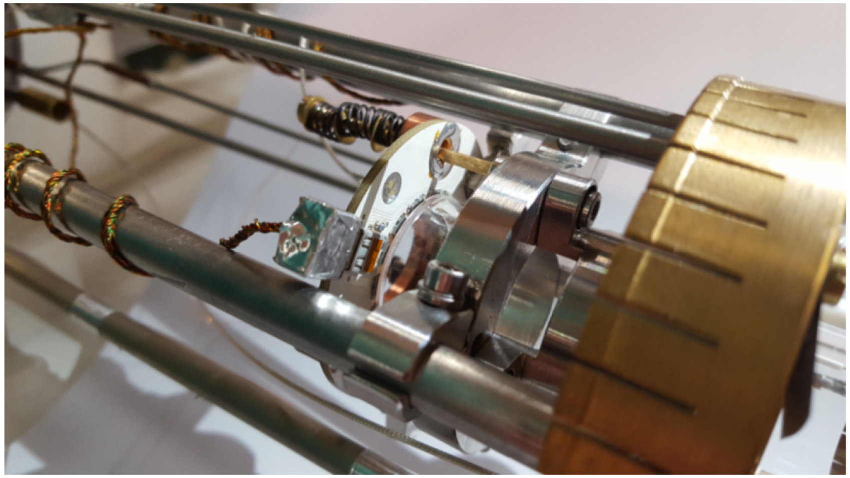

15 silicon photomultipliers

- Fully-differential signals
  - increasing signal-to-noise ratio $\times\sqrt{2}$
  - suppression of common-mode noise
- Individual floating shielding
  - avoids ground loops
- Tolerate long connections
  - reduction of the heat input

3 temperature probes

- Pt sensors with 4-wire readout
- Enable gain compensation

Stabilization of the Detector Gain and Energy Calculation

Constant pixel gain G control

- Radial interpolated temperature T_i
- Individual operational voltage V_i
  - Pixel capacitance C_{eff}
  - Breakdown voltage V_{BD}

$$G = C_{\text{eff}}[T_i]\,(V_i - V_{\text{BD}}[T_i]) := \text{const.}$$

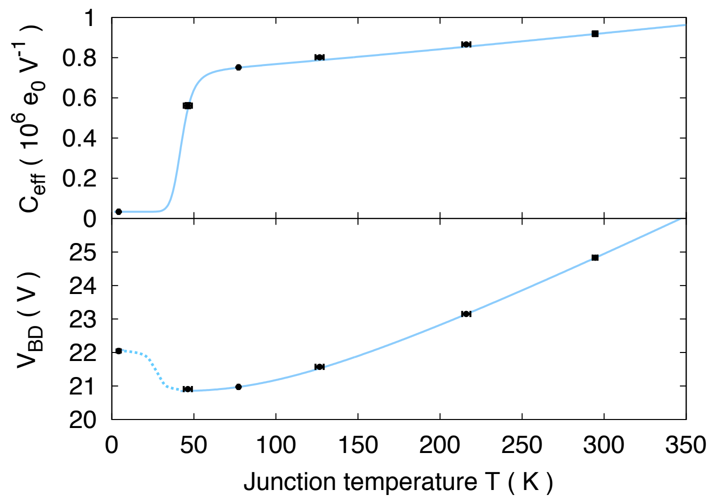

Individual pixel gain G_i calibration

- For each run:
  - Pixel gain G_i, pedestal charge Q_i^0 by curve-fitting
- For each event k:
  - Fired pixels $n_{k,i}$ with respect to the charge $Q_{k,i}$
  - Energy sum E_k as total sum of fired pixels

$$n_{k,i} = \left\lfloor \frac{Q_{k,i} - Q_i^0}{G_i} + \frac{1}{2} \right\rfloor \qquad E_k = \sum_i n_{k,i}$$

QDC spectrum of detector $i = 0$

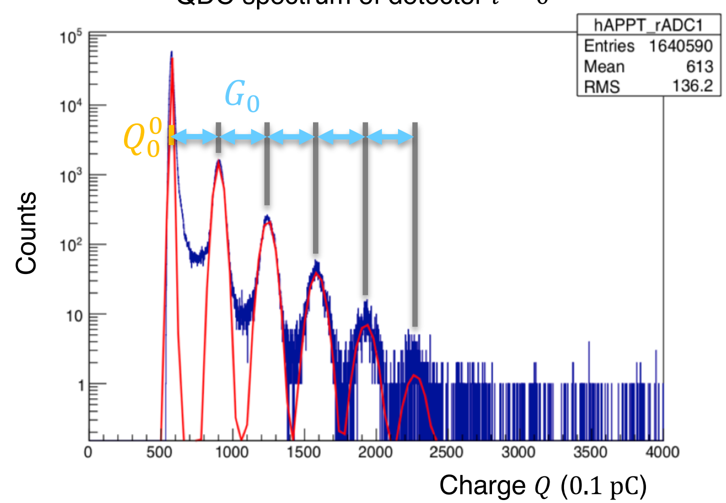

Additional SiPM literature: M. Biroth, et al., NIM A 787 (2015) 68-71, P. Achenbach, et al., NIM A 824 (2016) 74-75, M. Biroth et al., IEEE Trans. Nucl. Sci. 64 (2017) 1619-1624, P. Achenbach, et al., NIM A 912 (2018) 110-111

Proton Detection Efficiency and Threshold Energy

(In-)coherent processes are delimitated by requiring a recoil proton

π^0-photoproduction events for which the recoil proton reached the veto detector:

$N \to N_{E>0}$ Target fired

$N \to N_{E=0}$ Target did not fire

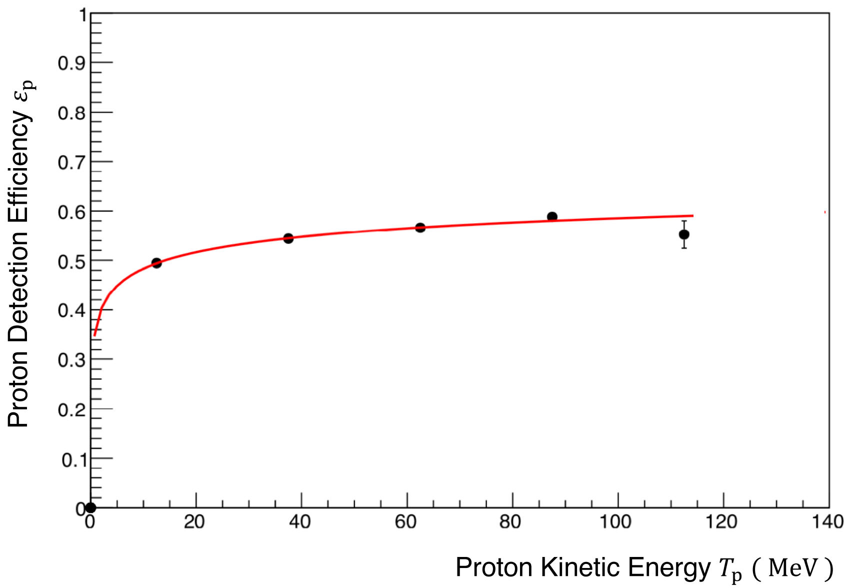

Definition of the proton detection efficiency ε_p:

$$\varepsilon_\mathrm{p} = \frac{N_{E>0}}{N_{E=0} + N_{E>0}} \cong \varepsilon_\infty \left(1 - \exp\left[-\ln 2 \frac{T_\mathrm{p}}{E_\mathrm{th}}\right]\right)$$

Detector	Maximum efficiency ε_∞	Threshold energy E_{th}
Veto	0.39 - 0.59*	70 MeV*
Active target	0.55(1)	3(1) MeV

Result confirmed by a missing mass analysis $\langle \varepsilon_\mathrm{p} \rangle_\mathrm{MM} \approx 0.54$

(∗) Detection efficiency of the Veto was investigated in the PhD thesis of P.P. Martel

ESR Spectrum of the Scintillator

- Field-modulated signal is the derivative of the spectrum
- Spectrum is comparable to TEMPO-doped butanol
- Discontinuities are caused by the base material and the radical

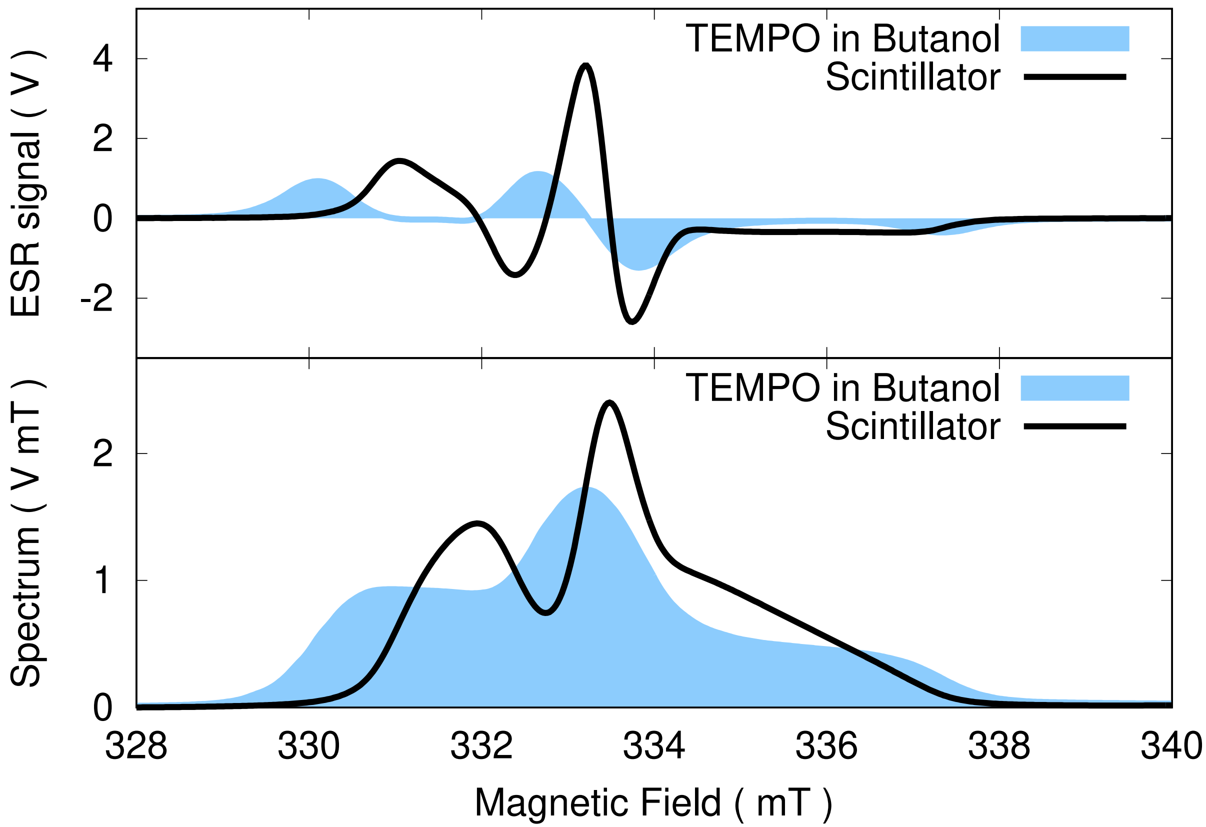

ESR = Electron Spin Resonance, µWave frequency $\omega_{\mathrm{ESR}} = 2\pi \times 9.36303\ \mathrm{GHz}$,
investigated radical density $\mathrm{n} = 3.0 \times 10^{19}\ \mathrm{cm}^{-3}$, TEMPO spectrum: S.T. Görtz, et al., NIM A526 (2004) 43-52

ESR Spectrum of the Scintillator

- Field-modulated signal is the derivative of the spectrum
- Spectrum is comparable to TEMPO-doped butanol
- Discontinuities are caused by the base material and the radical

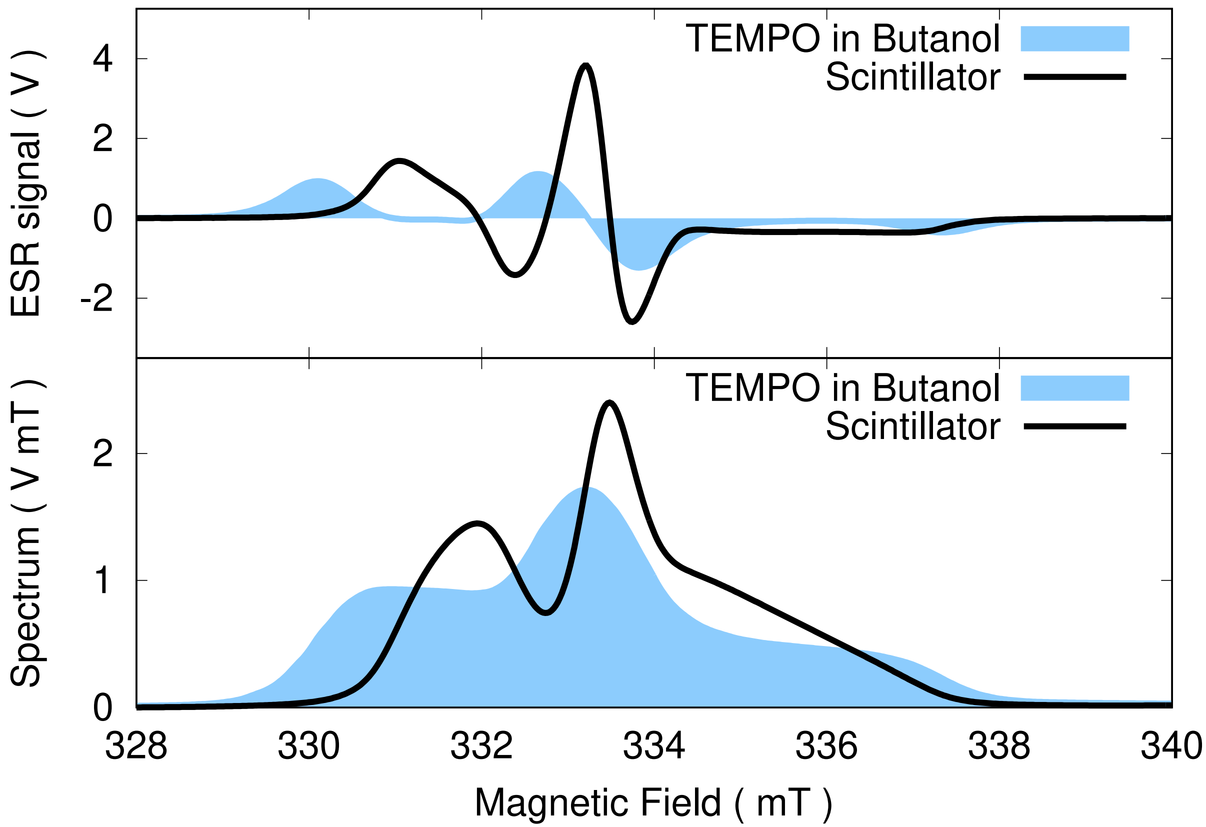

- Spin density was obtained as the magnitude of the spectrum relative to a DPPH sample

$$n = 3.55(46) \times 10^{19}\ \mathrm{cm}^{-3}$$

Reference: $3.0 \times 10^{19}\ \mathrm{cm}^{-3}$

ESR = Electron Spin Resonance, µWave frequency $\omega_{\mathrm{ESR}} = 2\pi \times 9.36303\ \mathrm{GHz}$,
investigated radical density $\mathrm{n} = 3.0 \times 10^{19}\ \mathrm{cm}^{-3}$, TEMPO spectrum: S.T. Görtz, et al., NIM A526 (2004) 43-52

ESR Spectrum of the Scintillator

- Field-modulated signal is the derivative of the spectrum
- Spectrum is comparable to TEMPO-doped butanol
- Discontinuities are caused by the base material and the radical

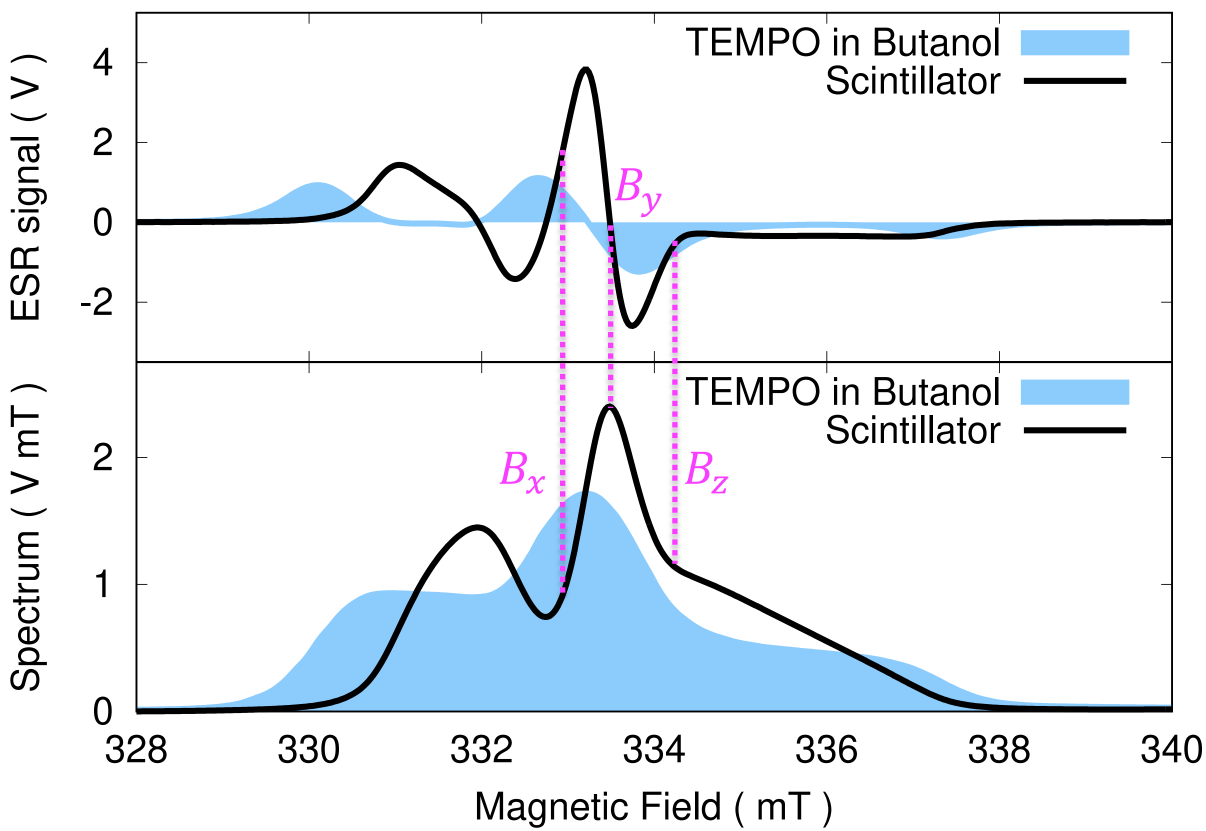

- Gyromagnetic ratio of glasses is an anisotropic tensor Γ

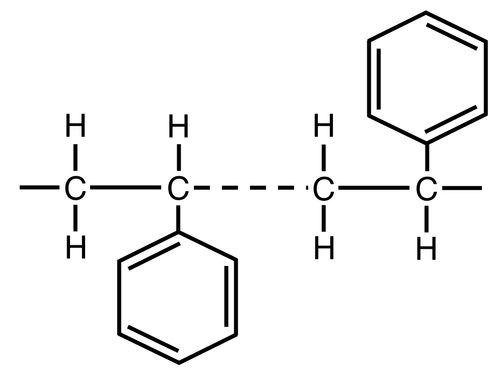

- Tensor is diagonal in the principal axes

$B_j = \omega_{\mathrm{ESR}} / \Gamma_{jj}$

ESR = Electron Spin Resonance, µWave frequency $\omega_{\mathrm{ESR}} = 2\pi \times 9.36303\ \mathrm{GHz}$, investigated radical density $\mathrm{n} = 3.0 \times 10^{19}\ \mathrm{cm}^{-3}$, TEMPO spectrum: S.T. Görtz, et al., NIM A526 (2004) 43-52

ESR Spectrum of the Scintillator

- Field-modulated signal is the derivative of the spectrum
- Spectrum is comparable to TEMPO-doped butanol
- Discontinuities are caused by the base material and the radical

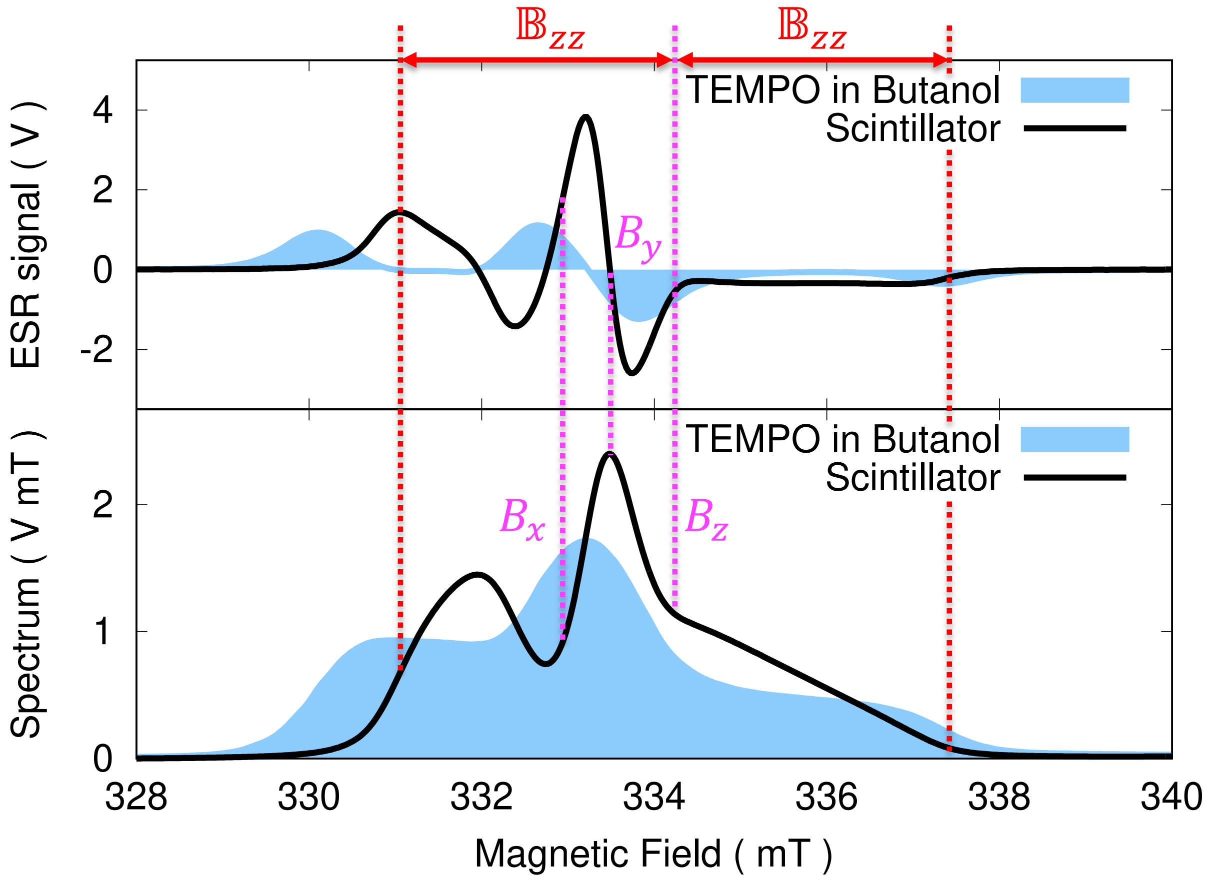

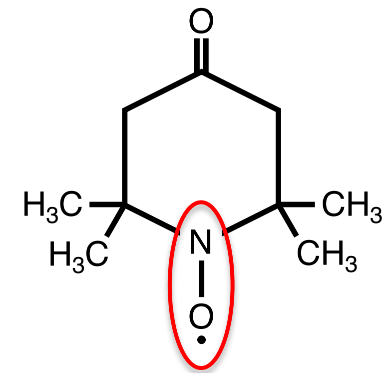

- Fringe field by hyperfine coupling to the spin-1 nitrogen
- Diagonal hyperfine tensor $\mathbb{B}_{jj}$ with strong zz-component

ESR = Electron Spin Resonance, μWave frequency $\omega_{\mathrm{ESR}} = 2\pi \times 9.36303\ \mathrm{GHz}$,
investigated radical density $\mathrm{n} = 3.0 \times 10^{19}\ \mathrm{cm}^{-3}$, TEMPO spectrum: S.T. Görtz, et al., NIM A526 (2004) 43-52

Transformation of the Spectrum to DNP Frequencies

- DNP field $B_0 = 2.5\,\mathrm{T}$ results in a resonance $\omega_\mathrm{e} \sim 2\pi \times 70\,\mathrm{GHz}$
- spectrum is not simply scaled, but also narrowed

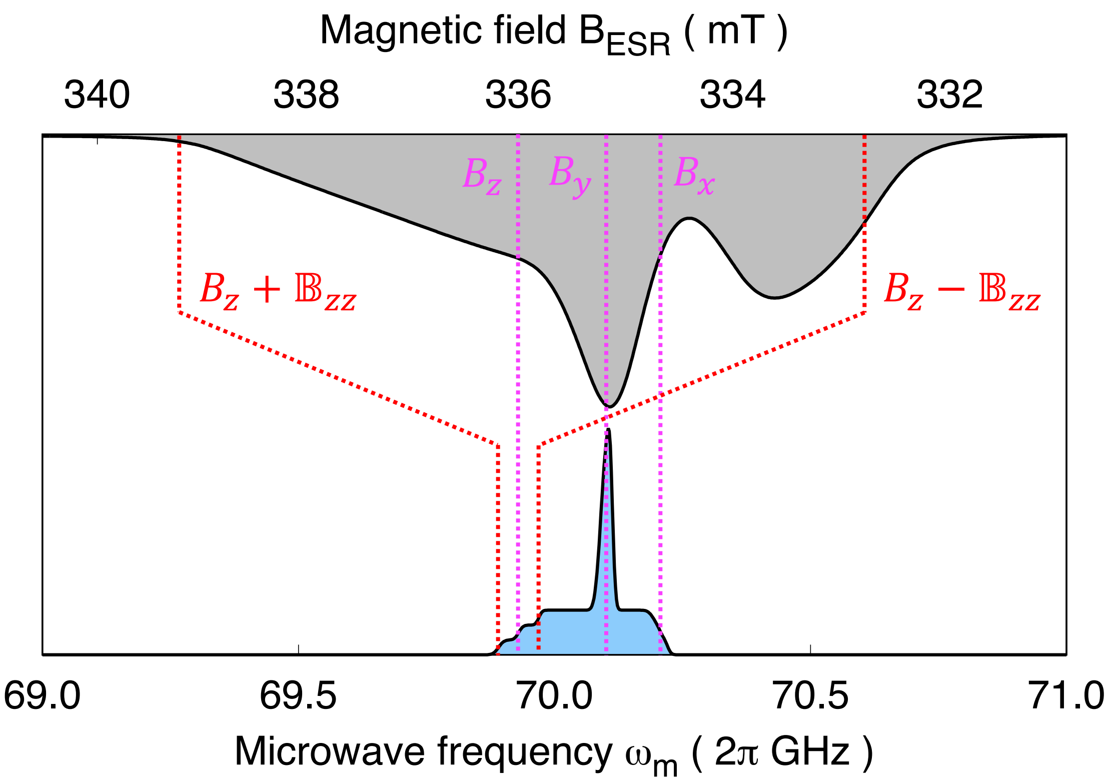

- Principal axes B_j transform proportional to the field B_0

$$\omega_j = \frac{\omega_\mathrm{ESR}}{B_j} B_0$$

- Fringe fields add up to B_0

$$\delta\omega_j \cong \frac{\omega_\mathrm{ESR}}{B_j} \delta B_j$$

  - hyperfine tensor $\mathbb{B}_{jj}$
  - super-hyperfine broadening

Expected Polarization Build-up

- Spin spectrum S_e determines the initial polarization growth $\partial P/\partial t$
- Overlapping contributions cancel by the differential solid effect

$$\frac{\partial P}{\partial t} \propto P_{\mathrm{TE,e}}\,\mathbb{P}_{\mathrm{m}}\,\left(S_e[\omega_{\mathrm{m}} + \gamma_{\mathrm{H}} B_0] - S_e[\omega_{\mathrm{m}} - \gamma_{\mathrm{H}} B_0]\right)$$

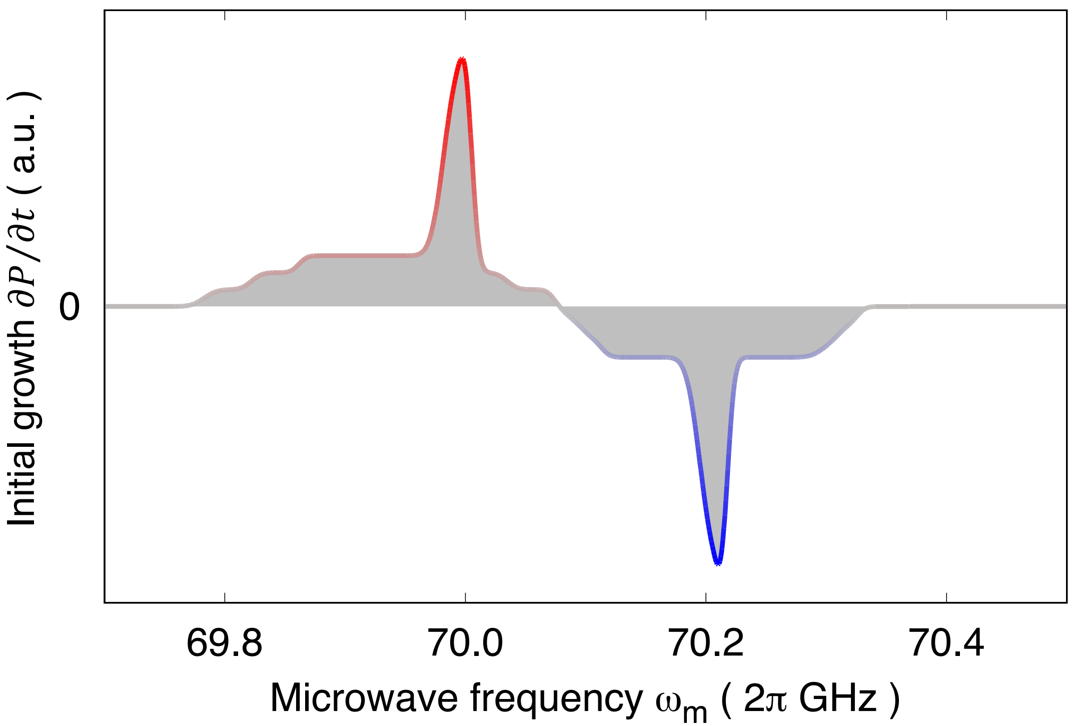

Expected Polarization Build-up

- Spin spectrum S_e determines the initial polarization growth $\partial P / \partial t$
- Overlapping contributions cancel by the differential solid effect

$$\frac{\partial P}{\partial t} \propto P_{\mathrm{TE,e}}\, \mathbb{P}_{\mathrm{m}}\, \left(S_e[\omega_{\mathrm{m}} + \gamma_{\mathrm{H}} B_0] - S_e[\omega_{\mathrm{m}} - \gamma_{\mathrm{H}} B_0]\right)$$

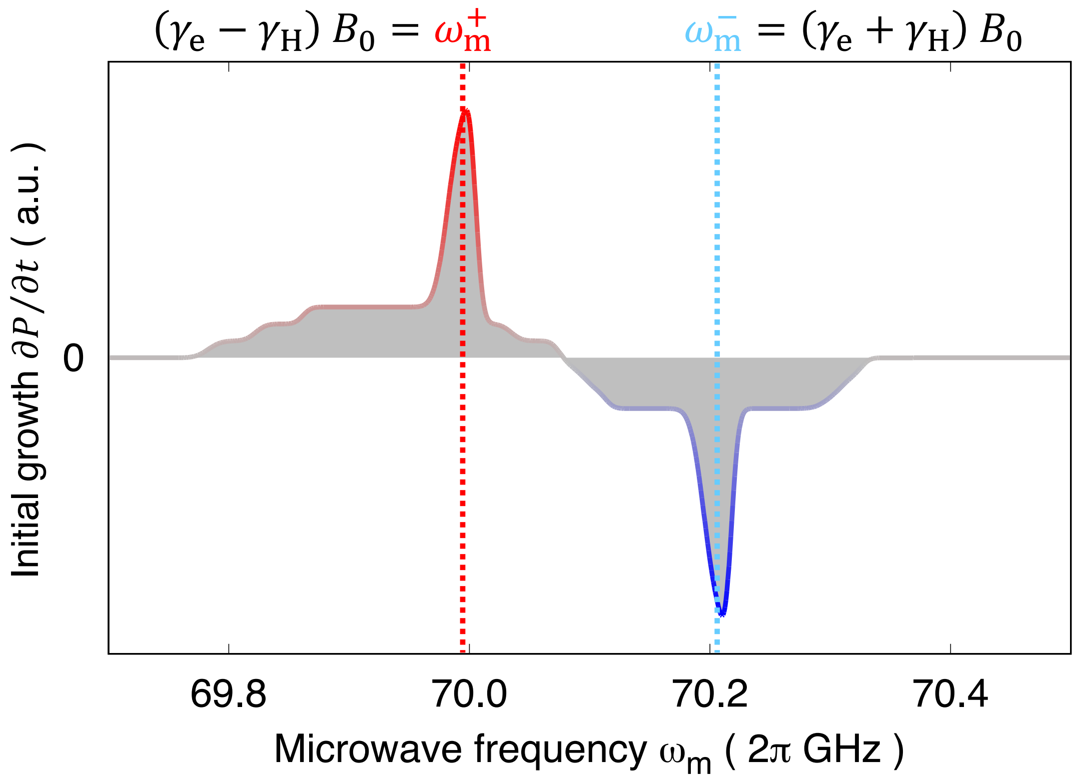

- Optimum polarization growth $\partial P / \partial t$ at $\omega_{\mathrm{m}}^{\pm}$

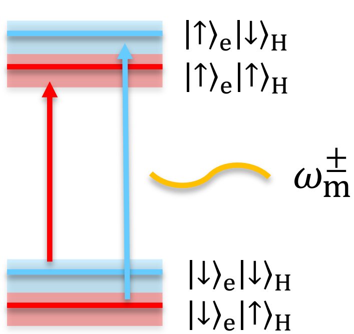

Expected Polarization Build-up

- Spin spectrum S_e determines the initial polarization growth $\partial P / \partial t$
- Overlapping contributions cancel by the differential solid effect

$$\frac{\partial P}{\partial t} \propto P_{\mathrm{TE,e}}\, \mathbb{P}_{\mathrm{m}} \left(S_e[\omega_{\mathrm{m}} + \gamma_{\mathrm{H}} B_0] - S_e[\omega_{\mathrm{m}} - \gamma_{\mathrm{H}} B_0] \right)$$

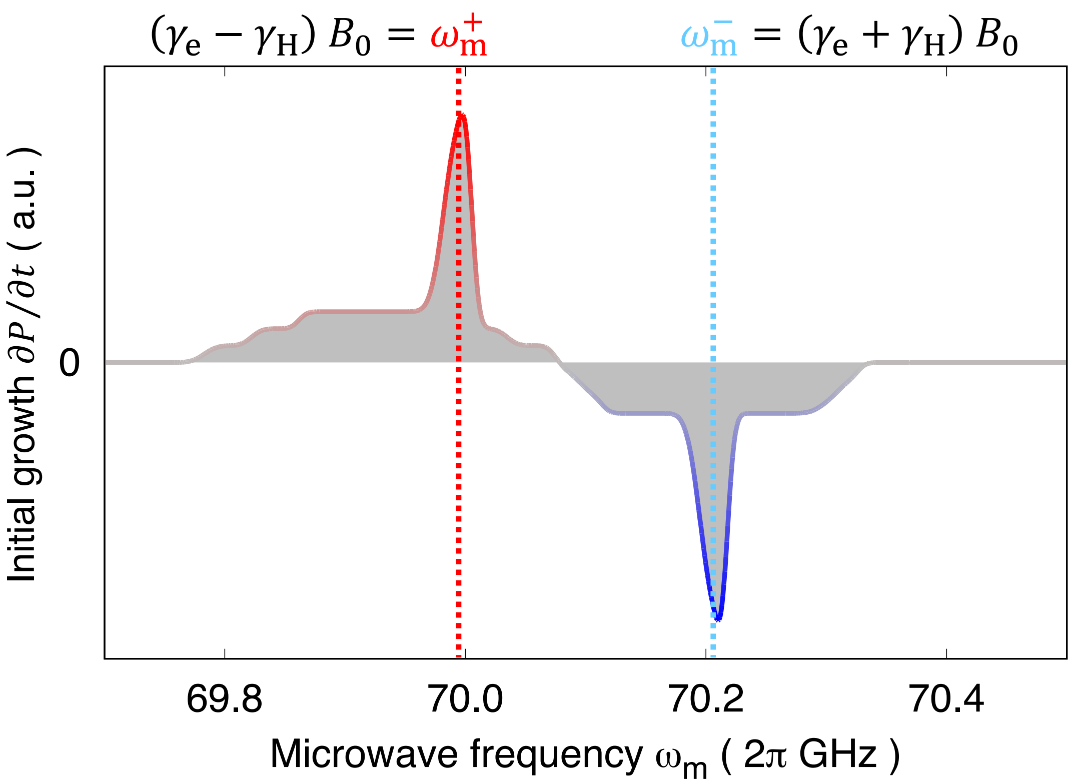

- Growth is proportional
  - to the lattice thermal equilibrium polarization $P_{\mathrm{TE,e}}$

Expected Polarization Build-up

- Spin spectrum S_e determines the initial polarization growth $\partial P/\partial t$
- Overlapping contributions cancel by the differential solid effect

$$\frac{\partial P}{\partial t} \propto P_{\mathrm{TE,e}}\, \mathbb{P}_{\mathrm{m}}\, (S_e[\omega_{\mathrm{m}} + \gamma_{\mathrm{H}} B_0] - S_e[\omega_{\mathrm{m}} - \gamma_{\mathrm{H}} B_0])$$

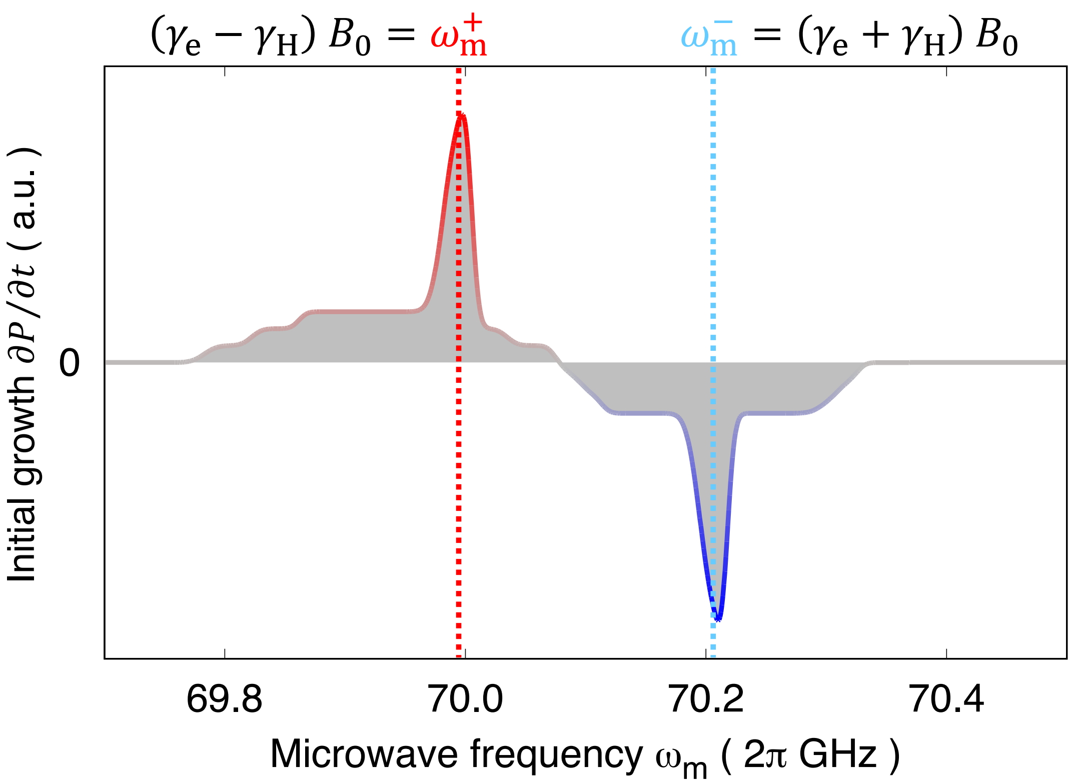

- Growth is proportional
  - to the lattice thermal equilibrium polarization $P_{\mathrm{TE,e}}$
  - initially to the µWave power $\mathbb{P}_{\mathrm{m}}$

mbiroth@uni-mainz.de

Saturation of the Polarization Build-up

- Polarization build-up saturates under high µWave power
- Adaptive reduction optimizes the growth during DNP

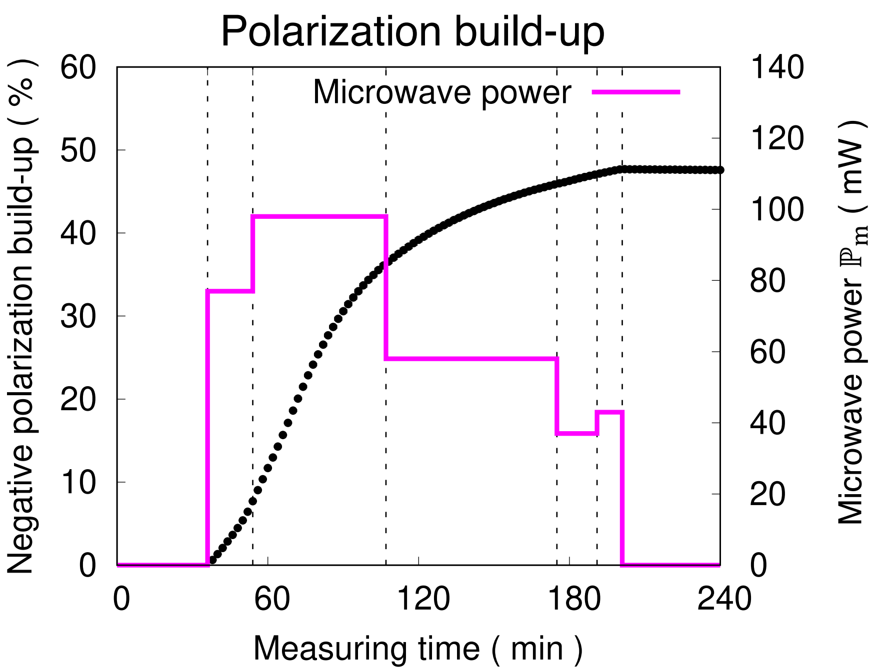

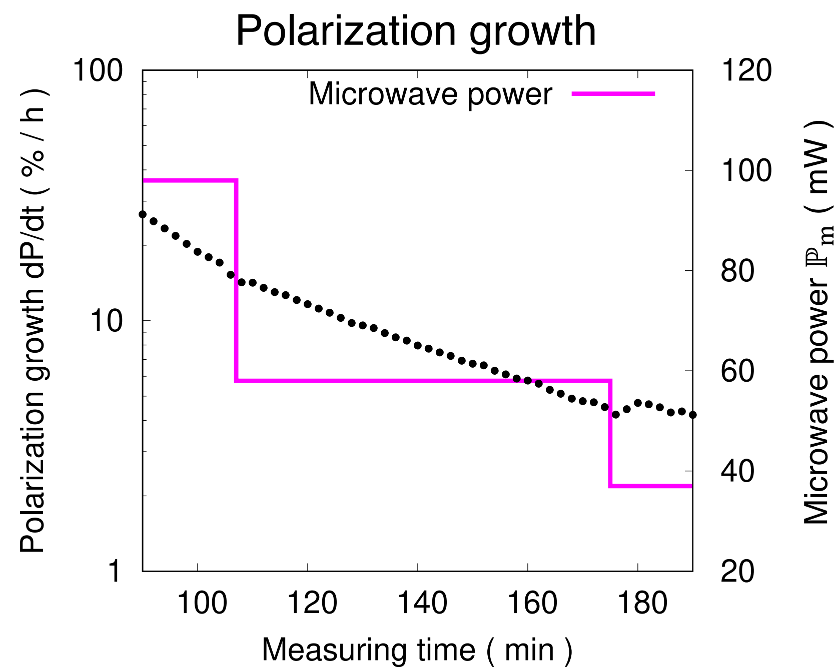

- Cooling power is limited by the molar flux $\dot{n}_{3\mathrm{He}}$ into the diluted phase
- Temperature changes typically by $1/\sqrt{-\dot{n}_{3\mathrm{He}}\,(\Delta S/T)} = 48\ \mathrm{mK}/\sqrt{\mathrm{mW}}$

Molar flux of ^{3}He $\dot{n}_{3\mathrm{He}} = 5.2\ \mathrm{mmol\ s^{-1}}$, entropy gradient ΔS for ^{3}He phase transition with $(\Delta S/T) = -84\ \mathrm{J\ K^{-2}}$

Requirements for Polarization Build-up and Measurement

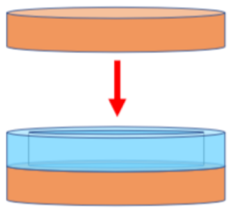

- Stack optimizes heat exchange by increasing the surface
  - 10 scintillator disks $\varnothing 20\ \mathrm{mm} \times 1\ \mathrm{mm}$
  - 9 PMMA rings $\varnothing 20\ \mathrm{mm} \times \varnothing 18\ \mathrm{mm} \times 0.5\ \mathrm{mm}$
- Optical coupling to the light concentrator by epoxy
- Slitting opens inter-disk volume
  - liquid helium circulation provides cooling during DNP

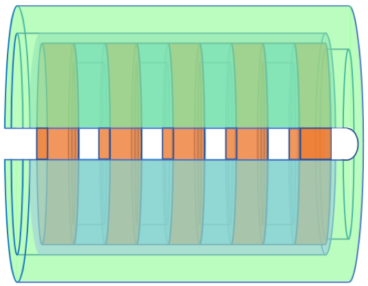

PMMA = Poly Methyl Methacrylate, CW-NMR = Continuous Wave Nuclear Magnetic Resonance

Requirements for Polarization Build-up and Measurement

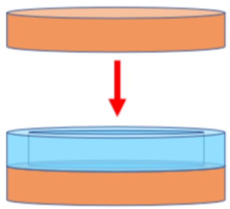

- Stack optimizes heat exchange by increasing the surface
  - 10 scintillator disks $\varnothing 20\ \mathrm{mm} \times 1\ \mathrm{mm}$
  - 9 PMMA rings $\varnothing 20\ \mathrm{mm} \times \varnothing 18\ \mathrm{mm} \times 0.5\ \mathrm{mm}$
- Optical coupling to the light concentrator by epoxy
- Slitting opens inter-disk volume
  - liquid helium circulation provides cooling during DNP
  - excitation and pick-up coil for NMR measurements

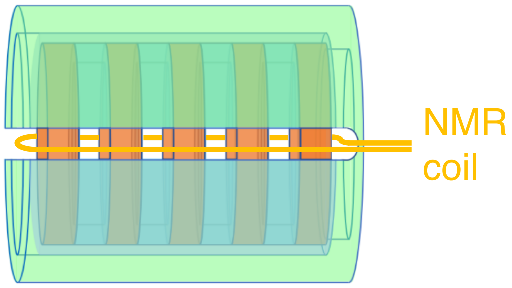

PMMA = Poly Methyl Methacrylate, CW-NMR = Continuous Wave Nuclear Magnetic Resonance

Requirements for Polarization Build-up and Measurement

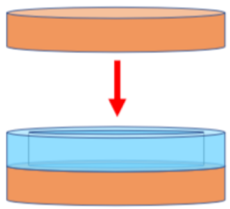

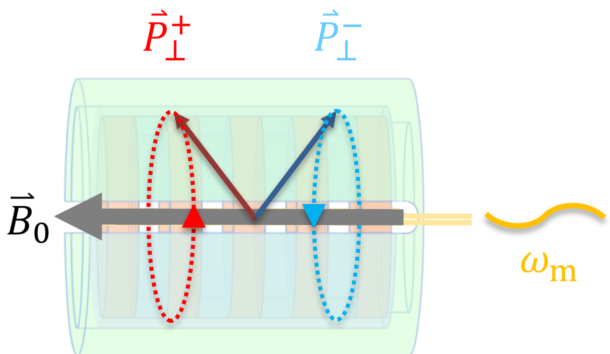

- Stack optimizes heat exchange by increasing the surface
  - 10 scintillator disks $\varnothing 20\ \text{mm} \times 1\ \text{mm}$
  - 9 PMMA rings $\varnothing 20\ \text{mm} \times \varnothing 18\ \text{mm} \times 0.5\ \text{mm}$
- Optical coupling to the light concentrator by epoxy
- Slitting opens inter-disk volume
  - liquid helium circulation provides cooling during DNP
  - excitation and pick-up coil for NMR measurements
- Continuous wave NMR measurement
  - excitation $\omega_\text{m} \sim \gamma_\text{H}\, B_0$ around the Larmor frequency

PMMA = Poly Methyl Methacrylate, CW-NMR = Continuous Wave Nuclear Magnetic Resonance

Requirements for Polarization Build-up and Measurement

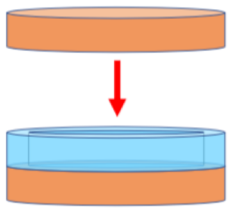

- Stack optimizes heat exchange by increasing the surface
  - 10 scintillator disks $\varnothing 20\ \mathrm{mm} \times 1\ \mathrm{mm}$
  - 9 PMMA rings $\varnothing 20\ \mathrm{mm} \times \varnothing 18\ \mathrm{mm} \times 0.5\ \mathrm{mm}$
- Optical coupling to the light concentrator by epoxy
- Slitting opens inter-disk volume
  - liquid helium circulation provides cooling during DNP
  - excitation and pick-up coil for NMR measurements

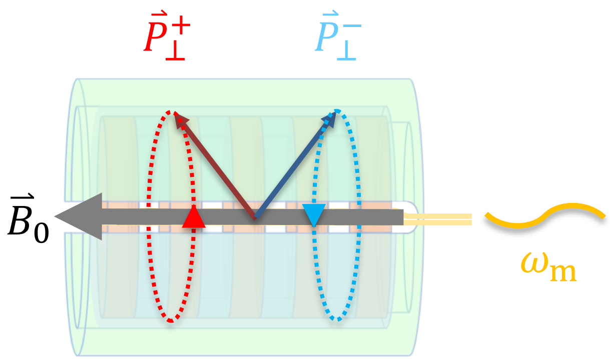

- Continuous wave NMR measurement
  - excitation $\omega_\mathrm{m} \sim \gamma_\mathrm{H}\, B_0$ around the Larmor frequency
  - pick-up of the Gaussian energy dissipation ΔE

$$A := \int d\omega_\mathrm{m}\, \Delta E \propto -P$$

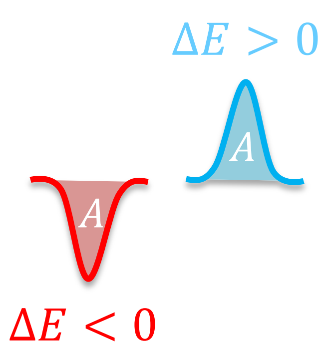

PMMA = Poly Methyl Methacrylate, CW-NMR = Continuous Wave Nuclear Magnetic Resonance

Calibration of the Polarization Measurement

An absolute measurement requires a thermal equilibrium calibration:

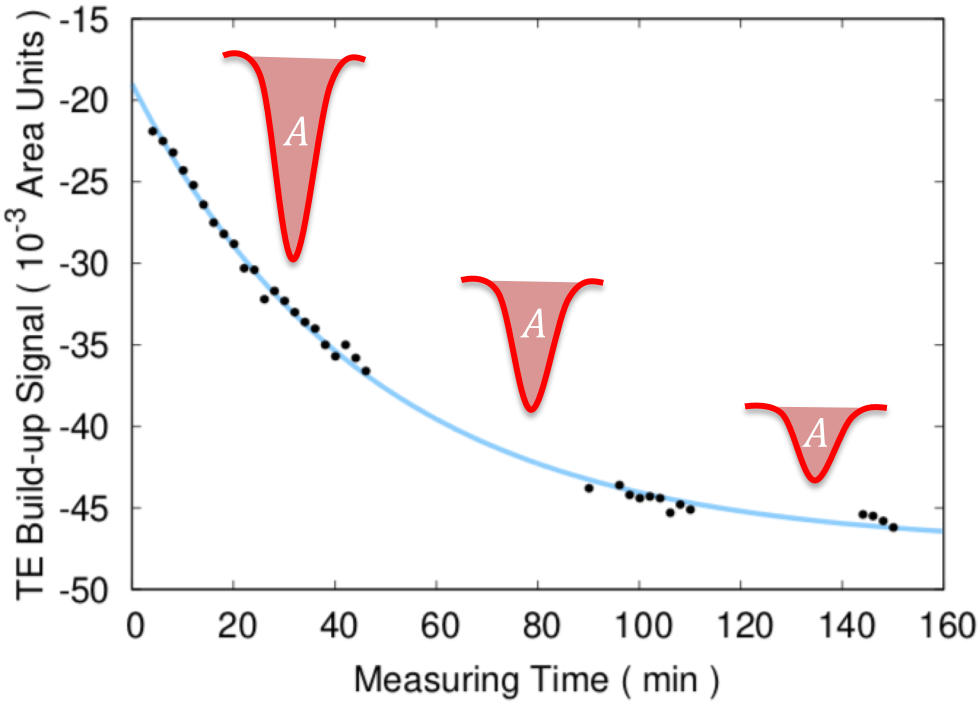

1. Temperature settles at $T_{\mathrm{TE}} \sim 1\ K$ after removal of ^{3}He

2. Polarization decays exponentially with $\tau_{1,\mathrm{TE}} \sim 46$ min to:

$$P_{\mathrm{TE}} = \tanh \frac{\hbar \gamma_{\mathrm{H}} B_0}{2 k_{\mathrm{B}} T_{\mathrm{TE}}} = 0.25\ \%$$

3. Integral relaxes to its thermal equilibrium value A_{TE}

$$\frac{P}{P_{\mathrm{TE}}} \cong \frac{A}{A_{\mathrm{TE}}} = 1 - \exp\left[-\frac{t}{\tau_{1,\mathrm{TE}}}\right]$$

Effect of the Supporting Structure on the Calibration

- Non-doped materials are also enclosed by the NMR coil
- Non-polarizable hydrogen constitutes 44% of the NMR signal
- Resonance frequency shift of $-160\ \mathrm{ppm}$ enables separation

Double-peak structure in the NMR signal

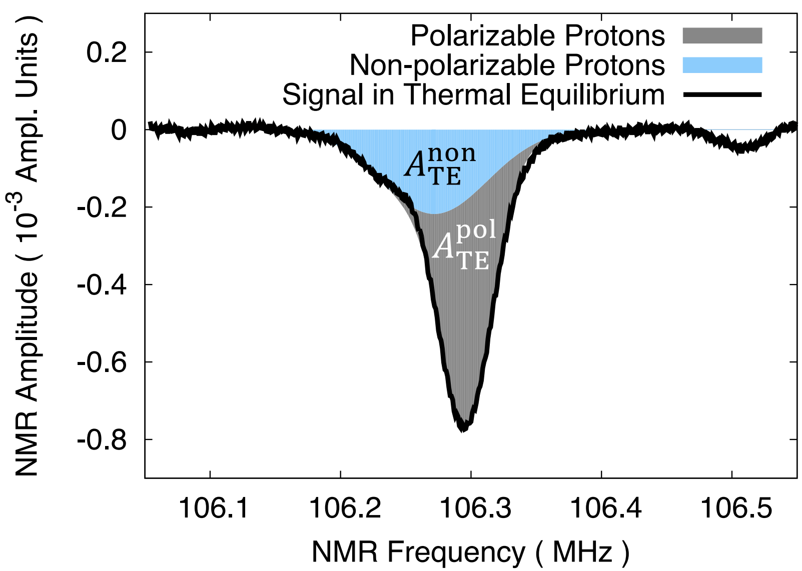

Blue peak does not polarize under DNP

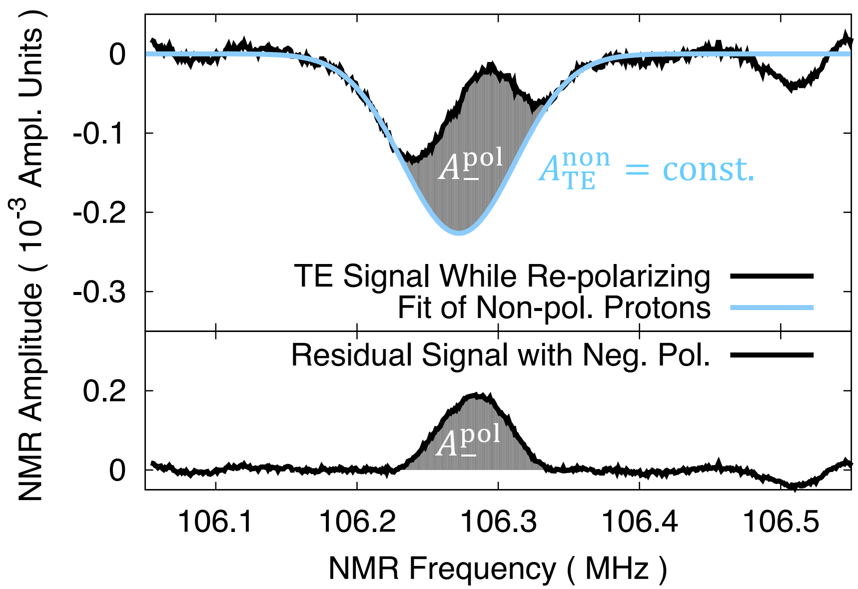

Double-Gaussian curve-fit yields:

$$A_{\mathrm{TE}} = -50\ \mathrm{AU} \quad \rightarrow \quad A_{\mathrm{TE}}^{\mathrm{pol}} = -28\ \mathrm{AU}, \quad A_{\mathrm{TE}}^{\mathrm{non}} = -22\ \mathrm{AU}$$

The actual polarization is calculated as:

$$P = \frac{P_{\mathrm{TE}}}{A_{\mathrm{TE}}^{\mathrm{pol}}}\left(A - A_{\mathrm{TE}}^{\mathrm{non}}\right)$$

Achieved Degree of Polarization and Relaxation Time

Maximum polarization and spin-lattice relaxation time are low compared to TEMPO-doped Butanol:

Property	Active Target		Butanol target
	Positive	Negative	
Temperature	$> 45\ \mathrm{mK}$		$28\ \mathrm{mK}$
Max. Polarization	$46.2\ \%$	$-49.2\ \%$	$\|P\| > 80\ \%$
Relaxation time	$78.5\ \mathrm{h}$	$75.4\ \mathrm{h}$	$> 1200\ h$

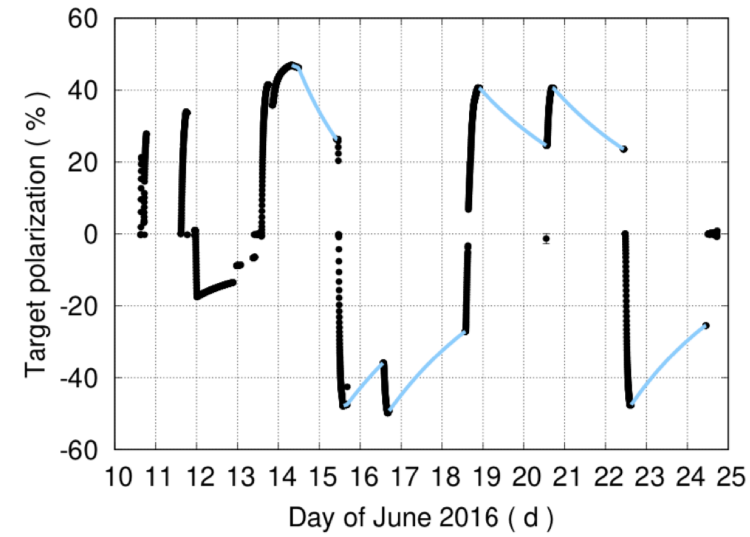

Approaches to optimize the polarization:

1. Reducing the spin density ($n < 1.5 \times 10^{19}\ \mathrm{cm}^{-3}$)

1. Reducing the temperature to $T < 30\ \mathrm{mK}$ predicts relaxation times of $\tau_1 > 1000\ \mathrm{h}$

2. Doubling the high field $B_0 = 5\ \mathrm{T}$ corresponds to halving the temperature during DNP

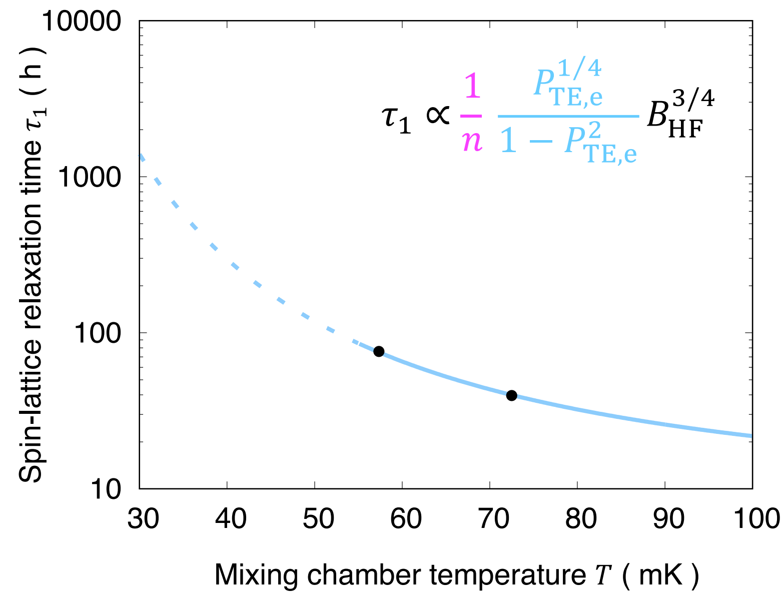

Maik Biroth, Institute of Nuclear Physics, Mainz, Germany
mbiroth@uni-mainz.de

Next Generation Active Target and Polarizable Scintillator

Semi-active Target Concept: A cage of segmented standard plastic scintillators surrounds a Teflon container with doped Butanol inside.

- Fiber readout minimizes the intensity attenuation
- Enables carbon subtraction using an carbon foam
- Doped pellets can be H- or D-Butanol

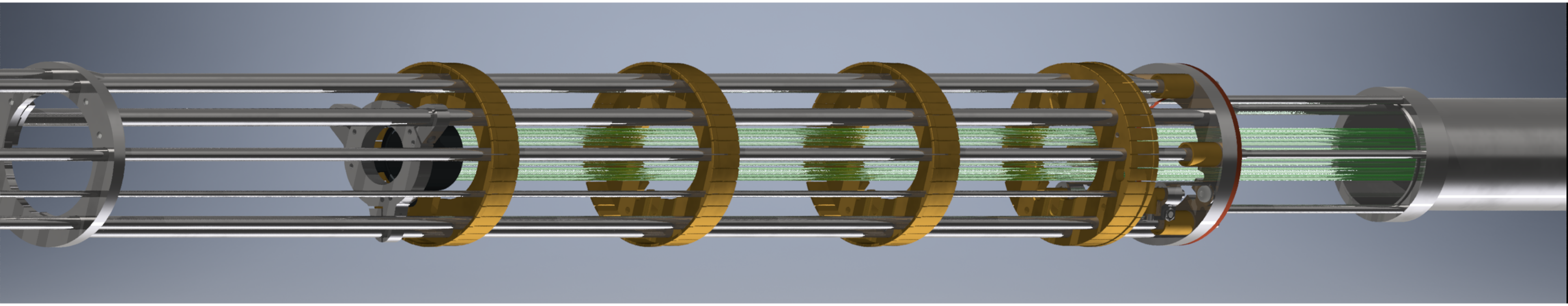

Next Generation Active Target and Polarizable Scintillator

Semi-active Target Concept: A cage of segmented standard plastic scintillators surrounds a Teflon container with doped Butanol inside.

- Fiber readout minimizes the intensity attenuation
- Enables carbon subtraction using an carbon foam
- Doped pellets can be H- or D-Butanol

- Segmentation provides ϕ-resolution. Efficiency gaps are avoided by dovetailing of the scintillator bars.

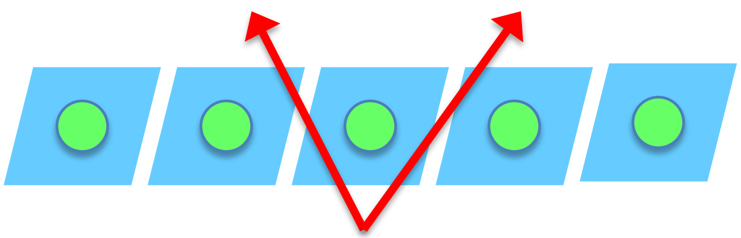

- Alternating coupling of the bars could provide θ-resolution by next-neighbor crosstalk.

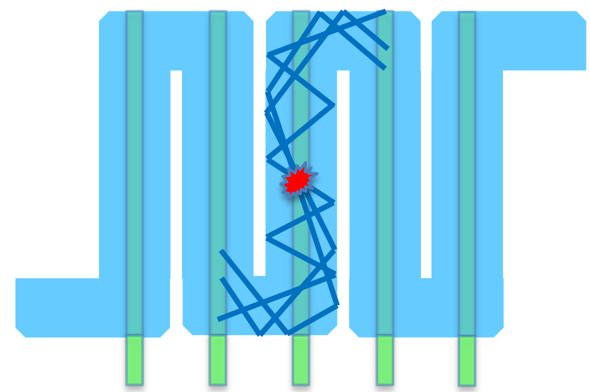

The next-generation polarizable scintillator could be developed

- by doping in cooperation with the Mainz PRISMA+ Laboratory for Scintillation and Fluorescence Detectors
- by irradiation at ELSA in cooperation with the Bonn Polarized Target Group

Transformation of the Approved Sealing Concept

First Active Target Concept

Flange (SS) Outer seal (PMMA) Inner seal (PMMA) Active Head

Semi-active Target Concept

Flange and tube (SS)

Scintillating head with fiber readout

Butanol container (PTFE)

Transformation of the Approved Sealing Concept

First Active Target Concept

Flange (SS) Outer seal (PMMA)

Upcoming work of
Andre Klotzbücher

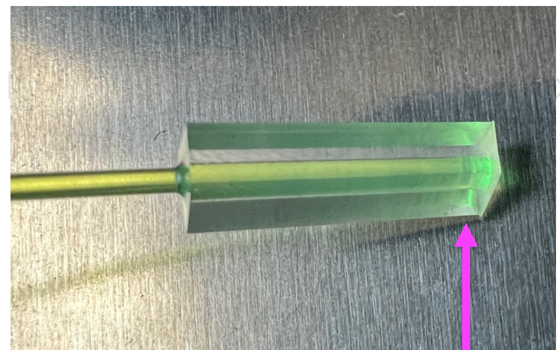

Semi-active Target Concept

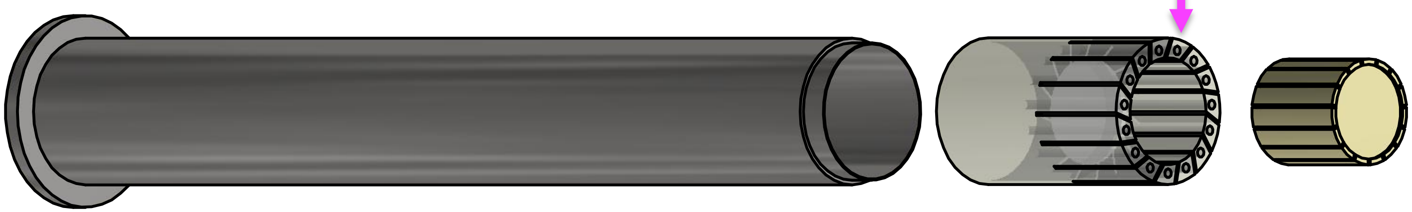

Flange and tube (SS)

Scintillating head
with fiber readout

Butanol
container (PTFE)

Summary of Achieved Properties

Advanced design of the Active Polarized Proton Target enables

- Temperatures down to $\mathrm{T} \sim 45\ \mathrm{mK}$
- Helium tightness under thermal cycling
- Single-photon energy resolution

Degree of polarization ⟷ Detection capability

- Target spin polarization $|P| \sim 50\ \%$
- Spin-lattice relaxation time $\tau_1 \sim 75\ \mathrm{h}$

- Proton detection efficiency $\varepsilon_\infty \sim 55\ \%$
- Threshold energy $E_{\mathrm{th}} \sim 3\ \mathrm{MeV}$

Summary of Achieved Properties

Advanced design of the Active Polarized Proton Target enables

- Temperatures down to $\mathrm{T} \sim 45\ \mathrm{mK}$
- Helium tightness under thermal cycling
- Single-photon energy resolution

Degree of polarization ⟷ Detection capability

- Target spin polarization $|P| \sim 50\ \%$
- Spin-lattice relaxation time $\tau_1 \sim 75\ \mathrm{h}$

- Proton detection efficiency $\varepsilon_\infty \sim 55\ \%$
- Threshold energy $E_{\mathrm{th}} \sim 3\ \mathrm{MeV}$

Thank you for your attention!

Appendix

No unpaired electron spins were found in the supporting materials.
The supporting structure is not polarizable by DNP.

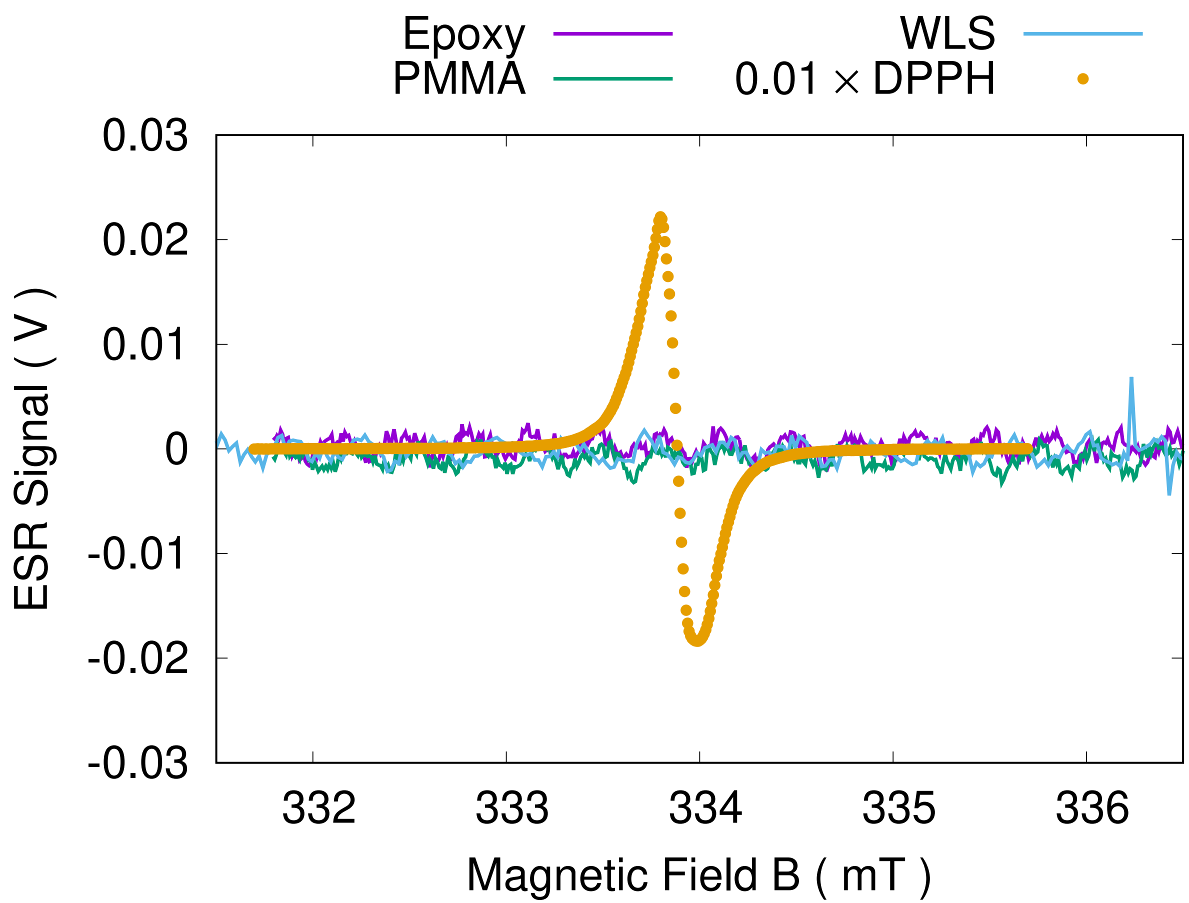

Polarized electrons $E_{\mathrm{e}0} = 450\ \mathrm{MeV}$ on an amorphous FeCo radiator

- Incoherent Bremsstrahlung with Bethe-Heidler cross-section

$$\frac{\mathrm{d}\sigma}{\mathrm{d}E_{\gamma 0}} = \frac{A}{\chi_0 N_A} \frac{1}{E_{\gamma 0}} \left(\frac{4}{3}(1-x) + x^2 \right) \qquad \text{with } x = \frac{E_{\gamma 0}}{E_{\mathrm{e}0}}$$

- Transfer of longitudinal electron polarization $P_\mathrm{e} \gtrsim 75\ \%$ to the circular photon polarization P_γ

$$\frac{P_\gamma}{P_\mathrm{e}} = \frac{2\left(\frac{2}{x} - 1\right) + 1}{\left(\frac{2}{x} - 1\right)^2 + 2}$$

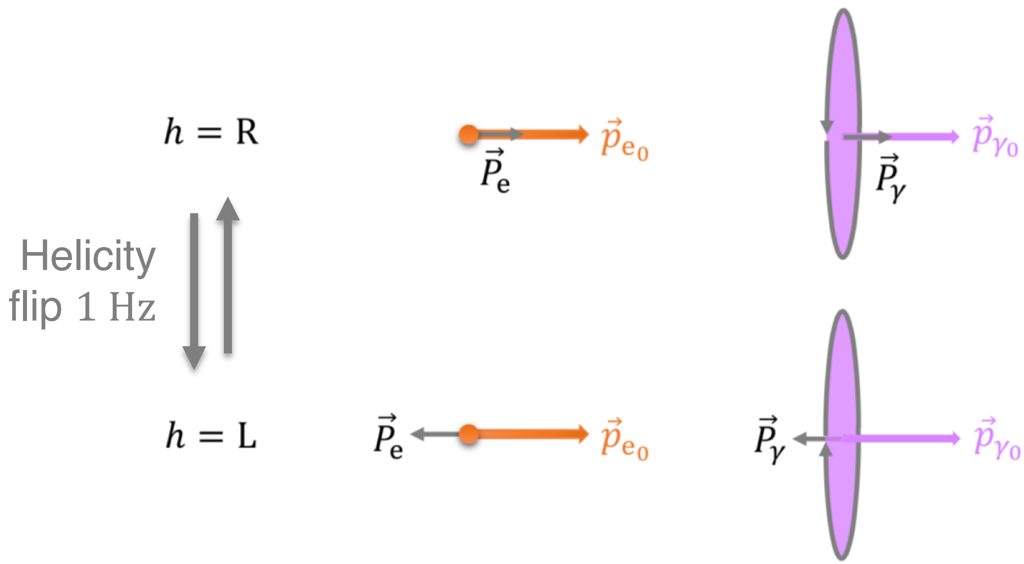

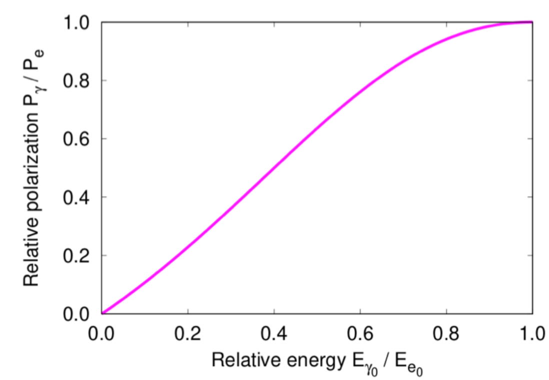

(Double-)Polarized Compton Asymmetries

The spin orientations modulate a dependence on the azimuthal photon angle ϕ_γ on the cross-sections σ_{2x} and σ_3.

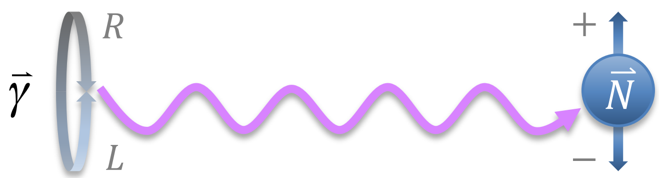

$$\Sigma_{2x} = \frac{\sigma_\uparrow - \sigma_\downarrow}{\sigma_\uparrow + \sigma_\downarrow} \qquad \frac{\mathrm{d}\sigma_{2x}}{\mathrm{d}\Omega} = \frac{\mathrm{d}\sigma_0}{\mathrm{d}\Omega}\left(1 + P_\mathrm{N}\, P_\gamma \sin\phi_\gamma\, \Sigma_{2x}\right)$$

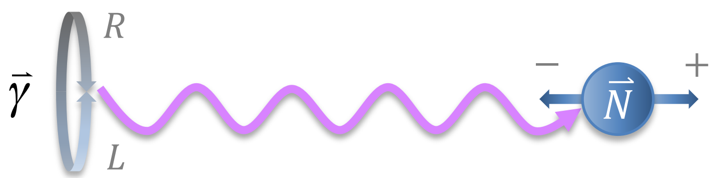

$$\Sigma_{2z} = \frac{\sigma_\rightarrow - \sigma_\leftarrow}{\sigma_\rightarrow + \sigma_\leftarrow} \qquad \frac{\mathrm{d}\sigma_{2z}}{\mathrm{d}\Omega} = \frac{\mathrm{d}\sigma_0}{\mathrm{d}\Omega}\left(1 + P_\mathrm{N}\, P_\gamma\, \Sigma_{2z}\right)$$

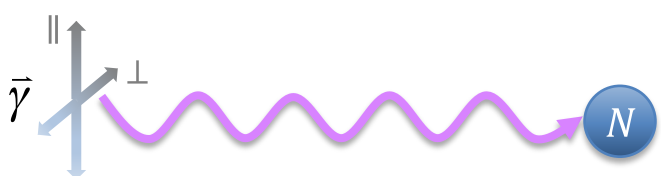

$$\Sigma_3 = \frac{\sigma_\parallel - \sigma_\perp}{\sigma_\parallel + \sigma_\perp} \qquad \frac{\mathrm{d}\sigma_3}{\mathrm{d}\Omega} = \frac{\mathrm{d}\sigma_0}{\mathrm{d}\Omega}\left(1 + P_\gamma \cos 2\phi_\gamma\, \Sigma_3\right)$$

Degree of nucleon polarization P_N and photon polarization P_γ

Maik Biroth, Institute of Nuclear Physics, Mainz, Germany mbiroth@uni-mainz.de

Sensitivity to the Spin-polarizabilities

Σ_{2x} best sensitivity to γ_{E1E1}

$$\gamma_{\mathrm{E1M2}} = -\gamma_{\mathrm{E1E1}} - \frac{1}{2}\gamma_0 - \frac{1}{2}\gamma_\pi$$

Data: P.P. Martel, et al., Phys. Rev. Lett. 114 (2015) 112501

Σ_{2z} best sensitivity to γ_{M1M1}

$$\gamma_{\mathrm{M1E2}} = -\gamma_{\mathrm{M1M1}} - \frac{1}{2}\gamma_0 + \frac{1}{2}\gamma_\pi$$

Data: D. Paudyal, et al., Phys. Rev. C 102 (2020) 035205

Σ_3 best sensitivity to γ_{M1M1}

New data: E. Mornacchi, et al., under internal Rev. (2021)

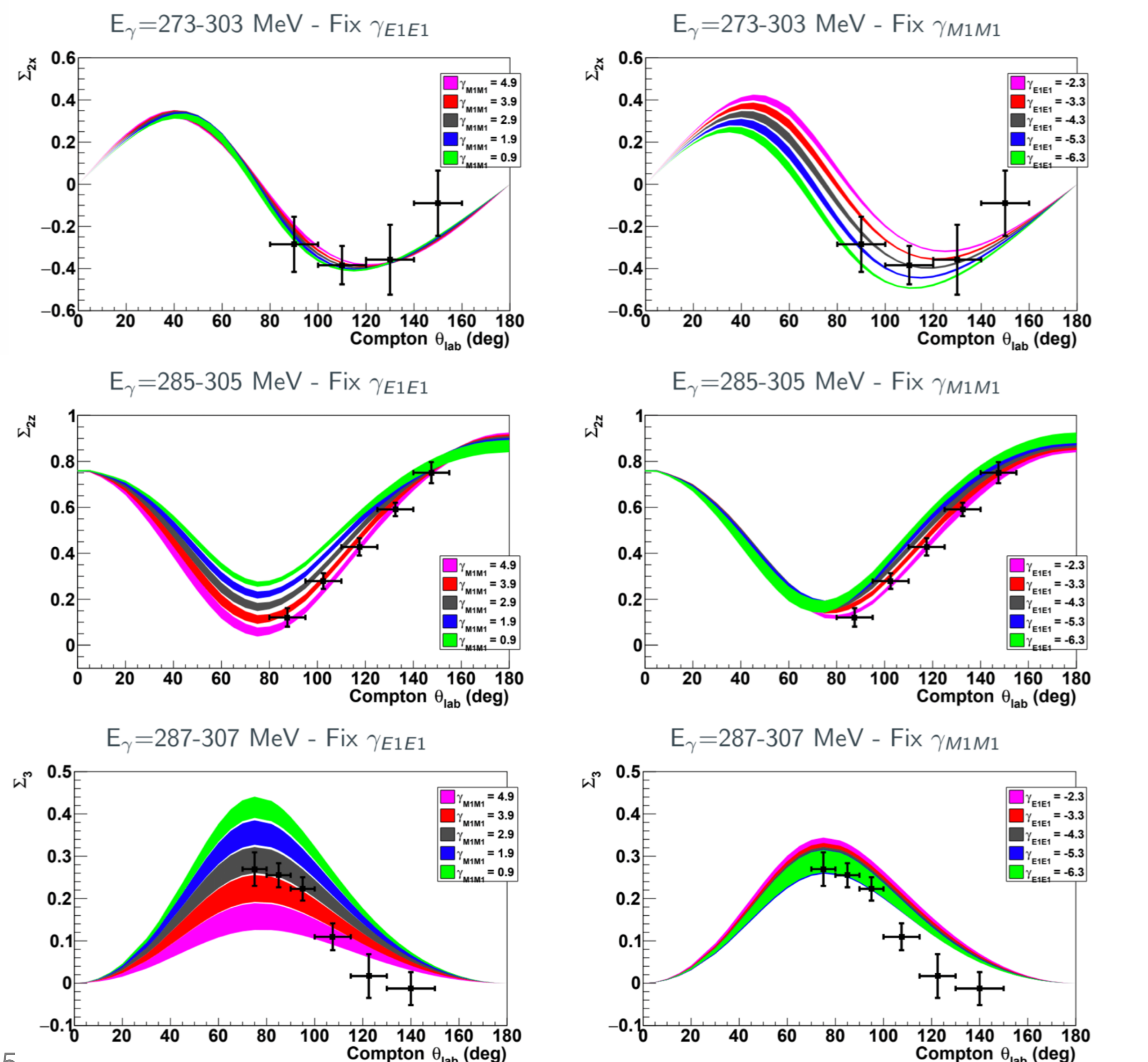

Simulation by P.P. Martel, PhD Thesis 2015

Neutral Pion Count Rate Asymmetry

The π^0-photoproduction count rate asymmetry scales with $\mathcal{F}$. Additionally, an intrinsic transverse target asymmetry $\mathcal{T}$ contributes.

$$\frac{N_{\pm}^{\mathrm{R}} - N_{\pm}^{\mathrm{L}}}{N_{\pm}^{\mathrm{R}} + N_{\pm}^{\mathrm{L}}} = \pm \frac{P_{\mathrm{p}} P_{\gamma}\, \mathcal{F} \sin\phi_{\gamma}}{1 \pm P_{\mathrm{p}}\, \mathcal{T} \cos\phi_{\gamma}}$$

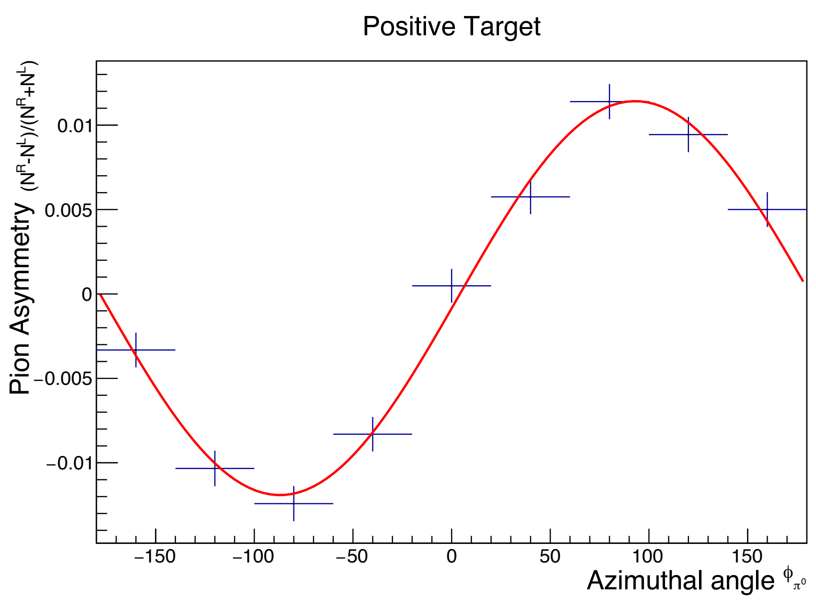

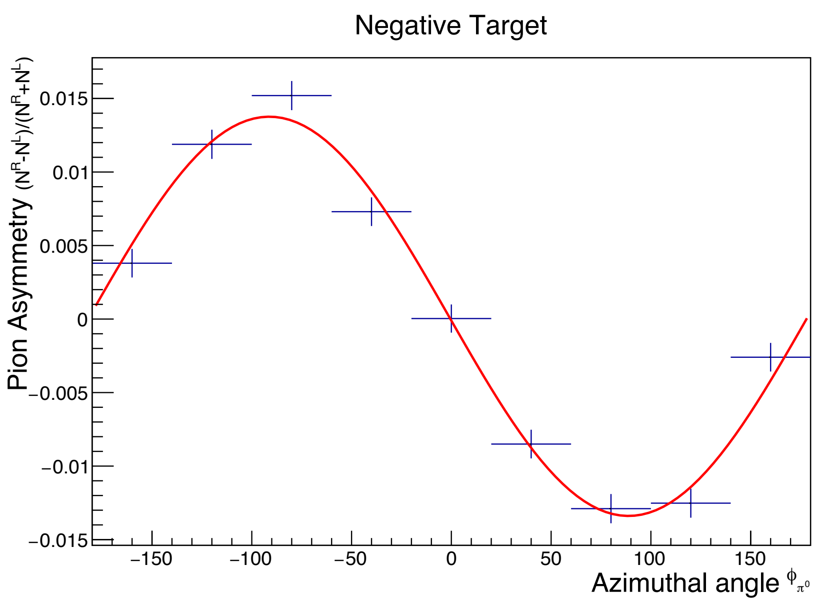

Analysis of the 2016, June data by P.P. Martel

Time Calculation and Coincidence with the Tagger

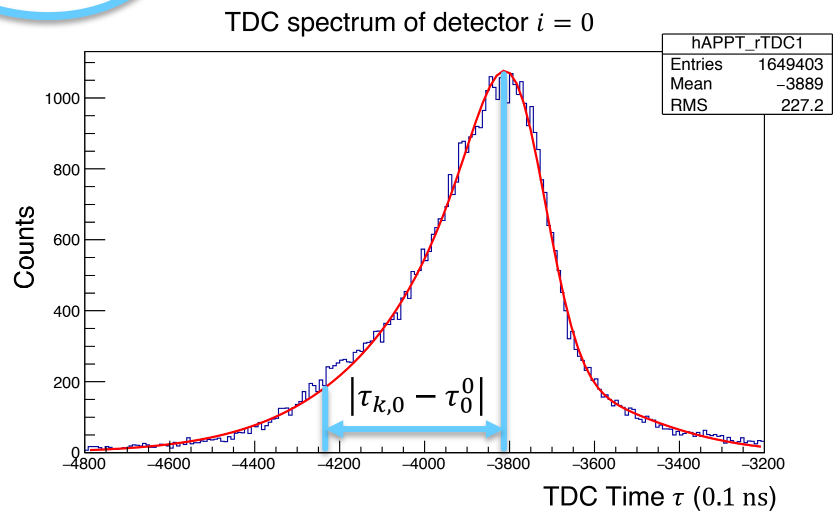

- For each run: detector specific time reference τ_i^0 by curve-fitting
- For each event: target time t_k as the minimum time-to-reference

$$t_k = \tau_{k,m} - \tau_m^0 \,:\, \left|\tau_{k,m} - \tau_m^0\right| \leq \left|\tau_{k,i} - \tau_i^0\right| \,\forall\, i \in [0{,}14]$$

- Coincidence with tagged photons is overlapped by a uniform distribution

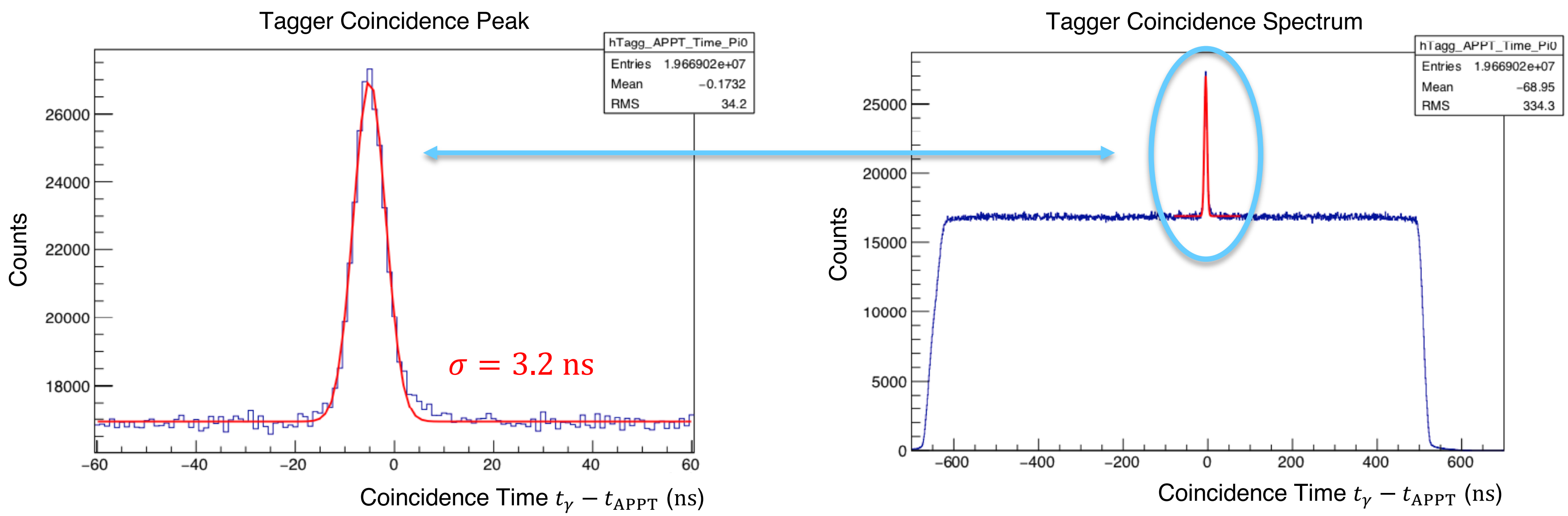

Delimitation of Background Contributions

Accidental photons are the main background contribution

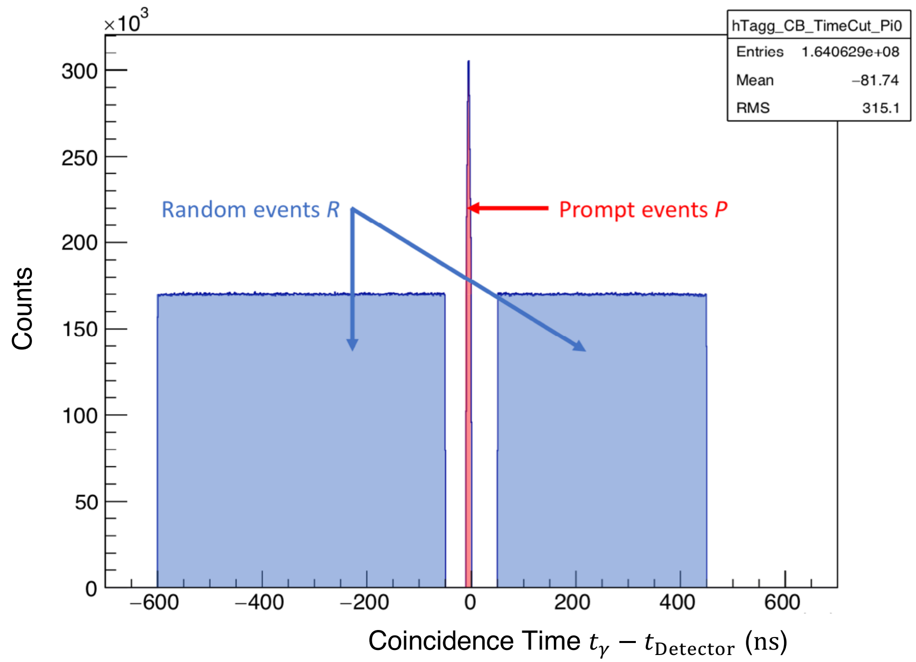

Prompt-Random subtraction

- Prompt events P in a $\pm\,\Delta t_P/2$ environment around the coincidence peak
- Random events R far off from the coincidence peak with the total width Δt_R
- True estimate N of coincident events

$$N = P - \left(\frac{\Delta t_P}{\Delta t_R}\right) R$$

Threading two large contributions requires angular resolution

- Nuclear background by scattering off ^{4}He, ^{12}C, or heavier nuclei inside the target
- Photon misidentification of one neutral pion decay photon if the other is not detected

Angular resolution was not achievable due to the 1.5 m long light guide tube

Proton Detection Efficiency from Missing Mass

(In-)coherent π^0 events (I) do not include any charged recoil particles. Recoil protons with $E = 0$ are not detected (II).

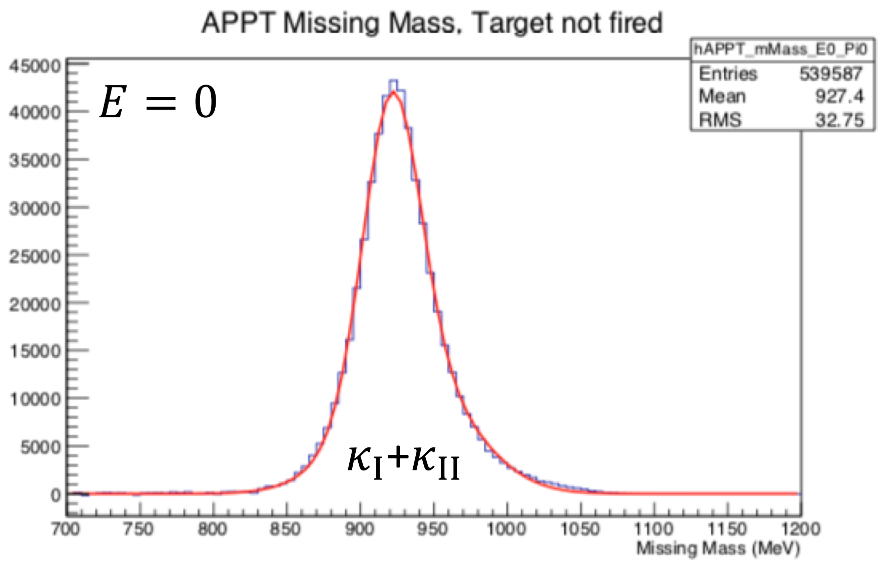

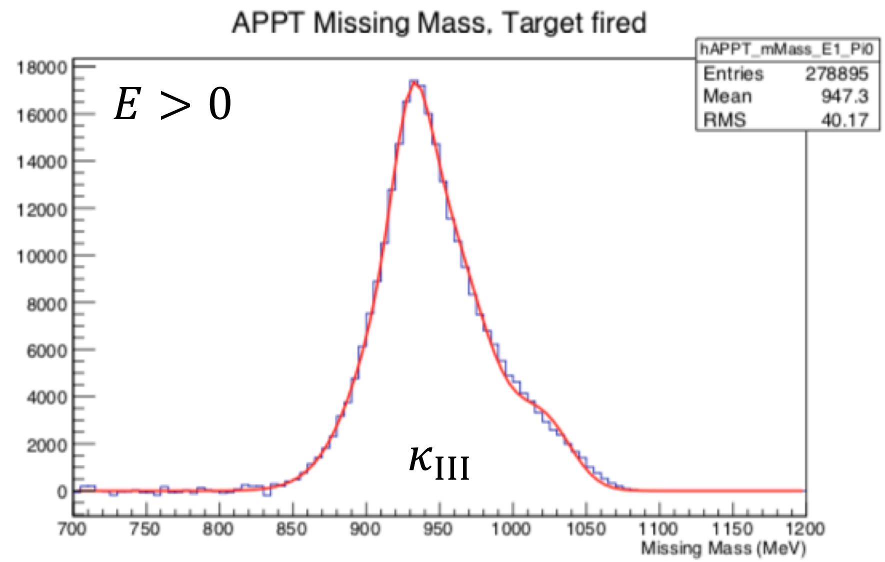

Energy	Case	Contributions	Peak mass	Branching
$E = 0$	I	(in-)coherent	921 MeV	$\kappa_{\mathrm{I}} = 0.363$
	II	not detected	935 MeV	$\kappa_{\mathrm{II}} = 0.295$
$E > 0$	III	detected	–	$\kappa_{\mathrm{III}} = 0.342$

Average Proton detection efficiency:

$$\langle \varepsilon_{\mathrm{p}} \rangle_{\mathrm{MM}} = \frac{\kappa_{\mathrm{III}}}{\kappa_{\mathrm{II}} + \kappa_{\mathrm{III}}} = 0.54$$

Separation of (In-)coherent Processes

(In-)coherent processes do not include any charged recoil particles.

All π^0 events

(In-)Coherent events off ^{12}C

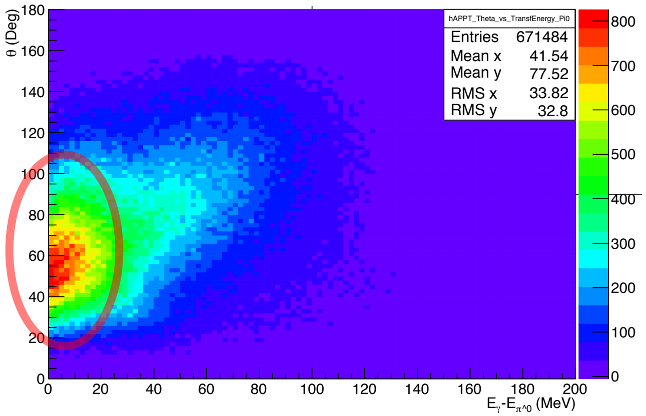

Recoil detected

Target fired

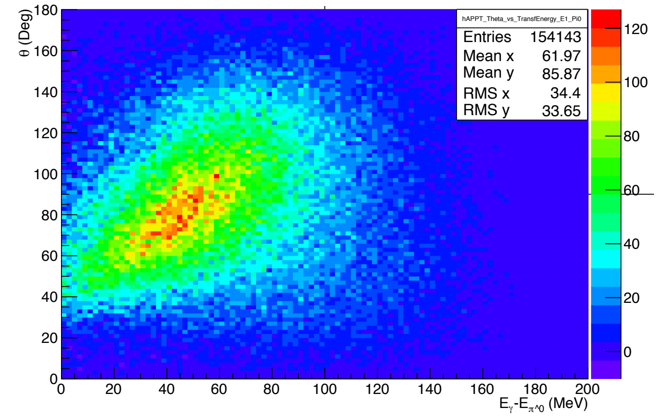

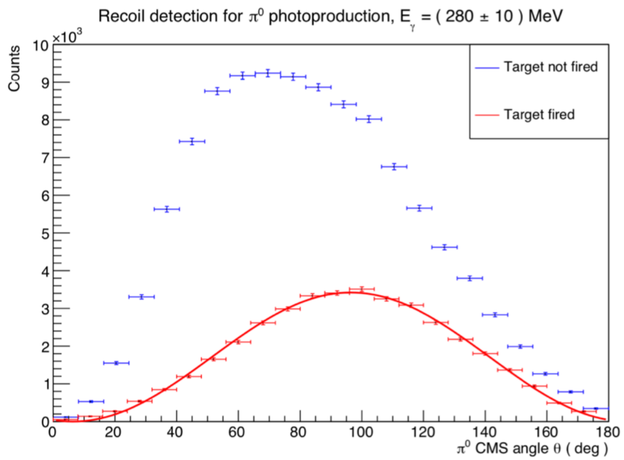

If the target fired, only free and quasi-free processes are identified. The count rates follow a sine-square distribution.

$$\left(\frac{d\sigma}{d\Omega}\right)_0 \propto \sin^2 \theta_\pi^*$$

D. Drechsel, et al., Medium effects in coherent pion photo- and electroproduction on ^{4}He and ^{12}C, Nucl. Phys. A 660 (1999) 423-438

mbiroth@uni-mainz.de

Compton off the Proton and its Background Processes

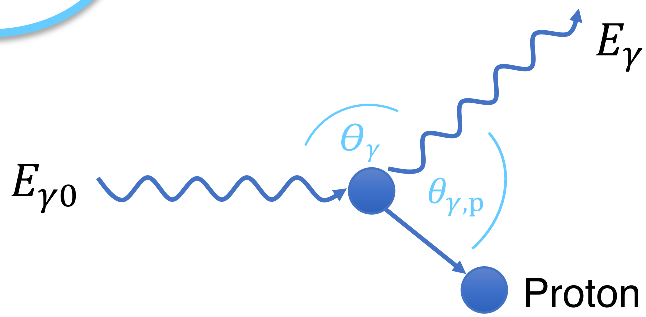

Real Compton scattering is a two-body reaction and has a well defined kinematic.

$$\cos\theta_{\gamma,\mathrm{p}} = \left(1 - \frac{m_p}{E_\gamma}\right) \Big/ \sqrt{1 + \frac{2\,m_p}{E_{\gamma 0} - E_\gamma}}$$

Kinematical cuts on the opening angle require angular resolution.

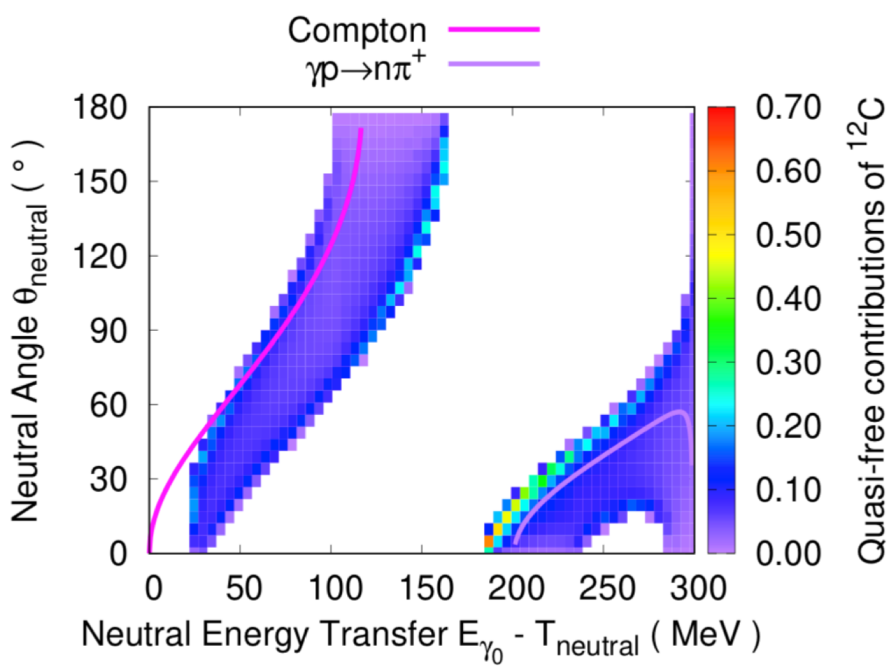

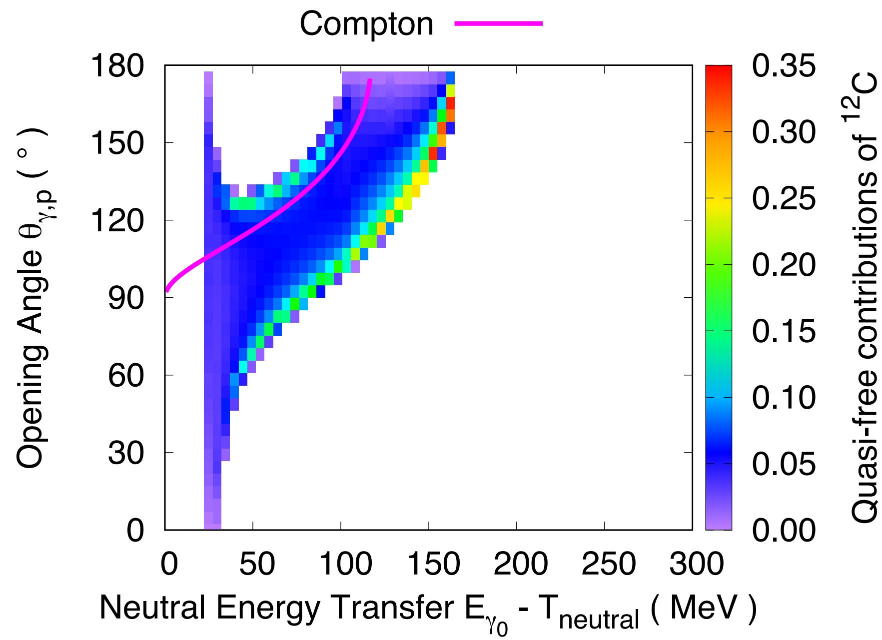

Kinematics are shown for $E_{\gamma 0} = 300\ \mathrm{MeV}$.

Compton off the Proton and Quasi-free Processes

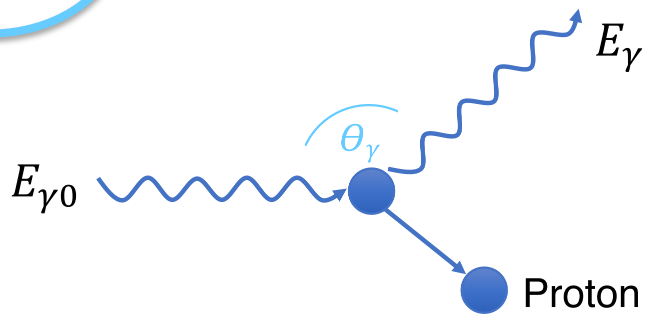

Real Compton scattering is a two-body reaction and has a well defined kinematic.

$$\cos\theta_\gamma = 1 - m_p\left(\frac{1}{E_\gamma} - \frac{1}{E_{\gamma 0}}\right)$$

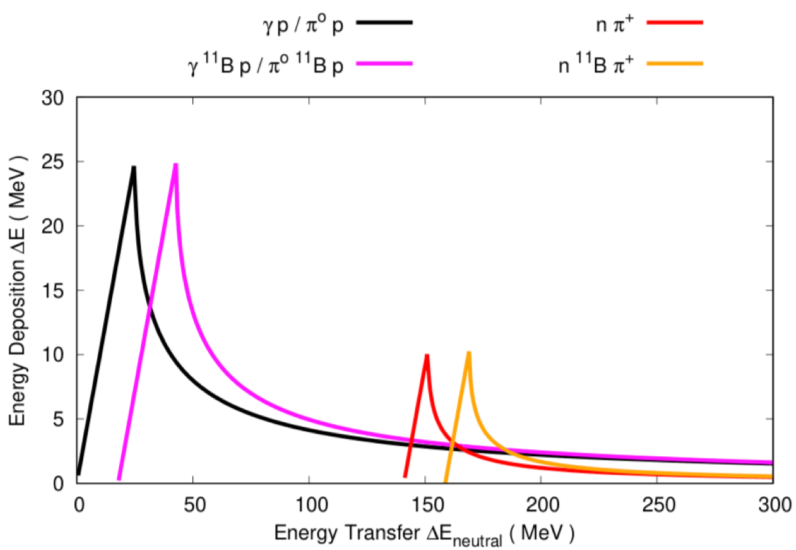

The detection of the recoil proton is essential for the delimitation of background processes with a kinematical overlap.

Critical are quasi-free processes, whereby the proton has the initial Fermi momentum p_F, that is isotropically oriented. The kinetic energy T_p from breakup is reduced by the difference in binding energy.

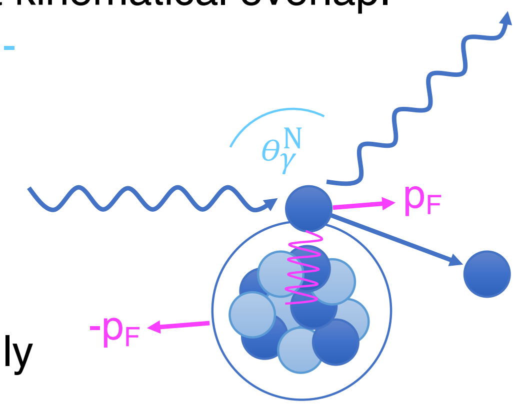

$$T_\mathrm{p} = E_{\gamma 0} - E_\gamma \qquad T_\mathrm{p}^{^{12}\mathrm{C}} = T_\mathrm{p} - \left(m_\mathrm{p} + \sqrt{m_{^{11}\mathrm{B}}^2 + p_{^{12}\mathrm{C}}^2} - m_{^{12}\mathrm{C}}\right) \cong T_\mathrm{p} - 16\ \mathrm{MeV}$$

Compton off the Proton and Quasi-free Processes

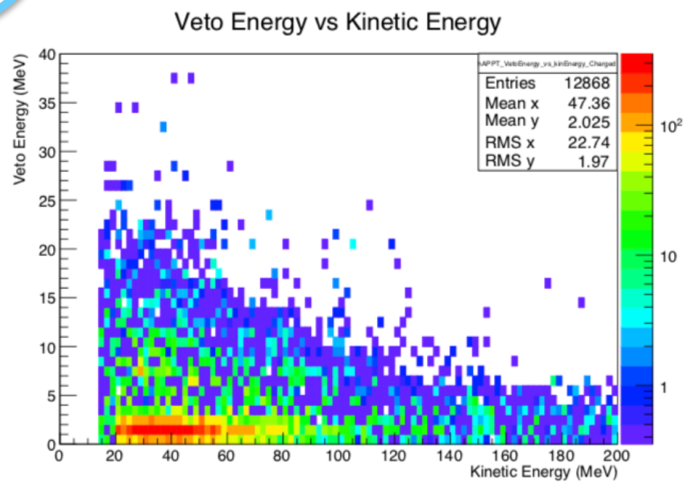

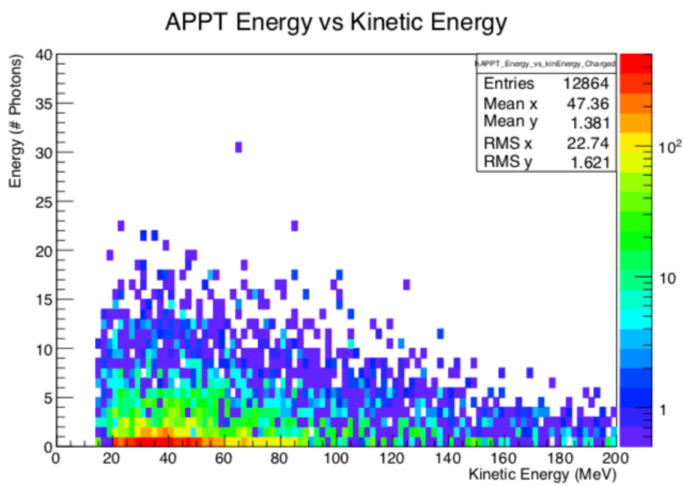

Real Compton scattering is a two-body reaction and has a well defined kinematic.

$$\cos\theta_\gamma = 1 - m_p \left(\frac{1}{E_\gamma} - \frac{1}{E_{\gamma 0}}\right)$$

The detection of the recoil proton is essential for the delimitation of background processes with a kinematical overlap. Critical are quasi-free processes, whereby the proton has the initial Fermi momentum p_F, that is isotropically oriented. The kinetic energy T_p from breakup is reduced by the difference in binding energy.

$$T_p = E_{\gamma 0} - E_\gamma \qquad T_p^{^{12}C} = T_p - \left(m_p + \sqrt{m_{^{11}B}^2 + p_{^{12}C}^2} - m_{^{12}C}\right) \cong T_p - 16\ \mathrm{MeV}$$

Light Output of the Polarizable Scintillator

The electron radical density effects also the light output of the scintillator.

Component	Wavelength of max. absorption	Wavelength of max. emission
PPO/2,5-Diphenylloxazole	303 nm	358 nm
Dimethyl-POPOP	360 nm	411 nm

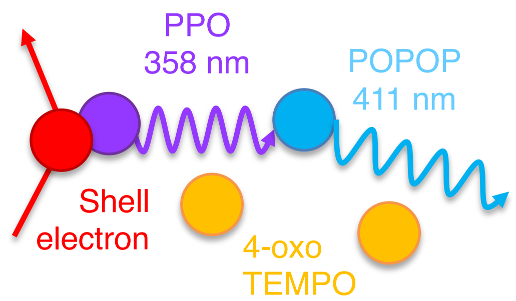

The radical deteriorates the quantum efficiency to 50% of a standard plastic scintillator or even lower, since wavelengths within the Stokes Shift does not excite the POPOP.

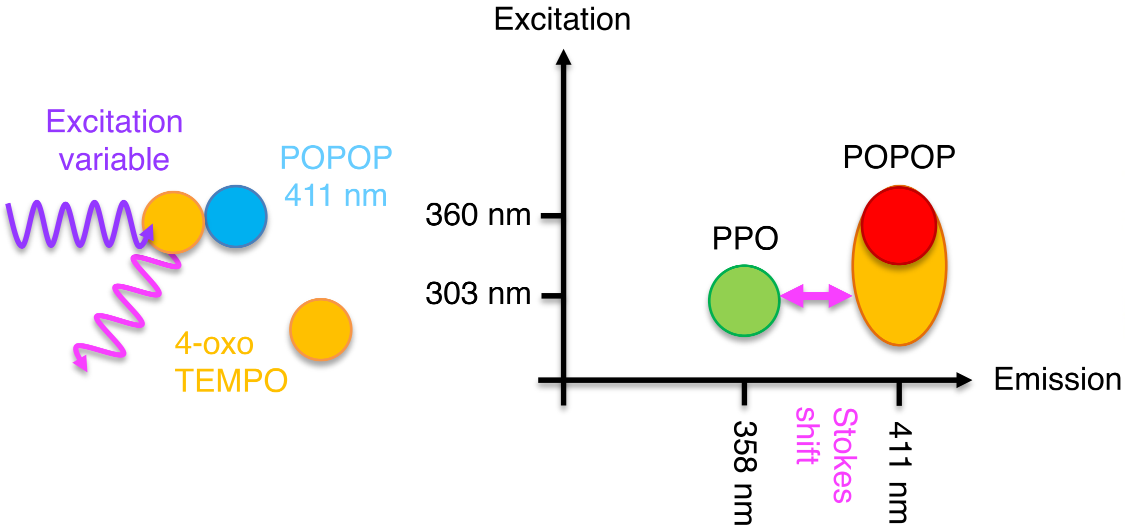

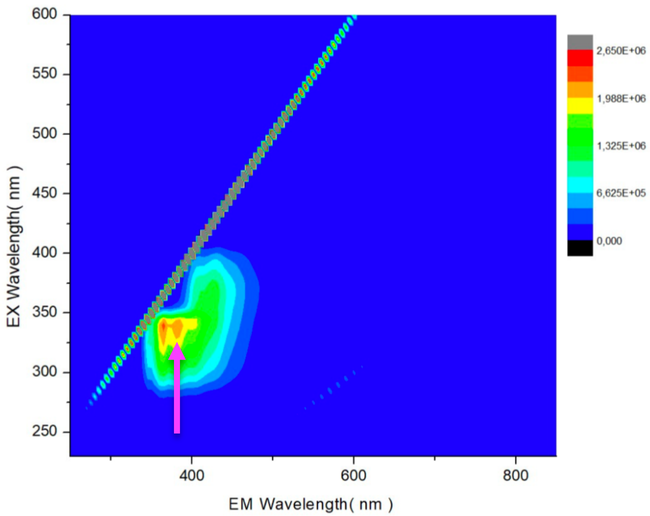

Maik Biroth, Institute of Nuclear Physics, Mainz, Germany
mbiroth@uni-mainz.de

Electronics and Data Acquisition

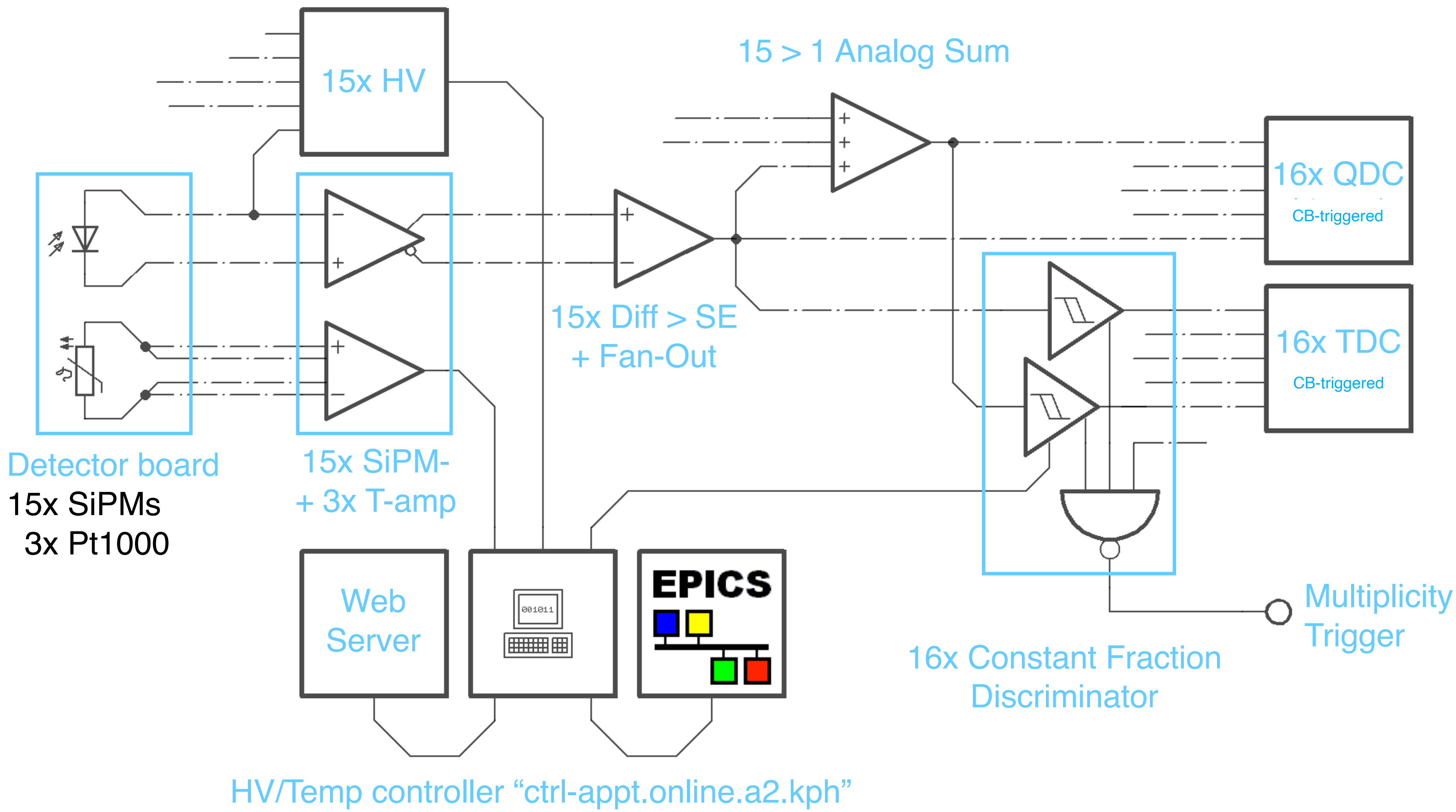

Appendix – Angular Resolution

Indication for Angular Resolution

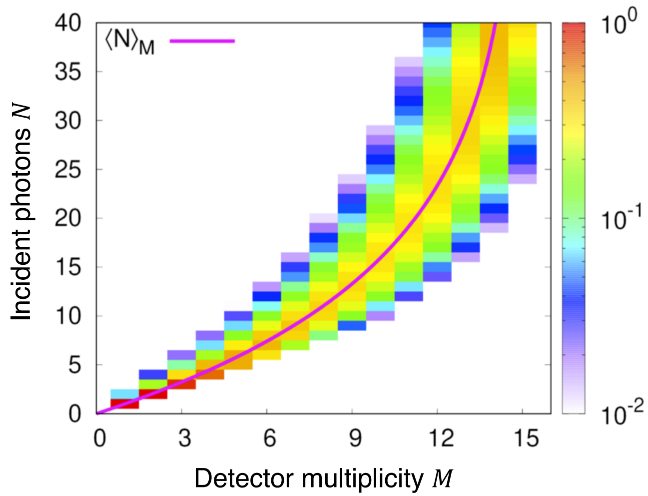

If N photons are unitary distributed over 15 detectors, then $P_{M,N}$ is the probability distribution for M fired detectors.

$$P_{M,N} = \sum_{m=0}^{M} (-1)^m \binom{15}{M} \binom{M}{m} \left(\frac{M-m}{15}\right)^N$$

$\langle M \rangle_N = 15\,(1-(1-1/15)^N)$ is the most probable number of involved detectors.

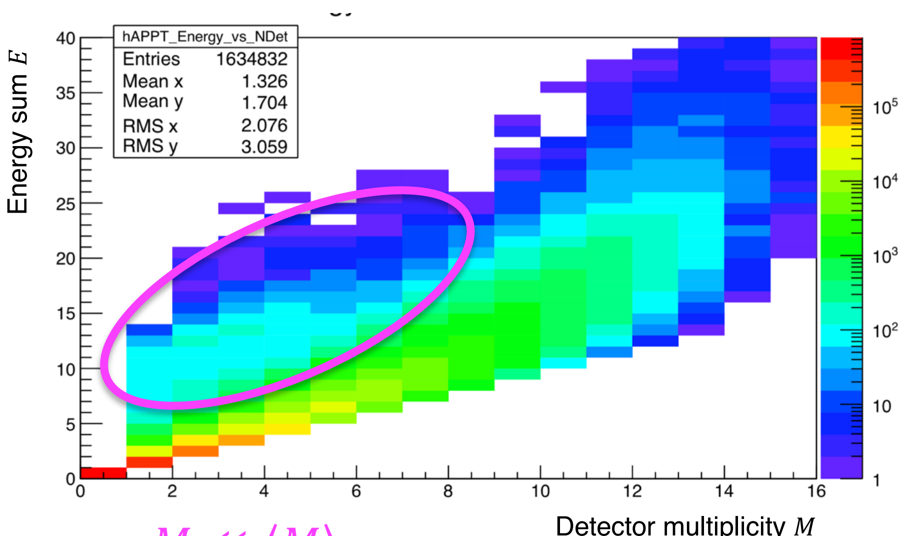

$M \ll \langle M \rangle_N$

The measured target energy with respect to the detector multiplicity showed higher intensities distributed over less detectors than expected statistically.

Maik Biroth, Institute of Nuclear Physics, Mainz, Germany

mbiroth@uni-mainz.de

Indication for Angular Resolution

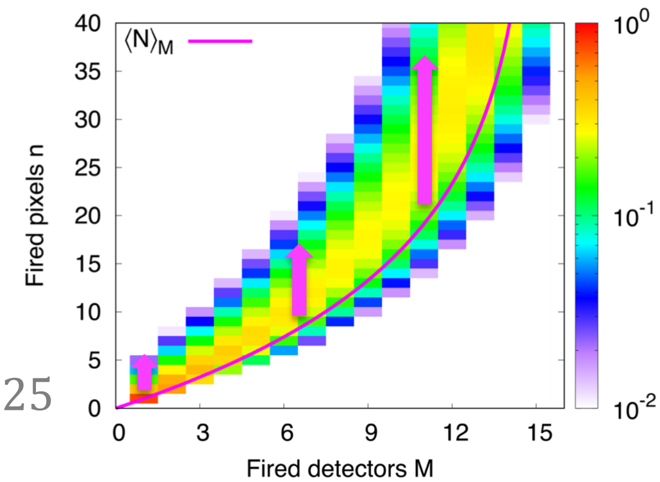

$q := 0.25$

If N photons are unitary distributed over 15 detectors, then $P_{M,N}$ is the probability distribution for M fired detectors.

$$P_{M,N} = \sum_{m=0}^{M} (-1)^m \binom{15}{M} \binom{M}{m} \left(\frac{M-m}{15}\right)^N$$

$\langle M \rangle_N = 15\,(1-(1-1/15)^N)$ is the most probable number of involved detectors.

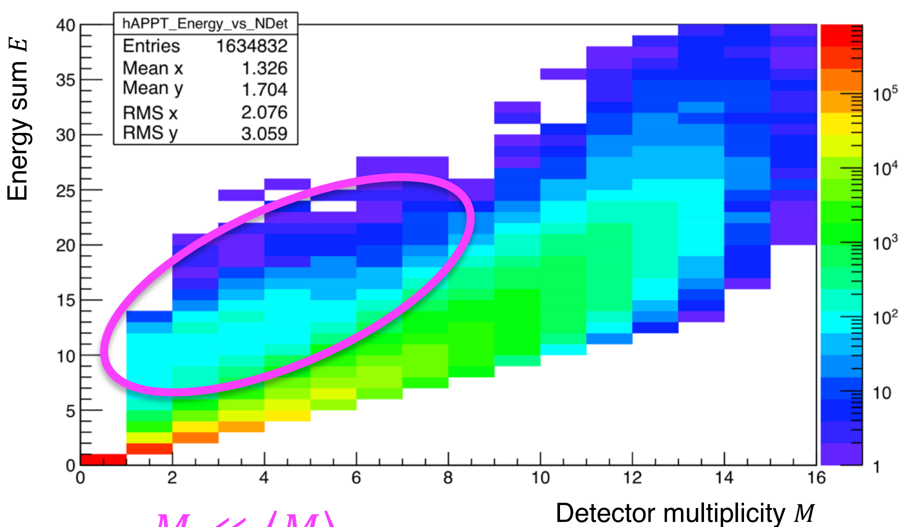

$M \ll \langle M \rangle_N$

Even considering crosstalk $X_{N,n}$ with the pixel-to-pixel crosstalk probability q does not reproduce the result.

$$X_{N,n} = \binom{n}{N} (1-q)^{N+1}\, q^{n-N}$$

Firing pixels: $n = \dfrac{N+q}{1-q} \cong \dfrac{N}{1-q}$

Factorization of the Light Output

The intensity distribution $\mathrm{d}I/\mathrm{d}x$ of a charged track inside the scintillator stack can be factorized in a geometrical fill factor f, the energy loss in a solid scintillator $\mathrm{d}E/\mathrm{d}x$, and the light transport properties Ψ with respect to the azimuthal angle ϕ.

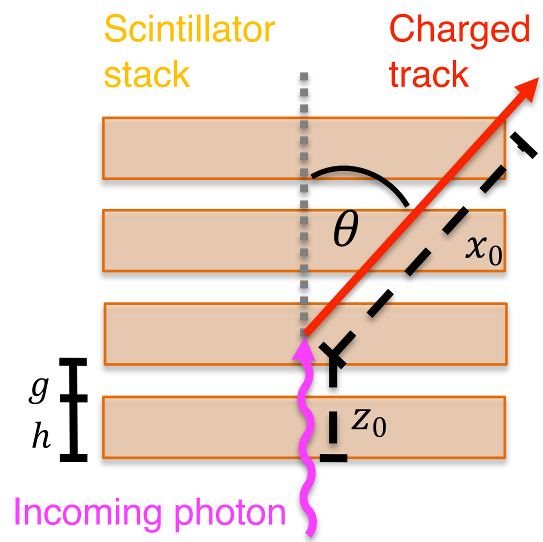

$$\frac{\mathrm{d}I}{\mathrm{d}x} \propto -f\,\frac{\mathrm{d}E}{\mathrm{d}x}\,\Psi$$

Caused by the finite stack height H and the disk radius R the maximum path length x_0 is limited with respect to the polar angle θ and the penetration depth z_0.

$$x_0 = \frac{R}{\sin\theta} \times \begin{cases} (H - z_0)\ \tan\theta & \big|\, 0 \le \theta \le \theta_{\rightarrow} \\ 1 & \big|\, \theta_{\rightarrow} \le \theta \le \theta_{\leftarrow} \\ -z_0 \tan\theta & \big|\, \theta_{\leftarrow} \le \theta \le \pi \end{cases}$$

$$\theta_{\rightarrow} = \tan^{-1} R/(H - z_0)$$

$$\theta_{\leftarrow} = \pi - \tan^{-1} R/z_0$$

Fill factor of the Scintillator Stack

Scintillator disks of height h are separated by gaps g. The fill-factor f gives the effective length of a track (x_0, θ) through the target volume in contrast to a solid scintillator.

Definition: $f_\infty = \dfrac{h}{h+g}$ $\quad \xi = \dfrac{x_0 \cos\theta}{h+g}$ $\quad n = \lceil\, |\xi| - f_\infty/2 \,\rceil$

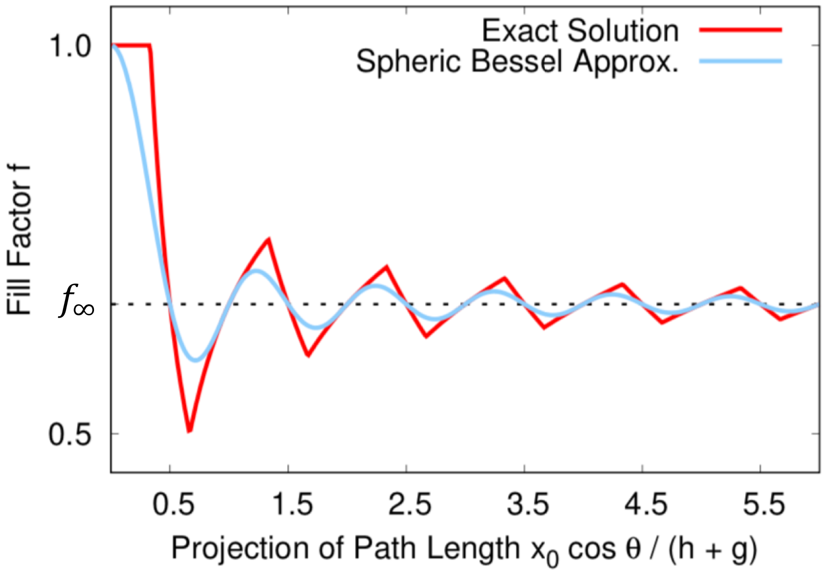

Fill factor with sharp edges:

$$f = \begin{cases} 1 & |\; 0 < |\xi| \le f_\infty/2 \\ (2n-1)\, f_\infty/2|\xi| & |\; f_\infty/2 < |\xi| \le n - f_\infty/2. \\ 1 - n\,(1-f_\infty)/|\xi| & |\; n - f_\infty/2 < |\xi| \le n + f_\infty/2 \end{cases}$$

Fill factor with Gaussian shaped edges:

$$f_{\mathrm{B}} = f_\infty + (1-f_\infty)\, j_0[2\pi\,\xi] \overset{h\sim g}{\approx} f * G_{\sigma=h}$$

For long paths in forward direction the fill factor converges: $f \to f_\infty$

Spherical Bessel function $j_n[x] = (-x)^n\,(1/x\ \mathrm{d}/\mathrm{d}x)^n\ \sin x/x$

Comparison to a Solid Scintillator

- All disks are equally likely, since $P_z \propto \exp - 9z/7\chi_0$ with $\chi_0 = 400\ \mathrm{mm}$

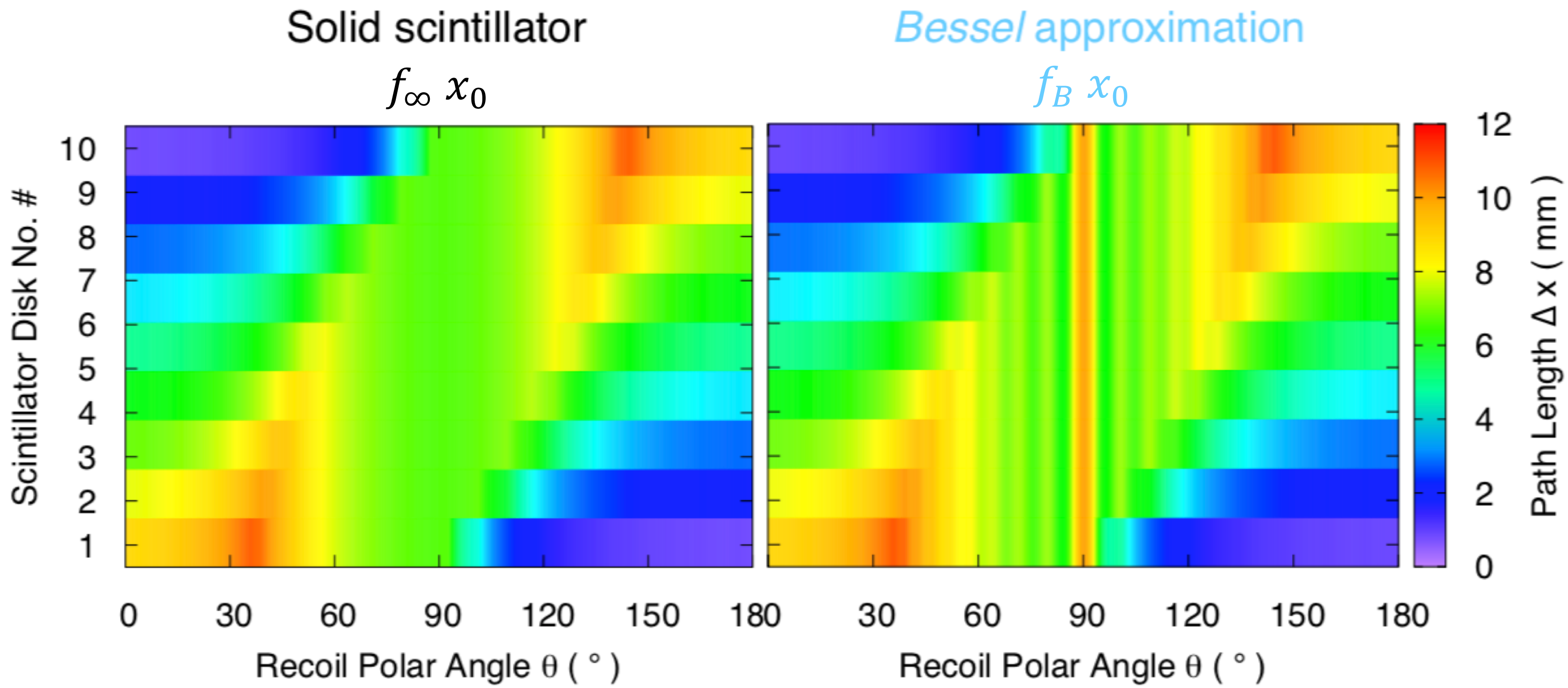

- High sensitivity under $\theta \sim 90°$ on the scintillator disk of incidence is assumed to vanish under multiple scattering

$$\Delta\theta \approx \frac{z_\mathrm{p}\,\psi}{2\,T_\mathrm{p}} \sqrt{\frac{\Delta x}{\chi_0}} \left(1 + \alpha \ln \frac{\Delta x}{\chi_0}\right)$$

Approximation: $c\,p\,\beta \sim 2\,T$, Values for calculation: $\psi = 13.6\ \mathrm{MeV\ m^{-1}}$, $\alpha = 0.038$

Energy Deposition in the Scintillator

Bethe formula describes mean energy loss by inelastic collisions with the shell electrons for heavy particles in thick absorbers.

$$\left\langle\frac{\mathrm{d}T}{\mathrm{d}x}\right\rangle = -\frac{\mathrm{d}\epsilon}{\mathrm{d}x}\,\frac{1}{\beta^2}\cdot\left(\frac{1}{2}\,\ln\left[\kappa^2\,\frac{\Delta T_{\max}}{2m_\mathrm{e}}\gamma^2\beta^2\right]-\beta^2-C\right)$$

Assuming low kinetic energy $\beta^2 \approx 2T\,/\,m_\mathrm{p}$ leads to an explicit, homogenous differential equation of the first order.

$$\left\langle\frac{\mathrm{d}T}{\mathrm{d}x}\right\rangle_{\beta\ll 1} \approx -\frac{\mathrm{d}\epsilon}{\mathrm{d}x}\cdot\ln\left[\kappa\,\frac{2\,T}{m_\mathrm{p}}\right]\cdot\frac{m_\mathrm{p}}{2\,T}$$

Solving this equation yields the mean kinetic energy $\langle T\rangle$ with respect to the path length *x*.

$$\langle T\rangle = \frac{m_\mathrm{p}}{2\,\kappa}\cdot\sqrt{\mathrm{li}^{-1}\left[2\,\kappa^2\,\frac{\mathrm{d}\epsilon}{\mathrm{d}x}\,\frac{\langle d\rangle - x}{m_\mathrm{p}}\right]}$$

Specific energy loss
$\mathrm{d}\epsilon/\mathrm{d}x = 4\pi\, n_\mathrm{e}\, r_\mathrm{e}^2\, m_\mathrm{e}$

Ionizability
$\kappa = 2\, m_\mathrm{e}\,/\,\epsilon_\mathrm{ion}$

Logarithmic integral
$\mathrm{li} = \mathrm{Ei} \circ \ln$

Exponential integral
$\mathrm{Ei}(x) = {}_{-\infty}{}^{x}\!\int \mathrm{d}t\, \exp[t]\,/\,t$

Maximum energy transfer per collision
$\Delta T_{\max} = m_\mathrm{p}\,\gamma^2\,\beta^2\,/\,(\,(m_\mathrm{e}^2+m_\mathrm{p}^2)\,/\,(2\,m_\mathrm{e}\,m_\mathrm{p}) + \gamma\,)$

Range of Protons in Polystyrene

The mean range $\langle d \rangle$ is accomplished after deposition of the full initial kinetic energy T_i.

$$\langle d \rangle = \frac{1}{2\,\kappa^2}\,\frac{m_\mathrm{p}}{\frac{\mathrm{d}\epsilon}{\mathrm{d}x}} \cdot \mathrm{li}\left[\left(\kappa\,\frac{2\,T_\mathrm{i}}{m_\mathrm{p}}\right)^2\right]$$

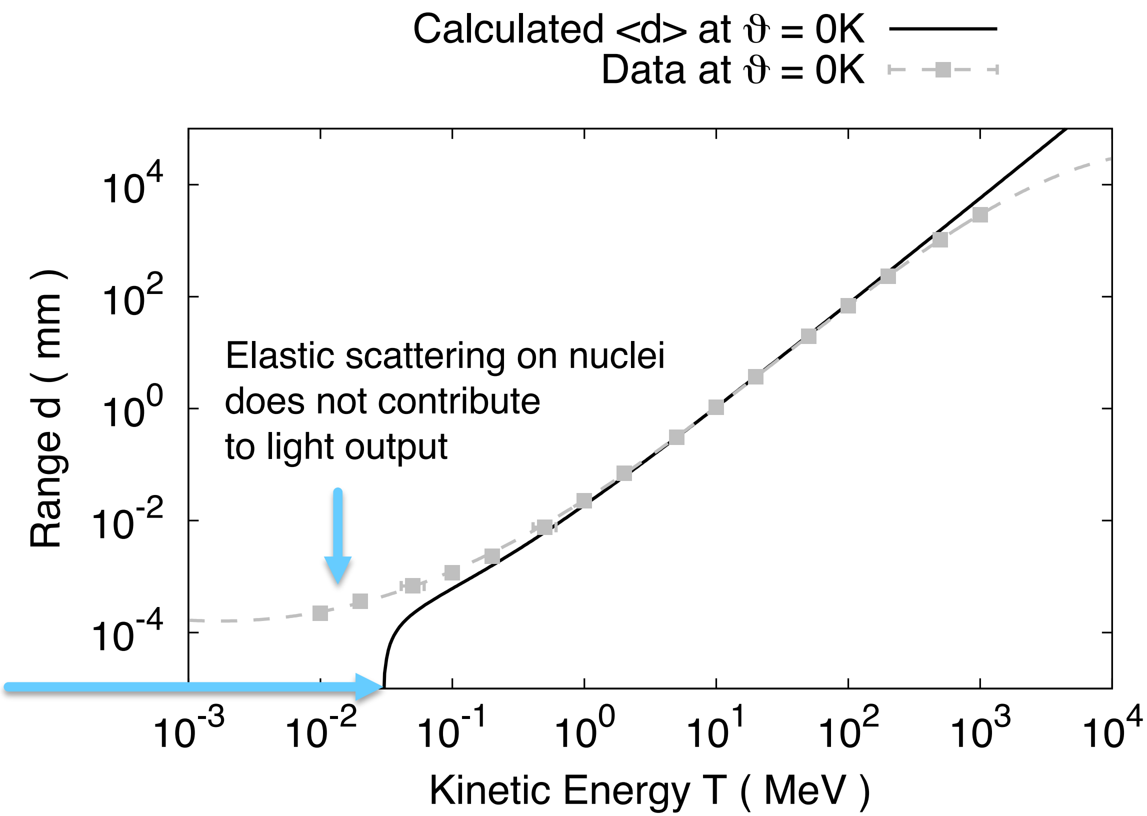

Break-off energy of inelastic scattering on shell electrons

$$\langle T_0 \rangle = \frac{m_\mathrm{p}}{2\,\kappa} \cdot \sqrt{\mathrm{li}^{-1}[0]}$$

Energy Loss and Total Deposition of Protons

Maximum energy deposition along the Bragg peak at $x \sim \langle d \rangle$

$$\frac{\mathrm{d}E}{\mathrm{d}x} = \begin{cases} \frac{\mathrm{d}}{\mathrm{d}x}\langle T \rangle & | x \leq \langle d \rangle \\ 0 & | x > \langle d \rangle \end{cases}$$

$$\Delta E = \begin{cases} T_\mathrm{i} - \langle T \rangle & | x \leq \langle d \rangle \\ T_\mathrm{i} & | x > \langle d \rangle \end{cases}$$

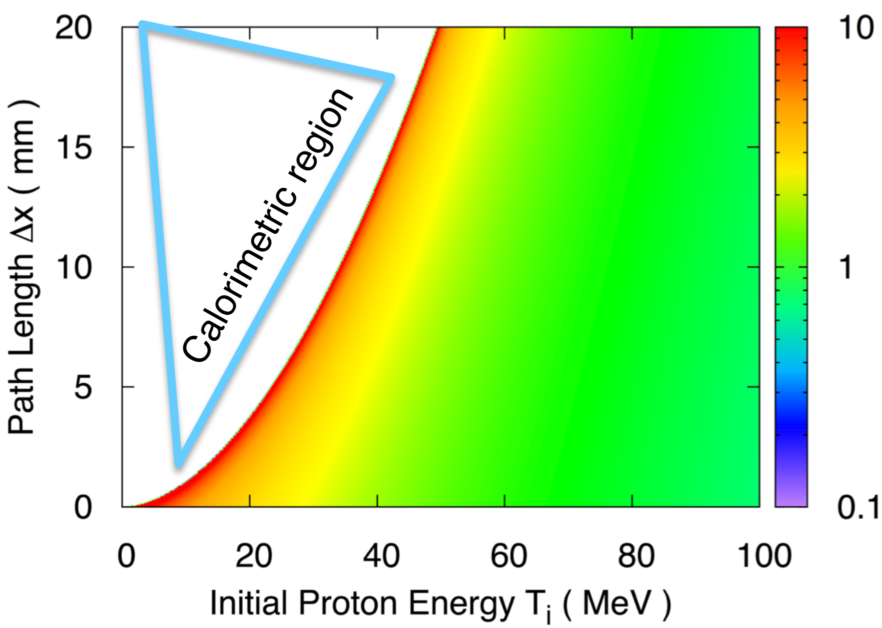

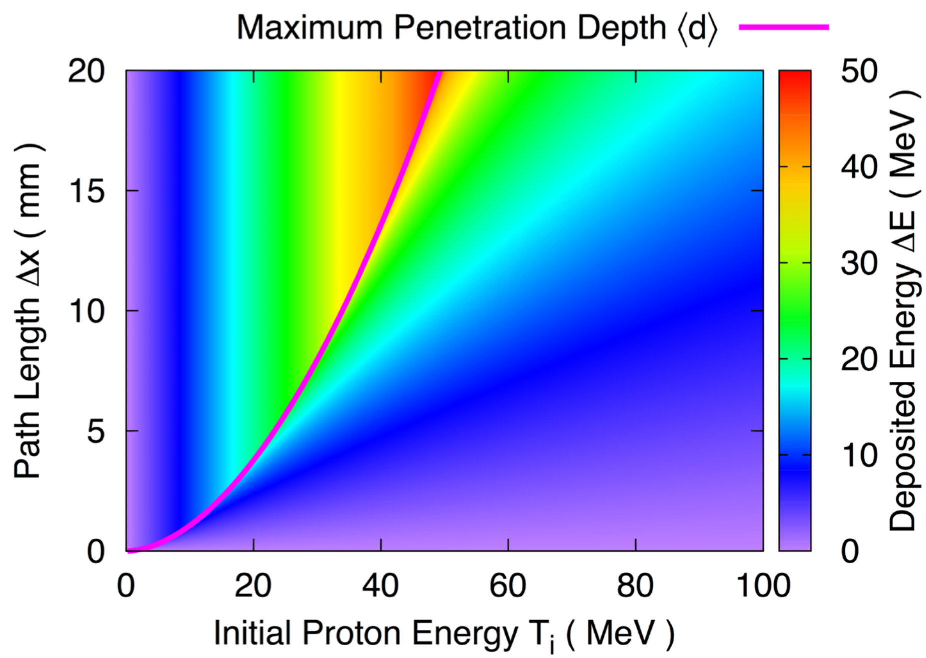

Sources of Light Loss in the Scintillator

The light output of the scintillator depends on two properties:

- Surface quality

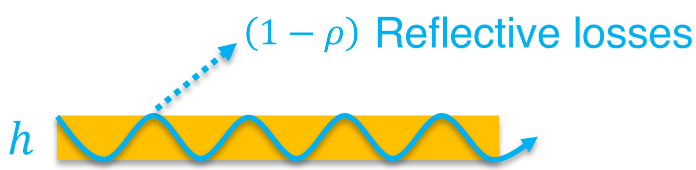

Following the Fresnel equations, the fraction of reflected light ρ with respect to the refractive index n of the scintillator depends on the angle of incidence α.

$$\rho = \frac{1}{2}\left(\left(\frac{1-\xi}{1+\xi}\right)^2 + \left(\frac{1-n^2\xi}{1+n^2\xi}\right)^2\right) \qquad \xi = \sqrt{\frac{n^{-2}-\sin^2\alpha}{1-\sin^2\alpha}}$$

The intensity contribution I_{ref} by reflective losses follows an exponential law with respect to the number of reflections k.

$$I_{\mathrm{ref}} \propto \rho^k \equiv \mathrm{e}^{-\frac{x}{\lambda_{\mathrm{ref}}}} \qquad \lambda_{\mathrm{ref}} = -h\tan\alpha/\ln\rho$$

- Purity of the base material

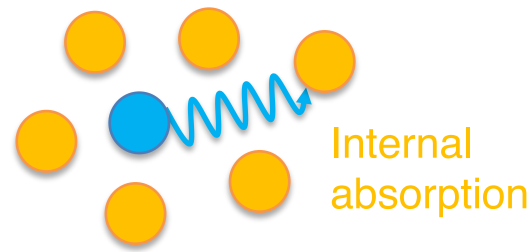

Molecules can become excited by absorbing the scintillation light, that is undetectable. The intensity contribution I_{abs} by internal absorption follows an exponential law with the attenuation length λ_{abs}.

$$I_{\mathrm{abs}} \propto \mathrm{e}^{-\frac{x}{\lambda_{\mathrm{abs}}}}$$

Maik Biroth, Institute of Nuclear Physics, Mainz, Germany
mbiroth@uni-mainz.de

Distribution of the Scintillation Light at the Edge

The radius of the scintillator disks $R = 10\,\mathrm{mm}$ is much larger than their thickness of $\mathrm{h} = 1\,\mathrm{mm}$. Away from the edge, the light output can be described by an exponential law $I = \exp - l_\phi/\lambda$ with the light path l_ϕ to the edge and the combined attenuation length $\lambda^{-1} = \lambda_{\mathrm{ref}}^{-1} + \lambda_{\mathrm{abs}}^{-1}$.

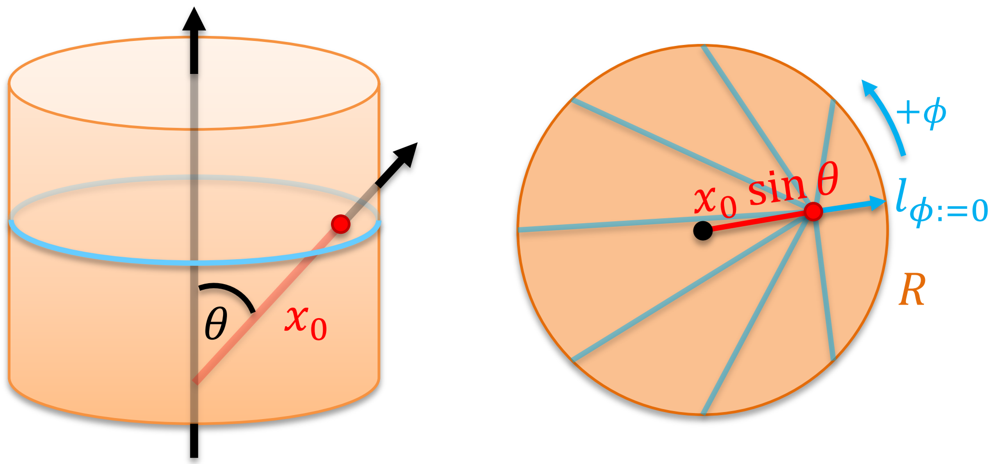

$$l_\phi = \sqrt{R^2 - x_0^2 \sin^2\theta \sin^2\phi} - x_0 \sin\theta\cos\phi \cong R - x_0 \sin\theta\cos\phi$$

Attenuation by reflective losses λ_{ref}, attenuation by absorption λ_{abs}

The energy deposition of protons can be approximated by a continuous energy loss profile, followed by the Bragg peak at zero kinetic energy.

Continuous loss

$$\frac{dE}{dx} = \mathrm{const.}$$

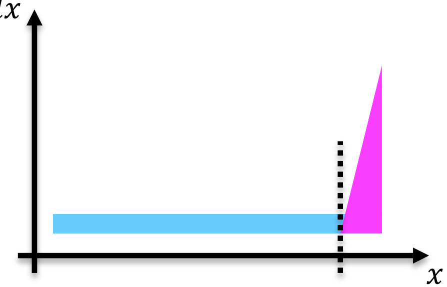

Bragg peak

$$\frac{dE}{dx} \propto \mathrm{D}[x - x_0 \sin\theta]$$

$$\Psi_\theta = \exp\left[-\hat{\delta}_\theta\right] \frac{\exp[\delta_\theta \cos\phi] - 1}{\delta_\theta \cos\phi}$$

Intensity profile

$$\Psi = \exp\left[-\hat{\delta}_\theta\right] \exp[\delta_\theta \cos\phi]$$

$$\delta_\theta = \frac{x_0}{\lambda} \sin\theta \qquad \hat{\delta}_\theta = \frac{R}{\lambda}$$

Log-dynamic range

$$\delta = 2\delta_\theta$$

$$\sigma_\theta = 1/\sqrt{\delta_\theta} \qquad \check{\sigma}_\theta = \sqrt{\lambda/R}$$

Gaussian width

$$\sigma = \sqrt{2/\delta} = 1/\sqrt{\delta_\theta}$$

Parallel Projection Approach

Assumption: The light transport in the tube is lossy because of surface defects. Therefore, only straight tracks survive. Gaussian filtering of the intensity map is able to conserve the finest structure $\check{\sigma}_\theta = \sqrt{\lambda/R}$, that is identical for tracks and Bragg peaks.

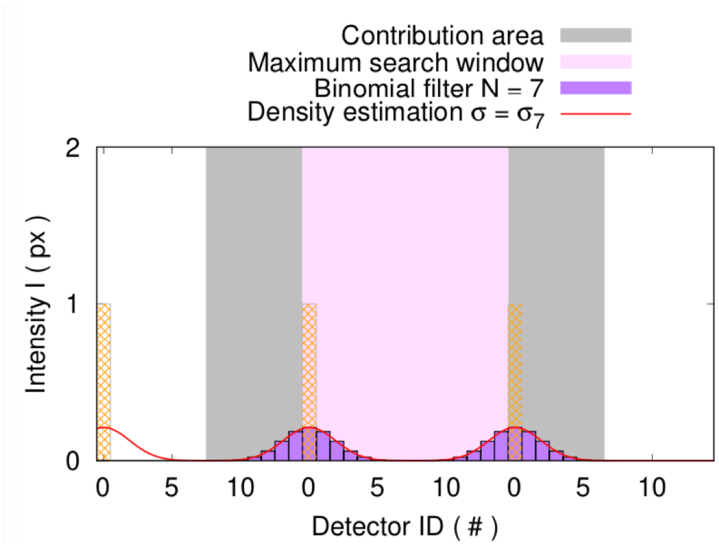

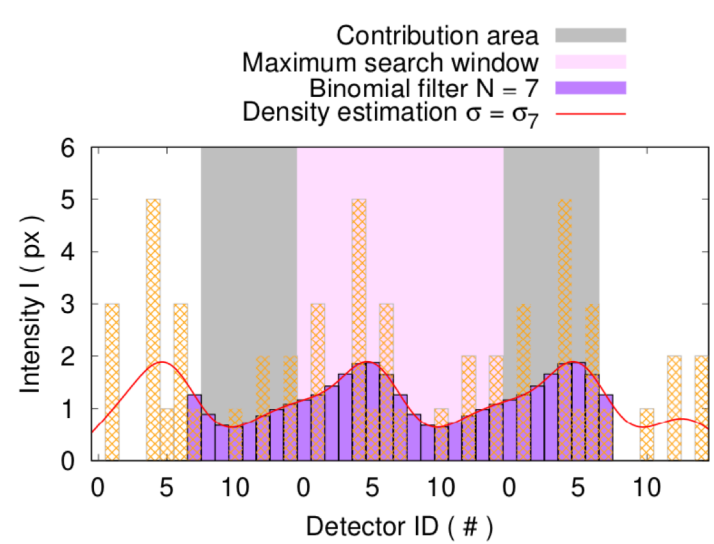

- The maximum of the distribution should be related to the azimuthal angle ϕ.
- The dynamic range of forward/backward tracks should be related to the polar angle $\delta_\theta \propto \tan\theta$.

Maik Biroth, Institute of Nuclear Physics, Mainz, Germany mbiroth@uni-mainz.de

Polar Angular Information from the Intensity Distribution

The correlation between the dynamic range and the missing proton angle from π^0 photoproduction were determined.

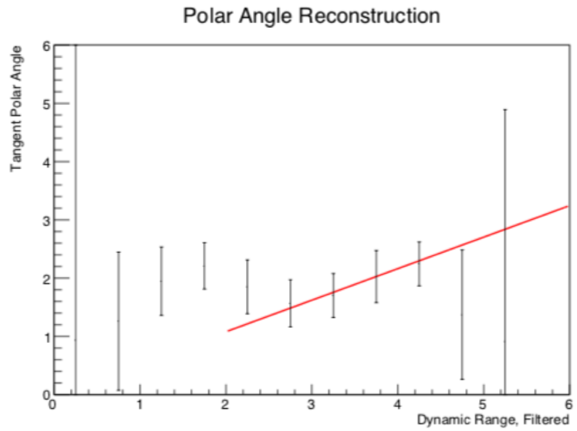

Correlation:

$$\tan\theta / \delta = 0.54(5)$$

Corresponding attenuation:

$$\lambda = 3.9(5)\ \mathrm{mm}$$

Shrinking to a fixed correlation did not remove the ^{12}C background.

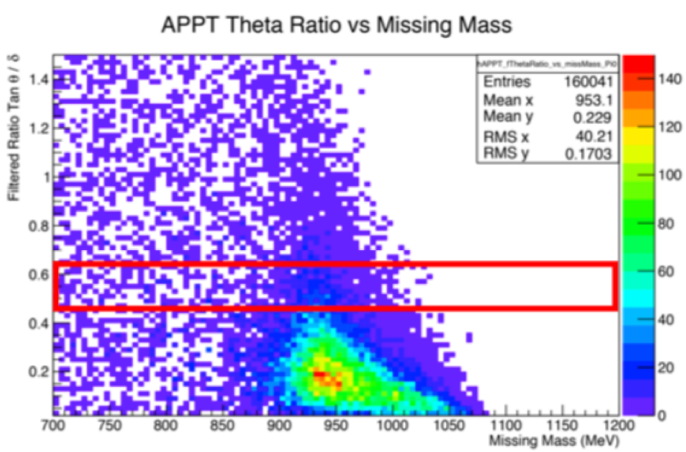

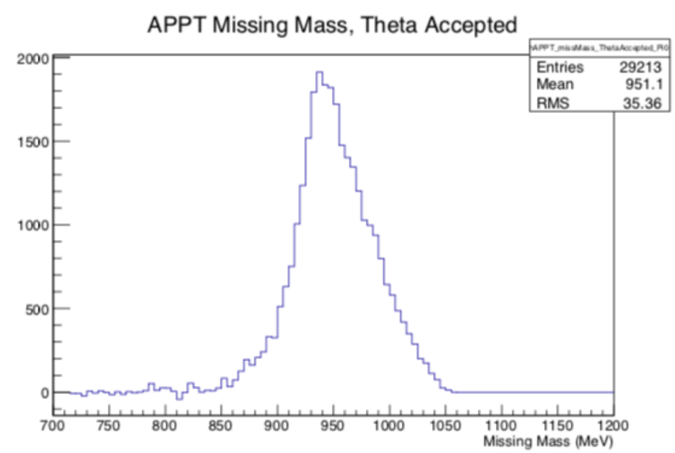

Azimuthal Angular Information from Intensity or Timing

The angular mixing in the beam/light guide tube destroys the azimuthal angular information.

- The maximum of the intensity distribution shows no correlation with ϕ.
- Selecting the first fired detector shows no correlation with ϕ.

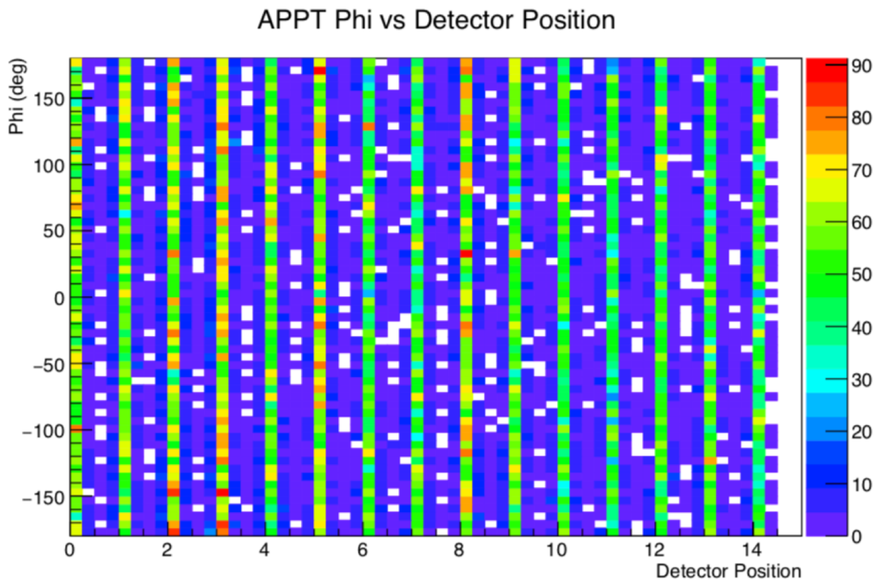

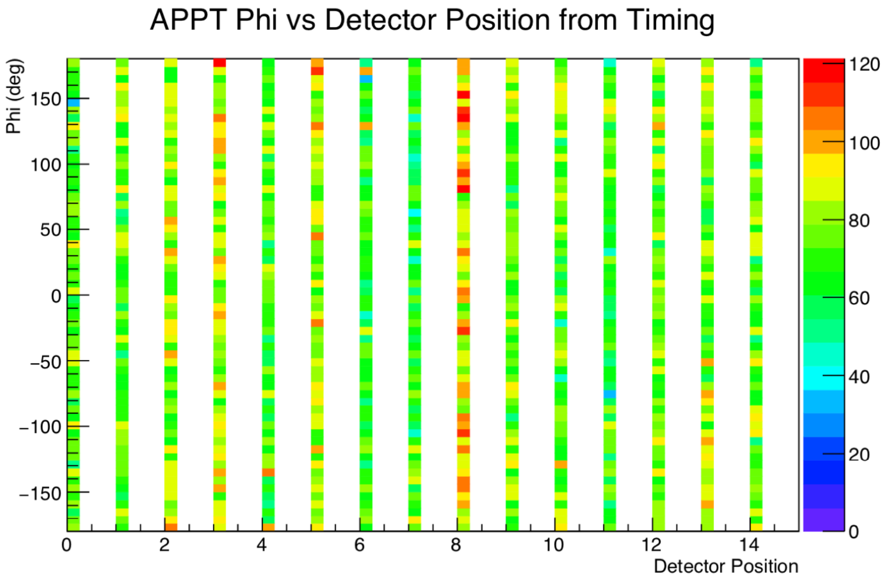

Angular Mapping by the Light Guide Tube

The properties of light transport are derived from a simple model.

Δz is the step z-increment per traveled arc with respect to the effective radius R and the tangential injection angle β:

$$\Delta z = 2\pi\, R \tan\beta$$

$\phi^* \in (-\infty, \infty)$ is the extended detection angle after outrunning the full tube length L_{tube}:

$$\phi^* = 2\pi\,\frac{L}{\Delta z} \qquad \Delta\beta = \pm 1° \;\rightarrow\; \Delta\phi^* = \pm 130°$$

Δt is the time resolution to distinguish between photons with different detection angles:

$$\Delta t = \frac{L}{c_0/n}\sqrt{1+\left(\frac{R}{L}\right)^2 \Delta\phi^{*2}} \qquad \Delta\phi^* = \pm 24° \;\rightarrow\; \Delta t = \pm 38\ \text{fs}$$

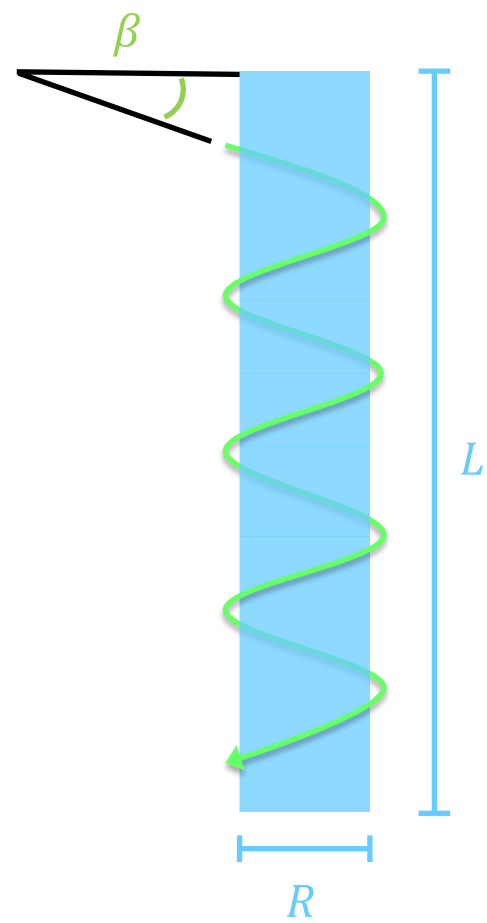

Effective tube radius $R_{\text{tube}} = (R_{\text{out}} + R_{\text{in}})/2 = 11.5\ \text{mm}$, tube length $L_{\text{tube}} = 1.5\ \text{m}$, refractive index of PMMA $n = 1.49$

Maik Biroth, Institute of Nuclear Physics, Mainz, Germany mbiroth@uni-mainz.de

Statistics of the Light Transport in the Tube

The measured intensity I_n is reduced by reflective losses and the initial intensity can be approximated by the most-probable intensity. Therefor the k-th moment of the Binomial distribution $\langle I_n^k \rangle_{\mathrm{MP}}$ can be calculated by:

$$\langle I_n^k \rangle_{\mathrm{MP}} = \sum_{I=I_n}^{\infty} I^k \binom{I}{I_n} p_{\mathrm{tube}}^{I_n} (1 - p_{\mathrm{tube}})^{I-I_n}$$

The most-probable intensity $\langle I_n \rangle_{\mathrm{MP}} > 0$ is obtained from the 1st moment:

$$\langle I_n \rangle_{\mathrm{MP}} := \frac{\langle I_n^1 \rangle_{\mathrm{MP}}}{\langle I_n^0 \rangle_{\mathrm{MP}}} = \frac{1 - p_{\mathrm{tube}}}{p_{\mathrm{tube}}} + \frac{I_n}{p_{\mathrm{tube}}} \qquad \leftrightarrow \qquad p_{\mathrm{tube}} = \frac{I_n + 1}{\langle I_n \rangle_{\mathrm{MP}} + 1}$$

The error of initial and measured intensity are directly correlated and calculated by help of the 2nd moment:

$$\Delta I_n = p_{\mathrm{tube}}\ \Delta I_{n,\mathrm{MP}} = p_{\mathrm{tube}} \sqrt{\frac{\langle I_n^2 \rangle_{\mathrm{MP}}}{\langle I_n^0 \rangle_{\mathrm{MP}}} - \left(\frac{\langle I_n^1 \rangle_{\mathrm{MP}}}{\langle I_n^0 \rangle_{\mathrm{MP}}} \right)^2} = \sqrt{1 - p_{\mathrm{tube}}}\, \sqrt{I_n + 1}$$

For a very lossy ($p_{\mathrm{tube}} \ll 1$) light guide one obtains the same result as from Poisson distribution and the incremented intensity $(I_n + 1)$ is proportional to the most-probable intensity.

$$\lim_{p_{\mathrm{tube}} \to 0} \langle I_n \rangle_{\mathrm{MP}} = \frac{I_n + 1}{p_{\mathrm{tube}}} \qquad \lim_{p_{\mathrm{tube}} \to 0} \Delta I_n = \sqrt{I_n + 1}$$

Intensity Distribution from Monte Carlo

The point-source was placed under the angle of detector 0.

The intensity-weighted path lengths follow a Weibull distribution.

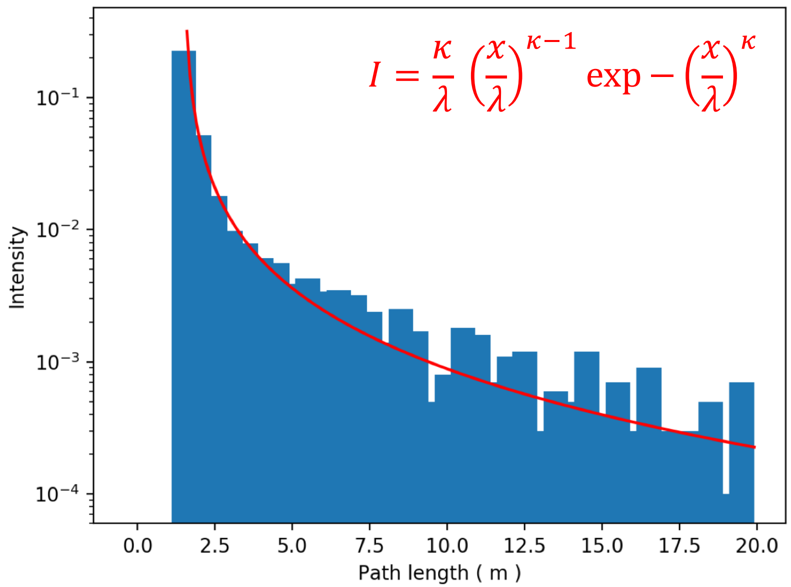

No angular resolution can be achieved with the light guide tube.

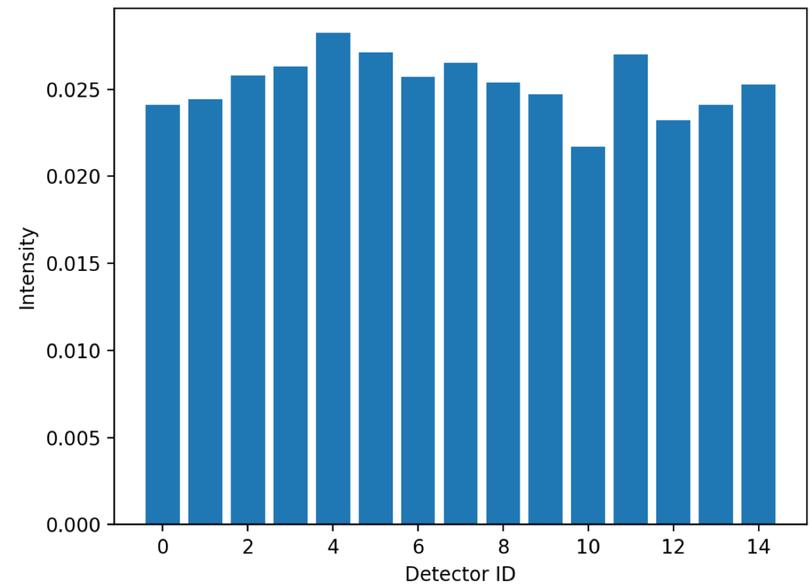

Refractive index of PMMA $n = 1.49$, refractive index of Borosilicate $n = 1.47$

Appendix – SiPM Spectrum and Cryogenic Properties

Study in Optical Detectors

Depending on the placement of the optical detectors, the operational condition change dramatically. Only one single type was matching the requirements:

- Photomultiplier tubes: sensitive to magnetic fields, He diffusion
- Avalanche photodiodes: low internal gain $10^2 - 10^3\ e_0/\gamma$
- Super-conducting nanowires: no sensitivity in the visible range
- Silicon photomultipliers (SiPM): study in cryogenic characteristics needed

The development of the differential transimpedance SiPM amplifiers with pseudo-floating shielding enabled the required 2.5 m connection cables between SiPM and amplifier:

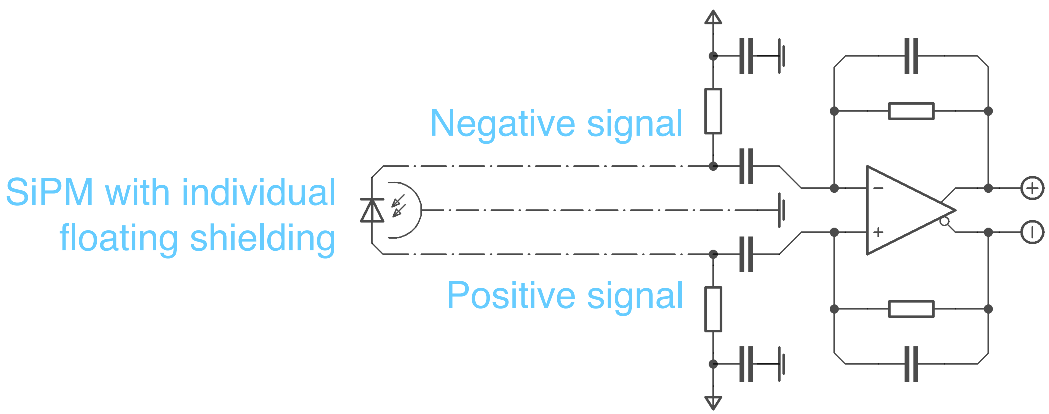

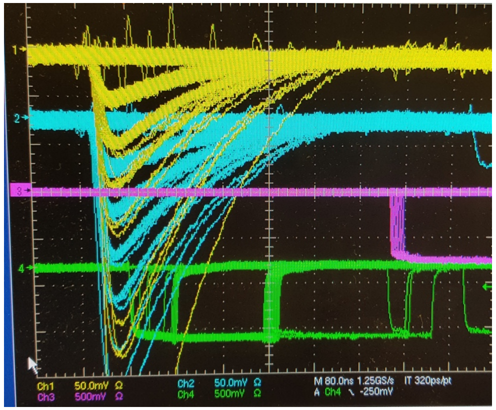

- The differential readout increases the signal-to-noise ratio by a factor $\sqrt{2}$.
- The fully-differential topology provides excellent common-mode noise suppression.

M. Biroth, et al., NIM A 787 (2015) 185-188

Maik Biroth, Institute of Nuclear Physics, Mainz, Germany
mbiroth@uni-mainz.de

Study in Statistical Properties of SiPMs

The number of fired pixels n of a SiPM with respect to the number of incident photons i is increased by the (optical) crosstalk.

The combinatorics of the fired pixels composition is calculated by the Binomial coefficient. The probability of a specific composition follows a Binomial distribution $B_{i,n}$ with the crosstalk probability q.

$$B_{i,n} = \binom{n}{i} (1-q)^{i}\, q^{n-i}$$

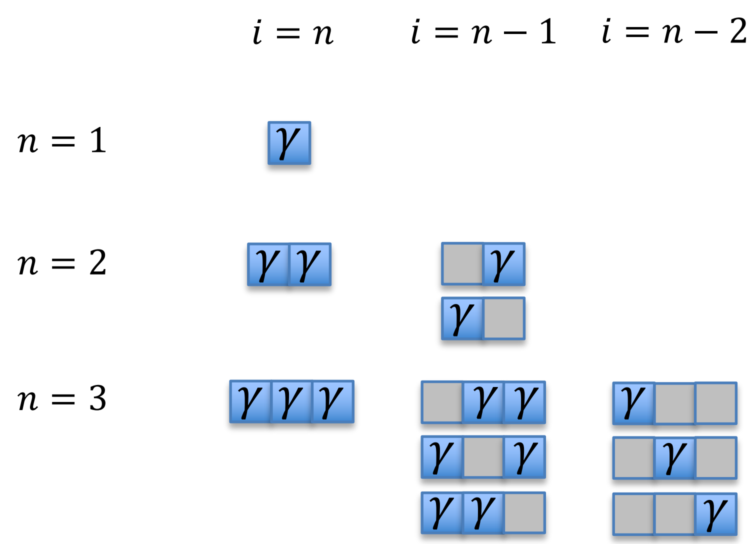

Dark count events are always triggered by a single thermally activated pixel. The spectrum follows for $i = 1$:

$$D_n = \mathcal{N}\, B_{1,n} = n\,(1-q)^2\, q^{n-1}$$

Extraction of SiPM Parameters from Low-intensity Spectra

The fluctuation of a coherent light source in emitting i photons follows a Poisson distribution $P_i = \mathrm{e}^{-\lambda}\,\lambda^i/i!$ with the mean number of photons λ. The probability of an event with n fired pixels is given by the probability Ω_n.

$$\Omega_n = \mathcal{N}\sum_{i=1}^{n} P_i\,B_{i,n} = \frac{(1-q)\,q^n}{\mathrm{e}^{\lambda}-1}\left(\mathcal{L}_n\left[-\frac{1-q}{q}\,\lambda\right]-1\right)$$

The spectrum S_n is obtained by considering the charge distribution of the pedestal distribution G_0 with the noise σ_0 and the n-pixel peaks G_n.

$$S_n = \mathrm{e}^{-\lambda}\,G_0 + \left(1-\mathrm{e}^{-\lambda}\right)\,\sum_n \Omega_n\,G_n$$

The mean charge of an n-pixel event appears as the n-fold of the Gaussian distributed single-pixel gain g_{SP}. The variation of the single-pixel gain σ_{SP} leads to a broadening of the n-pixel distribution by the factor $\sqrt{n}$.

$$G_n \propto \exp -\frac{1}{2}\,\frac{(Q-n\,g_{\mathrm{SP}})^2}{\sigma_0^2+n\,\sigma_{\mathrm{SP}}^2}$$

$$g_{\mathrm{SP}} = \langle g_j \rangle$$

$$\sigma_{\mathrm{SP}} = \sqrt{\langle g_j^2\rangle - \langle g_j\rangle^2}$$

Laguerre polynomials $\mathcal{L}_n = \sum_{i=0}^{n}\binom{n}{k}\,(-x)^k/k!$

Number of incident photons $\lambda = \eta\,\lambda_{\mathrm{initial}}$ is reduced by the Photon detection efficiency (PDE) η

Overview of Important SiPM Parameters

Charge spectra at single-photon intensity

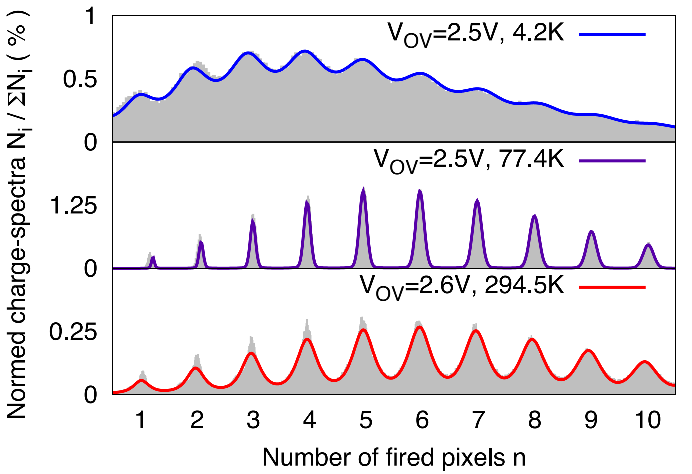

Optimum peak resolution

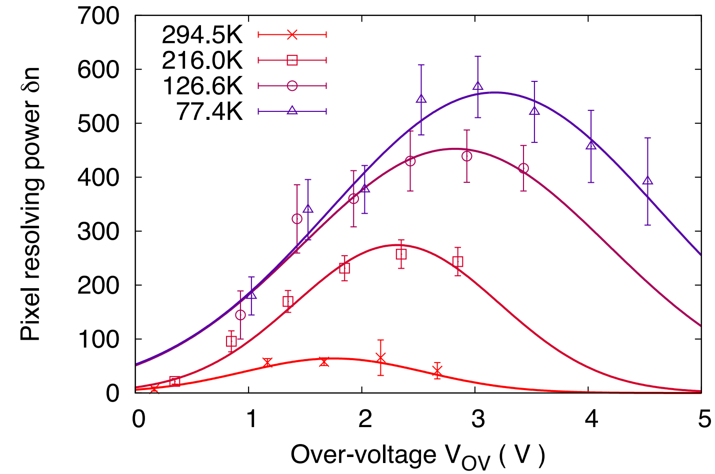

Optical cross and band-band tunneling

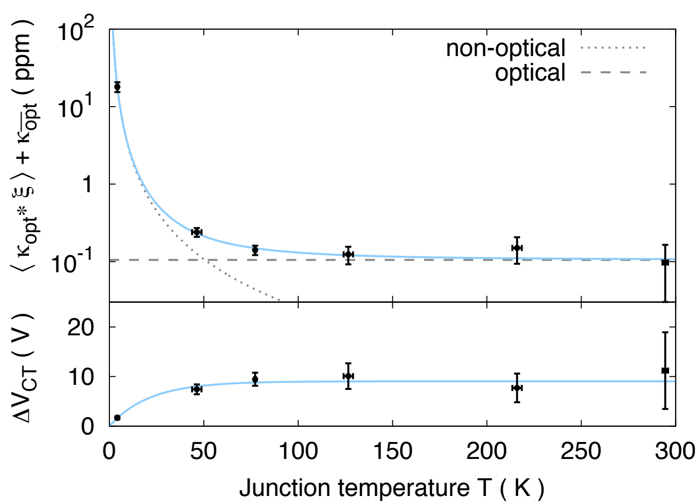

Photo-detection efficiency

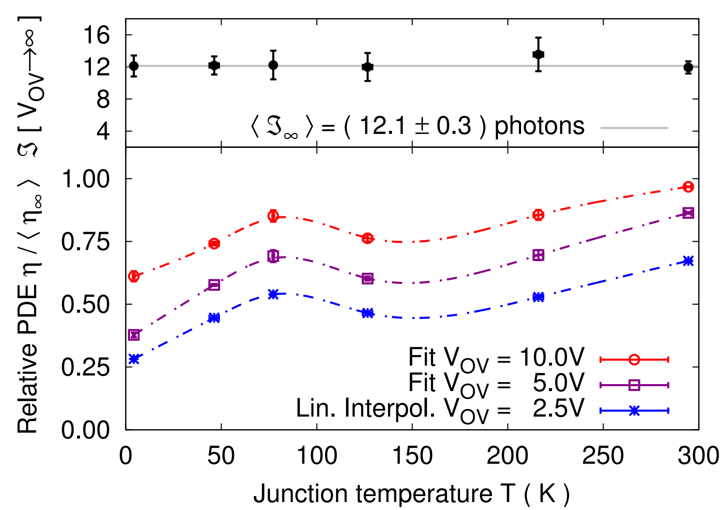

SiPM Spectrum for Large Intensities

Poisson and Binomial distribution can be approximated by Gaussian distributions for large intensities $\lambda \to \infty$ and many fired pixels $n \to \infty$ respectively:

$$P_{i,\lambda\to\infty} \propto \exp - \frac{1}{2}\left(\frac{i-\lambda}{\sqrt{\lambda}}\right)^2 \qquad B_{i,n\to\infty} \propto \exp - \frac{1}{2}\left(\frac{i-(1-q)\,n}{\sqrt{q\,(1-q)\,n}}\right)^2$$

The probability distribution can be calculated as a continuous integral. It has a Gaussian form with the central intensity μ and the standard deviation σ:

$$P_n \cong \mathcal{N} \int_0^n \mathrm{d}i \; P_{i,\lambda\to\infty}\, B_{i,n\to\infty} \cong \frac{1}{\sqrt{2\pi\,\sigma^2}} \exp - \frac{1}{2}\left(\frac{n-\mu}{\sigma}\right)^2$$

$$\mu = \frac{\lambda}{1-q} \qquad \sigma = \sqrt{\frac{\mu + n\,q}{1-q}} \overset{n\sim\mu}{\cong} \sqrt{\frac{1+q}{1-q}\,\mu}$$

Maik Biroth, Institute of Nuclear Physics, Mainz, Germany mbiroth@uni-mainz.de

Appendix – Polarization Relaxation, Measurement, Build-up

Electron Spin-Lattice Relaxation

The lattice $\mathcal{H}_\mathrm{L}$ can be treated as one dimensional oscillator with creation $a_j^\dagger$ and annihilation a_j operators of optical phonon modes $\hbar\omega_{\mathrm{ph},j}$.

$$\mathcal{H}_\mathrm{L} = \sum_j \hbar\omega_{\mathrm{ph},j}\left(a_j^\dagger a_j + \tfrac{1}{2}\right)$$

The spin-lattice coupling $\mathcal{H}_\mathrm{SLC}$ with the complex coupling constants $\Omega^\pm$ enables spin flips by phonon absorption and emission.

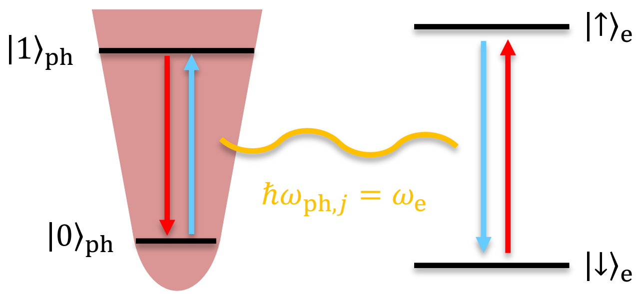

$$\mathcal{H}_\mathrm{SLC} \propto \sum_j \left(\Omega^- \sigma_\mathrm{e}^+ a_j + \Omega^+ \sigma_\mathrm{e}^- a_j^\dagger\right)$$

$$\mathcal{H}_\mathrm{SLC}\,|n\rangle_\mathrm{ph}\,|\uparrow\rangle_\mathrm{e} = |n+1\rangle_\mathrm{ph}\,|\downarrow\rangle_\mathrm{e}$$

$$\mathcal{H}_\mathrm{SLC}\,|n\rangle_\mathrm{ph}\,|\downarrow\rangle_\mathrm{e} = |n-1\rangle_\mathrm{ph}\,|\uparrow\rangle_\mathrm{e}$$

The statistic nature of the process leads to a relaxation of the electron polarization P_e to the thermal equilibrium polarization $P_\mathrm{TE,e}$ with the electron spin-lattice relaxation time $\tau_{1,\mathrm{e}}$.

$$\frac{\partial}{\partial t} P_\mathrm{e} = -\frac{1}{\tau_{1,\mathrm{e}}}\left(P_\mathrm{e} - P_\mathrm{TE,e}\right) \qquad \tau_{1,\mathrm{e}} \propto \frac{P_\mathrm{TE,e}}{\omega_\mathrm{e}^5}$$

Nuclear Spin-Lattice Relaxation

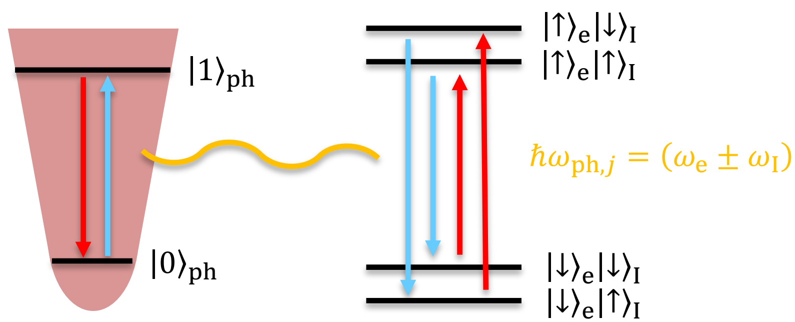

Direct nuclear spin-lattice relaxation induces a coupled electron-nuclear spin flip under absorption or emission of a phonon. Indirect relaxation takes place by dipolar coupling of electron and nuclear spins.

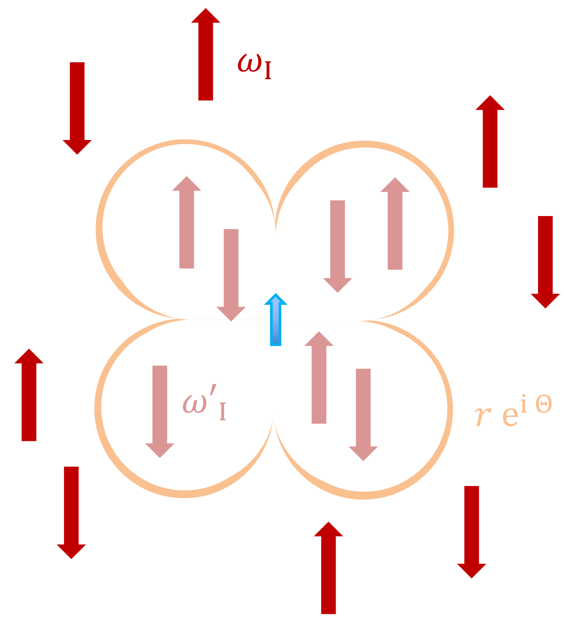

Within the diffusion boundary $\vec{r}$ with $n = 4$, the nuclear resonance frequency $\omega'_{\mathrm{I}} \neq \omega_{\mathrm{I}}$ is still affected by the dipolar coupling to the electron spin.

$$r := |\vec{r}| \propto \left(\frac{3 \sin^2 \Theta \cos^2 \Theta}{4\,\mathcal{D}} \right)^{1/n}$$

The mutual coupling between nuclear spins inside and beyond the diffusion boundary is reduced. Therefore, the nuclear spin-lattice relaxation time $\tau_{1,\mathrm{I}}$ depends on $\tau_{1,\mathrm{e}}$ to the power $1/n$ with $n \approx 4$.

$$\tau_{1,\mathrm{I}} \propto \frac{\omega_{\mathrm{I}}^2}{1 - P_{\mathrm{TE,e}}^2} \tau_{1,\mathrm{e}}^{1/n} \propto \frac{P_{\mathrm{TE,e}}^{1/n}}{1 - P_{\mathrm{TE,e}}^2} \frac{\omega_{\mathrm{I}}^2}{\omega_{\mathrm{e}}^{5/n}}$$

$$n = 5 \left(2 - \frac{\ln \tau_{1,0} - \ln \tau_{1,\mathrm{HF}}}{\ln B_0 - \ln B_{\mathrm{HF}}} \right)^{-1} = 4.2871(79)$$

Maik Biroth, Institute of Nuclear Physics, Mainz, Germany

mbiroth@uni-mainz.de

Thermal Equilibrium and Transverse Relaxation

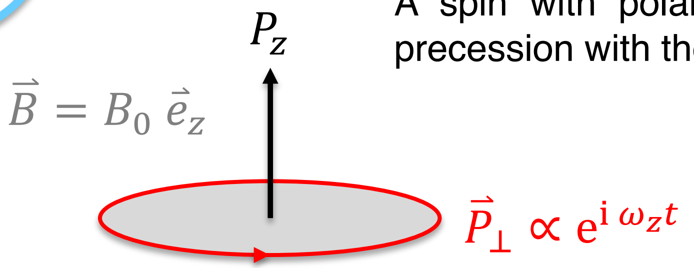

A spin with polarization vector $\vec{P}$ in a magnetic field $\vec{B}$ undergoes precession with the Larmor frequency $\vec{\omega}$ following the Bloch equations.

$$\frac{\partial}{\partial t}\vec{P} = -\vec{\omega} \times \vec{P}$$

The (micro-)canonical ensemble requires a vanishing transverse component $\vec{P}_\perp$ to reach an equilibrium state.

$$\lim_{t\to\infty} \vec{P}_\perp \equiv \vec{o} \qquad \lim_{t\to\infty} P_z \equiv P_{\mathrm{TE}} = \tanh\frac{\hbar\omega_0}{2k_{\mathrm{B}}T}$$

Mutual dipolar coupling enables flipflop transitions $\mathcal{H}_{\mathrm{FF}}$, that lead to homogeneous broadening $\Delta\omega_{\mathrm{FF}}$ of the ω_0. In the time domain the perpendicular polarization decays with the transverse spin-spin relaxation time τ_2.

$$\mathcal{H}_{\mathrm{FF}} \propto \sum_{j,k} \delta_{j,k}\left(\sigma_j^+\sigma_k^- + \sigma_j^-\sigma_k^+\right)$$

$$\mathcal{H}_{\mathrm{FF}}\,|{\downarrow}\rangle\,|{\uparrow}\rangle = |{\uparrow}\rangle\,|{\downarrow}\rangle$$
$$\mathcal{H}_{\mathrm{FF}}\,|{\uparrow}\rangle\,|{\downarrow}\rangle = |{\downarrow}\rangle\,|{\uparrow}\rangle$$

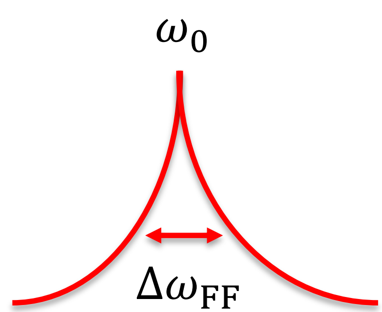

$$\tau_2 = \frac{2}{\Delta\omega_{\mathrm{FF}}}$$

$$\frac{\partial}{\partial t}\vec{P}_\perp = -\frac{1}{\tau_2}\vec{P}_\perp$$

Maik Biroth, Institute of Nuclear Physics, Mainz, Germany
mbiroth@uni-mainz.de

Method of Continuous Wave Polarization Measurement

The spins are exited by a high-frequency field ω_m around the hydrogen resonance $\omega_0 = \gamma_\mathrm{I}\, B_0$ with magnitude $2\omega_1$. The effective field $\vec{\omega}^\mathrm{R}$ in the rotating frame is constant in time.

$$\vec{\omega}_1 = 2\omega_1 \cos\omega_\mathrm{m} t \;\; \vec{e}_x \qquad \underset{\circlearrowright\, \omega_\mathrm{m} t}{\Longrightarrow} \qquad \vec{\omega}^\mathrm{R} \cong \begin{pmatrix} \omega_1 \\ 0 \\ \omega_0 - \omega_\mathrm{m} \end{pmatrix}$$

The excitation adds additional terms to the equation of motion for the polarization P^R in the rotating frame.

$$\frac{\partial}{\partial t} \vec{P}^\mathrm{R} = \begin{pmatrix} -1/\tau_2 & (\omega_0 - \omega_\mathrm{m}) & 0 & 0 \\ -(\omega_0 - \omega_\mathrm{m}) & -1/\tau_2 & \omega_1 & 0 \\ 0 & -\omega_1 & -1/\tau_1 & 1/\tau_1 \end{pmatrix} \begin{pmatrix} \vec{P}^\mathrm{R} \\ \\ P_\mathrm{TE} \end{pmatrix} \coloneqq \vec{o}$$

The static solution yields the complex perpendicular polarization $\bar{P}_\perp$ that is proportional to complex magnetization $\bar{M}_\perp$ with the number of spins N and the gyromagnetic ratio γ.

$$\vec{P}^\mathrm{R} = \frac{P_\mathrm{TE}}{1 + \tau_1\tau_2\omega_1^2 + \tau_2^2(\omega_0 - \omega_\mathrm{m})^2} \begin{pmatrix} \tau_2^2\, \omega_1(\omega_0 - \omega_\mathrm{m}) \\ \tau_2\, \omega_1 \\ 1 + \tau_2^2(\omega_0 - \omega_\mathrm{m})^2 \end{pmatrix}$$

$$\bar{P}_\perp = \left(P_x^\mathrm{R} + j\, P_y^\mathrm{R}\right) \exp j\, \omega_\mathrm{m} t$$

$$\bar{M}_\perp = N\, \gamma\, \tfrac{\hbar}{2}\, \bar{P}_\perp$$

Signal Shape of Polarization Measurement

The NMR coil is perpendicularly oriented to the polarization coil. The spins are exited by a high-frequency field ω_m around the hydrogen resonance $\omega_0 = \gamma_I \, B_0$ with magnitude $2\omega_1$.

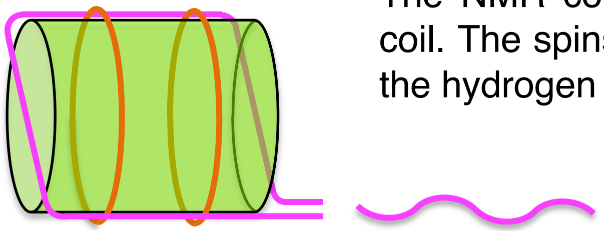

$$E_{\leftarrow} = 2\hbar\omega_1 \cos \omega_m t$$

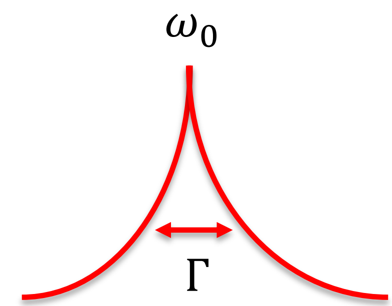

The induced spin precession adds the Lorentzian energy distribution $\Delta E_{\leftrightarrows}$ per cycle to the deflected wave.

$$\Delta E_{\leftrightarrows} = A \frac{2}{\pi \, \Gamma} \frac{1}{1 + \left(2 \, \frac{\omega_0 - \omega_m}{\Gamma}\right)^2}$$

For the a non-saturated ESR $\omega_1 \ll 1/\sqrt{\tau_1 \tau_2}$, the width Γ would equal the natural line width. In NMR, homogenous broadening leads to a Gaussian form.

$$\Gamma = \sqrt{1 + \tau_1 \tau_2 \omega_1^2} \; \frac{2}{\tau_2}$$

τ_1: spin-lattice relaxation time
τ_2: spin-spin relaxation time

The frequency integral A is directly proportional to the number of spins N in the sample and to their polarization P.

$$A = -2\pi \, \Omega \, \hbar\omega_1 \times N \, P \quad \text{with} \quad \Omega = \frac{\pi \, \omega_1}{\sqrt{1 + \tau_1 \tau_2 \omega_1^2}}$$

Maik Biroth, Institute of Nuclear Physics, Mainz, Germany
mbiroth@uni-mainz.de

The Solid Effect in Dynamic Nuclear Polarization

The solid effect is the 1st order mechanism in DNP.

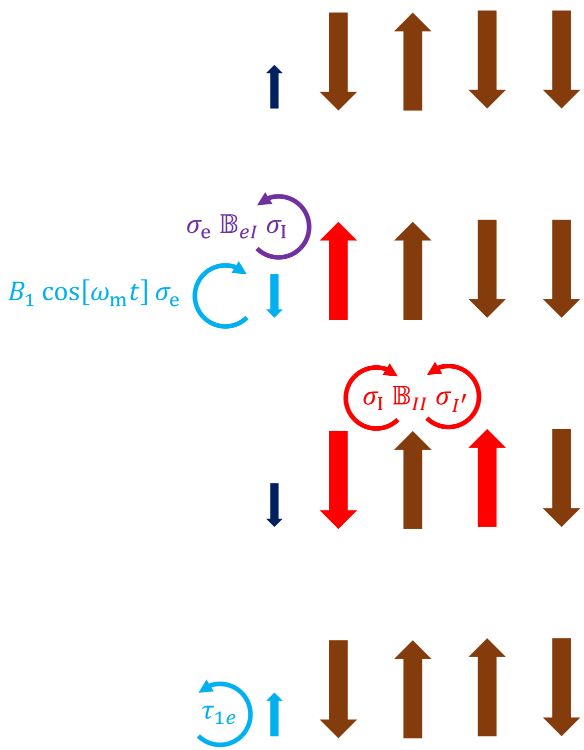

A hydrogen spin sample is doped with a paramagnetic free radical.

A microwave field induces a coupled e-H spin flip by super-hyperfine interaction.

Polarization spreads out by mutual H-H interaction.

The electron spin flips back by spin-lattice relaxation.

Maik Biroth, Institute of Nuclear Physics, Mainz, Germany

mbiroth@uni-mainz.de

Thermal Mixing in Dynamic Nuclear Polarization

If the nuclear gyromagnetic ratio is in the order of the ESR line, the polarization transfer by the solid effect is suppressed.

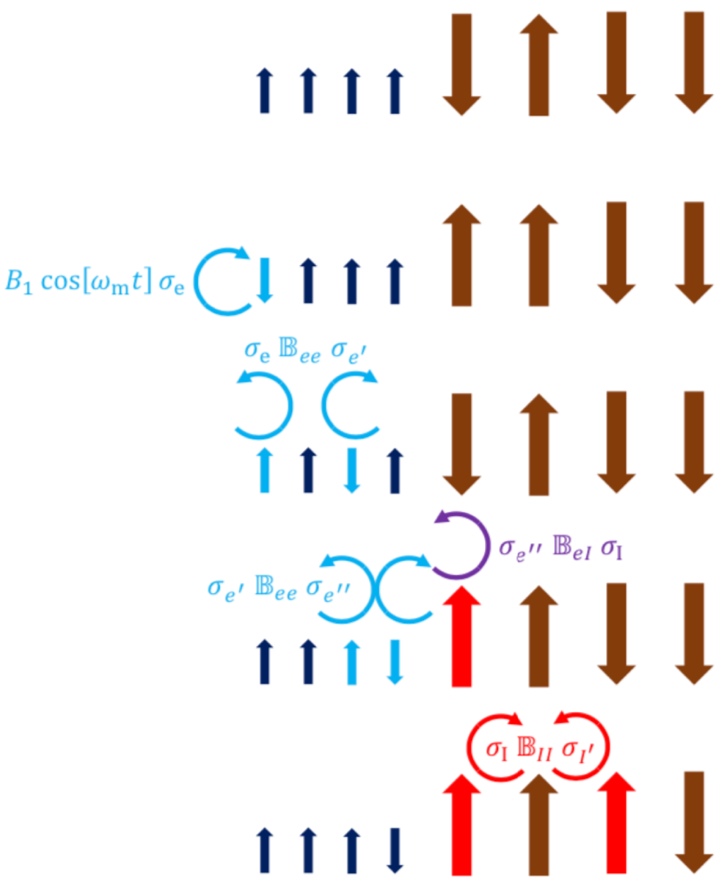

A hydrogen spin sample is doped with a paramagnetic free radical.

A microwave field flips an electron spin.
If electron spin diffusion is fast, the polarization spreads out over the spectrum.

Polarization is transferred to the nucleon off-resonance by a triple spin flip.

Polarization spreads out by mutual H-H interaction.

Maik Biroth, Institute of Nuclear Physics, Mainz, Germany mbiroth@uni-mainz.de

Anisotropy of the Electron's g-Tensor

$$\frac{g_\mathrm{e}-2}{2} = \frac{\alpha_\mathrm{em}}{2\pi} + \cdots = 1.160 \times 10^{-3}$$

The g-factor of a free electron g_e is calculatable by the QED. If free electron spins are embedded in a single-crystal, they show isotropic alignment under an applied magnetic field.

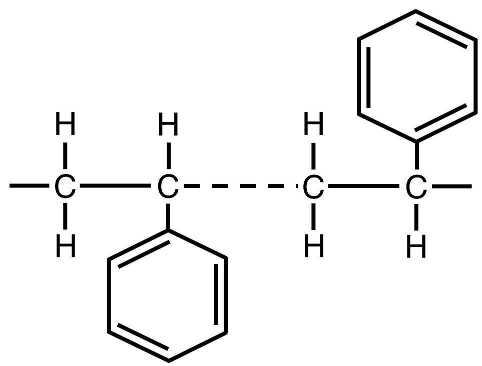

Amorphous Polystyrene is a glass, since the position of the Phenyl group is randomly distributed.

$$\frac{g_{jj}-2}{2} = \frac{\hbar\omega_\mathrm{m}}{2\,\mu_\mathrm{B}\,B_j} - 1 = \begin{pmatrix} 4.4 & & \\ & 2.9 & \\ & & 0.5 \end{pmatrix} 10^{-3}$$

It follows, resonance condition is degenerated. The resulting g-tensor g_{jj} is anisotropic and can be diagonalized in the principal axes B_j.

Fine-structure constant $\alpha_\mathrm{em} = e_0^2/4\pi\varepsilon_0\,\hbar c$, Bohr magneton $\mu_\mathrm{B} = e_0\hbar/2m_\mathrm{e}$,
Excitation frequency $\omega_\mathrm{m} = 2\pi \times 9.36303\ \mathrm{GHz}$

Hyperfine Interaction with a Spin-1 Atom

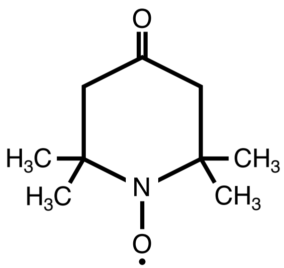

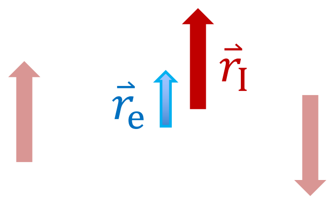

The radical 4-Oxo-TEMPO offers an unpaired electron spin $\vec{r}_{\mathrm{e}}$ at the nitroxide group, that is hyperfine-coupled to the spin-1 nitrogen $\vec{r}_{\mathrm{I}}$ in the distance $\vec{r} = \vec{r}_{\mathrm{I}} - \vec{r}_{\mathrm{e}}$.

The hyperfine Hamiltonian $\mathcal{H}_{\mathrm{HF}}$ can be described as an dipolar interaction using the symmetric magnetic field tensor $\mathbb{B}$.

$$\mathbb{B} \approx -\frac{\mu_0}{4\pi}\frac{\Gamma_{\mathrm{e}}}{r^3}\left(I_3 - 3\frac{\vec{r}\,\vec{r}}{r^2}\right)$$

$$= \begin{pmatrix} 0.5 & & \\ & 0.3 & \\ & & 3.2 \end{pmatrix} \mathrm{mT}$$

$$\mathcal{H}_{\mathrm{HF}} = -\vec{\sigma}_{\mathrm{e}}\,\hbar\mathbb{B}\,\gamma_{\mathrm{I}}\vec{\sigma}_{\mathrm{I}} \approx -m_{\mathrm{I}}\,\sigma_{\mathrm{e},z}\,\hbar\mathbb{B}_{zz}\,\gamma_{\mathrm{I}}$$

Its strong *zz*-component leads to characteristic discontinuities in the z-axis with the quantum numbers $m_{\mathrm{I}} \in [-1,0,+1]$ to the ^{14}N Eigenstates $|m_{\mathrm{I}}\rangle$.

Gyromagnetic ratio tensor $\Gamma_j = g_{jj}\,\mu_{\mathrm{B}}/\hbar$,
Bohr magneton $\mu_{\mathrm{B}} = e_0\hbar/2m_{\mathrm{e}}$,
Excitation frequency $\omega_{\mathrm{ESR}} = \Gamma_j\,B_j = 2\pi \times 9.36303\ \mathrm{GHz}$

Maik Biroth, Institute of Nuclear Physics, Mainz, Germany mbiroth@uni-mainz.de

Expected Polarization Growth

- Groth $\partial P/\partial t$ is initially proportional to the µWave power $\mathbb{P}_\mathrm{m}$
- Overlapping contributions cancel by the differential solid effect

$$\partial P/\partial t \propto \mathbb{P}_\mathrm{m}\, P_{\mathrm{TE,e}}\, (S_e[\omega_\mathrm{m} + \omega_\mathrm{H}] - S_e[\omega_\mathrm{m} - \omega_\mathrm{H}])$$

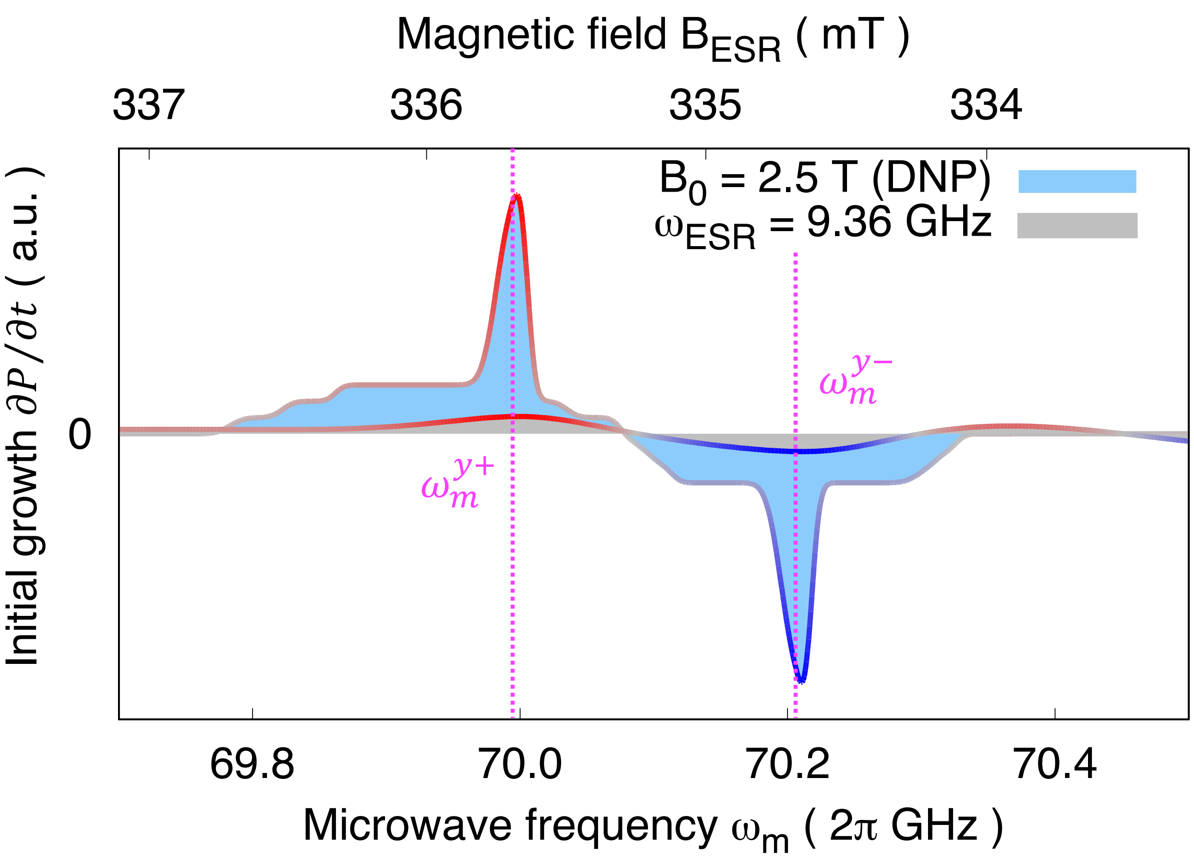

- *Y*-axis frequencies correspond to the known resonances

$$\omega_m^{y\pm} = (\Gamma_{\mathrm{e},yy} \mp \gamma_\mathrm{H})\, B_0 \cong \omega_m^{\pm}$$

- Polarization growth in high fields is superior

Maximum Achievable Polarization

The maximum achievable polarization P_∞ depends on the asymmetry of the overlapping spectrum contributions, reduced by the factor ξ.

$$P_\infty = P_{\mathrm{TE,e}} \frac{S_e[\omega_\mathrm{m} + \omega_\mathrm{H}] - S_e[\omega_\mathrm{m} - \omega_\mathrm{H}]}{S_e[\omega_\mathrm{m} + \omega_\mathrm{H}] + S_e[\omega_\mathrm{m} - \omega_\mathrm{H}] + \xi}$$

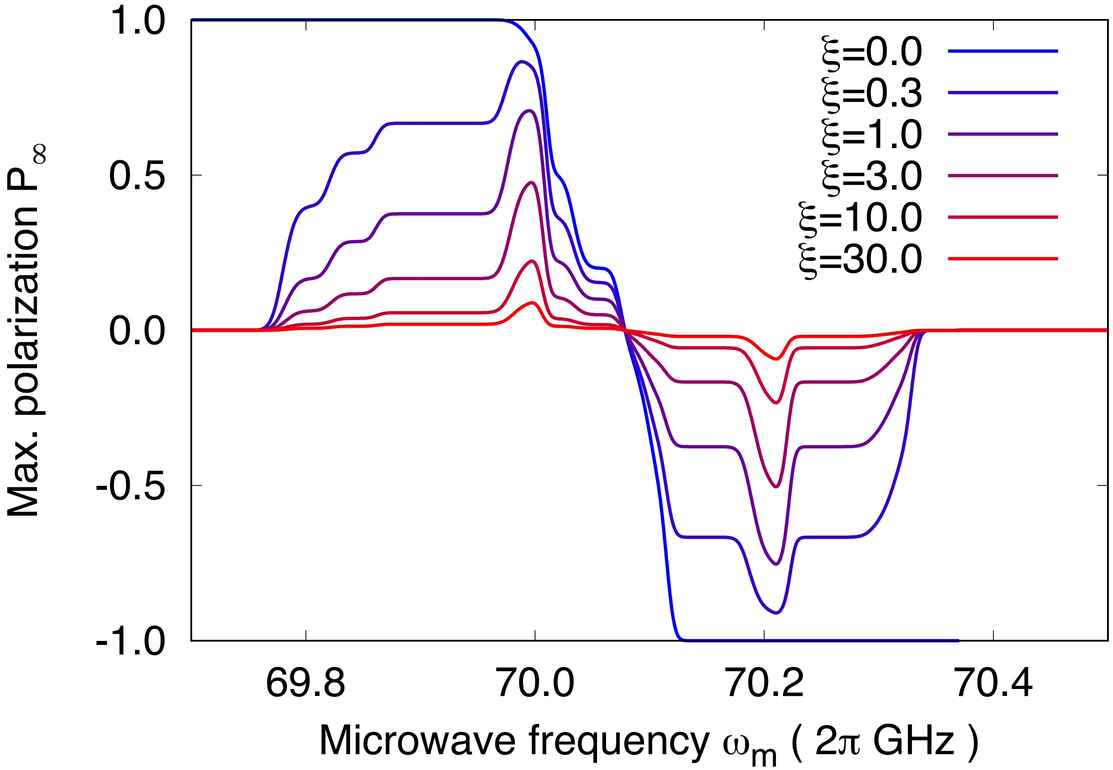

The factor ξ depends on the field, the temperature and the µWave power.

$$\xi \propto \frac{1 - P_{\mathrm{TE,e}}^2}{\tau_{1,\mathrm{e}}} \frac{1}{\mathbb{P}} \propto \frac{1 - P_{\mathrm{TE,e}}^2}{P_{\mathrm{TE,e}}} \frac{B_0^5}{\mathbb{P}}$$

$$P_{\mathrm{TE,e}} = \tanh \frac{\hbar\, \gamma_\mathrm{e}\, B_0}{2 k_\mathrm{B} T}$$

mbiroth@uni-mainz.de

Heat Input by Micro Wave Irradiation

The cryostat has the cooling power $\dot{Q}_c = \alpha\, T^2$, $\alpha = -\dot{n}_{3\mathrm{He}} \left(\frac{\Delta S}{T}\right) = 0.44\ \mu\mathrm{W\,mK}^{-2}$. The temperature T_m is expected to depend on the square root of the µWave power $\mathbb{P}_\mathrm{m}$. The measured temperature $\tilde{T}_\mathrm{m}$ shows a dependence of the power $1/n$ with $n = 3.4$ due to a bolometric voltage drop over the probe.

$$T_\mathrm{m} = \sqrt{T_0^2 + \mathbb{P}_\mathrm{m}/\alpha} \qquad \tilde{T}_\mathrm{m} = (T_0^n + \mathbb{P}_\mathrm{m}/\tilde{\alpha})^{1/n}$$

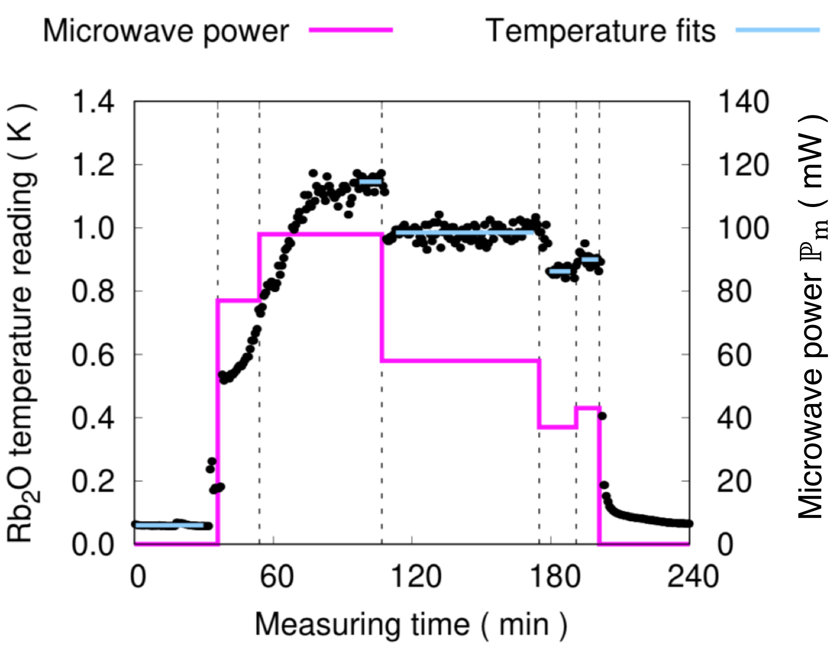

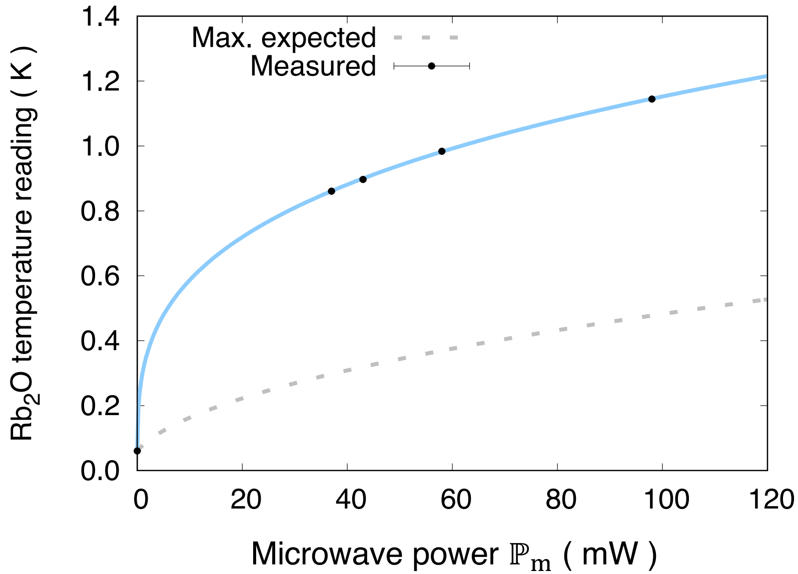

Power-off temperature $T_0 = 60$ mK, conversion factor $\tilde{\alpha} = 61.7\ \mathrm{mW\,K}^n$

Appendix – Energy Expansion of the Hamiltonian

Thomson Cross-section: 0th Order Energy Expansion

The 0th order Hamiltonian describes the scattering of a wave with the electromagnetic 4-potenial $A^\mu = \left(A_0 \, , \quad \vec{A} \right)$ off a particle with charge e_0 and mass m, resulting in the covariant momentum $\vec{\pi}$:

$$\mathscr{H}_{\text{eff}}^{(0)} = e_0 \; A_0 + \frac{1}{2\,m} \; \vec{\pi}^{\,2} \qquad\qquad \vec{\pi} = \vec{p} - e_0 \, \vec{A}$$

The measured cross-section is given by the Thomson cross-section, only depending on the scattering angle θ:

$$\left(\frac{d\sigma}{d\Omega}\right)_{\text{Thomson}} = \frac{1}{2} \left(\frac{e_0^2}{m}\right)^2 (1 + \cos^2\theta)$$

Powell Cross-section: 1th Order Energy Expansion

The 1th order Hamiltonian describes the scattering off a particle with anomalous magnetic moment κ and spin $\vec{\sigma}$. Therein, $\vec{E} = -\vec{\nabla} A_0 - \dot{\vec{A}}$ is the electrical and $\vec{H} = \vec{\nabla} \times \vec{A}$ the magnetic field.

$$\mathscr{H}_{\text{eff}}^{(1)} = -\frac{e_0(1+\kappa)}{2\,m}\,\vec{\sigma}\cdot\vec{H} - \frac{e_0(1+2\,\kappa)}{8\,m^2}\,\vec{\sigma}\cdot\left(\vec{E}\times\vec{\pi} - \vec{\pi}\times\vec{E}\right)$$

The corresponding Powell cross-section is the Born contribution.

$$\left(\frac{d\sigma}{d\Omega}\right)_{\text{Born}} = \frac{1}{2}\left(\frac{e_0^2}{m}\right)^2\left(\frac{\omega'}{\omega}\right)^2\Bigg(\frac{\omega}{\omega'} + \frac{\omega'}{\omega} - \sin^2\theta \quad = \text{Klein-Nishina cross-section}$$

$$+\kappa\,\frac{\omega\omega'}{m^2}\,2\,(1-\cos\theta)^2 + \kappa^2\,\frac{\omega\omega'}{m^2}\left\{4\,(1-\cos\theta) + \frac{1}{2}(1-\cos\theta)^2\right\}$$

$$+\kappa^3\,\frac{\omega\omega'}{m^2}\,\{2\,(1-\cos\theta) + (1-\cos\theta)^2\} + \kappa^4\,\frac{\omega\omega'}{m^2}\left\{1 + \frac{1}{2}(1-\cos\theta)^2\right\}\Bigg)$$

The 2th order Hamiltonian describes the response of the electric and magnetic density of the nucleon to static fields by the scalar polarizabilities, resulting in an electric $\vec{\varepsilon} = 4\pi\, \alpha_{\mathrm{E1}}\, \vec{E}$ and magnetic $\vec{\mu} = 4\pi\, \beta_{\mathrm{M1}}\, \vec{H}$ dipole moment.

$$\mathscr{H}_{\mathrm{eff}}^{(2)} = -\,4\,\pi \left(\frac{1}{2}\,\alpha_{\mathrm{E1}}\,\vec{E}^2 + \frac{1}{2}\,\beta_{\mathrm{M1}}\,\vec{H}^2 \right)$$

The polarized differential cross-section can be given in the Low Energy Expansion:

$$\left(\frac{d\sigma}{d\Omega}\right)_{\mathrm{LEX}} = \left(\frac{d\sigma}{d\Omega}\right)_{\mathrm{Born}} - \omega\omega' \left(\frac{\omega'}{\omega}\right)^2 \frac{e_0^2}{m} \left(\frac{\alpha_{\mathrm{E1}} + \beta_{\mathrm{M1}}}{2}\,(1+\cos\theta)^2 + \frac{\alpha_{\mathrm{E1}} - \beta_{\mathrm{M1}}}{2}\,(1-\cos\theta)^2 \right)$$

The Spin Polarizabilities: 3rd Order Energy Expansion

The 3th order Hamiltonian depends on the dynamics of the nucleon spin $\vec{\sigma}$ interacting with the fields $\vec{E}$ and $\vec{H}$ of the scattering photon.

$$\mathscr{H}_{\text{eff}}^{(3)} = -4\pi \left(\frac{1}{2}\gamma_{\text{E1E1}}\,\vec{\sigma}\cdot\left(\vec{E}\times\dot{\vec{E}}\right) + \frac{1}{2}\gamma_{\text{M1M1}}\,\vec{\sigma}\cdot\left(\vec{H}\times\dot{\vec{H}}\right) - \frac{1}{2}\gamma_{\text{M1}E2}\,\sigma_i\,H_j\left(\nabla_i E_j + \nabla_j E_i\right) + \frac{1}{2}\gamma_{\text{E1}M2}\,\sigma_i\,E_j\left(\nabla_i H_j + \nabla_j H_i\right)\right)$$

The spin polarizabilities are proportional to the direction and magnitude of the excited spin precession.

Multipole expansion	El-photon	Ml-photon
Change in parity	$P_\text{f} = P_\text{i}\,(-1)^l$	$P_\text{f} = P_\text{i}\,(-1)^{l+1}$
Change in angular momentum	$\lvert j_\text{i} - j_\text{f}\rvert \le l \le j_\text{i} + j_\text{f}$	
Transition probability	$W_\text{fi} = \frac{1}{\tau} \propto E_\gamma^{2l+1}$	

Energy Dependence of the Spin-polarizabilities

Center-of-mass photon energy:

$$\omega_{\mathrm{CM}} = m_{\mathrm{p}}\,\gamma_{\mathrm{CM}}\,\beta_{\mathrm{CM}} = m_{\mathrm{p}}\frac{E_{\gamma 0}}{\sqrt{s}}$$

$$E_{\gamma 0} = 300\ \mathrm{MeV} \rightarrow \omega_{\mathrm{CM}} = 234\ \mathrm{MeV}$$

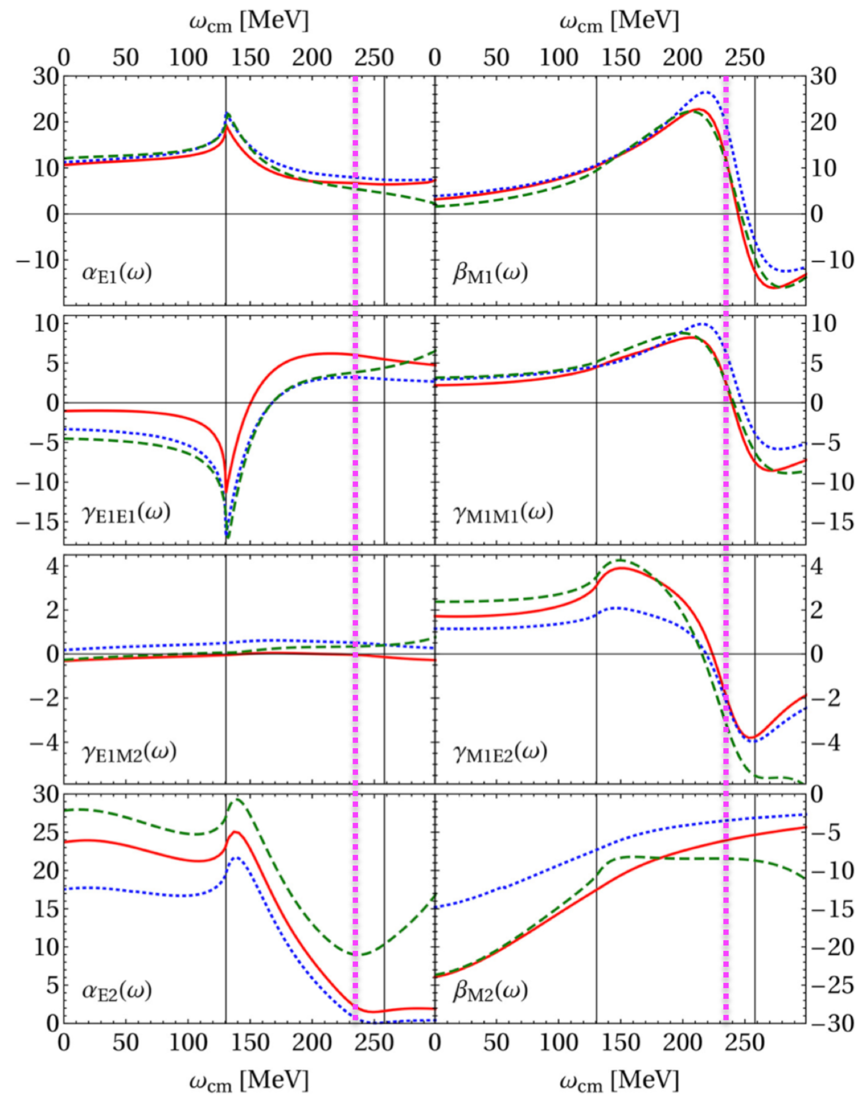

Center-of-mass energy:

$$s = m_{\mathrm{p}}\left(m_{\mathrm{p}} + 2\,E_{\gamma 0}\right)$$

Center-of-mass velocity:

$$\beta_{\mathrm{CM}} = \frac{E_{\gamma 0}}{m_{\mathrm{p}} + E_{\gamma 0}}$$

H.W. Grießhammer, et al., Eur. Phys. J. A 54 (2018) 37

Forward and Backward Spin Polarizabilities

The forward and backward γ_0, γ_π spin polarizabilities shrink the parameter space, since they are linear combinations of $\gamma_{E1E1}, \gamma_{M1M1}, \gamma_{E1M2}, \gamma_{M1E2}$.

Forward spin polarizability (J. Ahrens 2001, H. Dutz 2003)

$$\gamma_0 = -\gamma_{E1E1} - \gamma_{M1M1} - \gamma_{E1M2} - \gamma_{M1E2} = -\frac{1}{4\pi^2}\int_0^\infty \mathrm{d}\omega \, \frac{\sigma_{3/2} - \sigma_{1/2}}{\omega^3}$$ (Gerasimov-Drell-Hearn sum rule)

Backward spin polarizability (M. Camen 2002, dispersion analysis of Compton $\theta_\gamma^{CM} = 135°$)

$$\gamma_\pi = \gamma_\pi^{\pi P} + \gamma_\pi^{disp} \qquad \gamma_\pi^{disp} = -\gamma_{E1E1} + \gamma_{M1M1} - \gamma_{E1M2} + \gamma_{M1E2}$$ (dispersive contribution)

	Prediction		Experiment
	HDPV	BχPT	
γ_0	-0.8	-1.0	-1.01 ± 0.08 ± 0.10
γ_π^{disp}	9.4	7.2	8.0 ± 1.8

All values are in units of 10^{-4} fm^4

$\gamma_\pi = -38.7 \times 10^{-4}$ fm^4 without subtraction of the pion-pole $\gamma_\pi^{\pi P} = -46.7 \times 10^{-4}$ fm^4

Pion Pole Contribution to the Cross-section

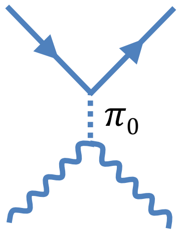

For larger angles and energies $\omega \geq 50\,\mathrm{MeV}$, a pole in the Mandelstam t-channel at the neutral pion mass m_π becomes dominant. This leads to the the pion-pole contribution to the Compton scattering cross-section.

$$\left(\frac{d\sigma}{d\Omega}\right)_{\pi\mathrm{P}} = \frac{2B(B+E)}{m_\pi^2}\,\frac{\omega\omega'}{m^2}\left(\frac{\omega'}{\omega}\right)^2 (1-\cos\theta)$$

$$B = \frac{m_\pi}{16\pi}\, g_{\pi\mathrm{NN}}\, F_{\pi\gamma\gamma}\, \frac{t}{m_\pi^2 - t}$$

$$E = \frac{e_0^2}{m}\frac{m_\pi}{2}\left(\kappa^2 + 2\kappa + (1+\kappa)\,(1-\cos\theta)\right)$$

Maik Biroth, Institute of Nuclear Physics, Mainz, Germany mbiroth@uni-mainz.de

Appendix – T-matrix and Polarizabilities

(Double-)Polarized Transition Matrix

The (double-)polarized T-matrix can be decomposed in eight independent functions W_{ij}. Six of these are relevant below the pion threshold.

The photon polarization is expressed by the Stokes vector $\vec{\xi}$ and the nucleon polarization by the four-vector S^μ.

$$|T|^2 = W_{00} + \xi_3 W_{03} + K_\mu S^\mu (\xi_1 W_{11} + \xi_2 W_{12}) + Q_\mu S^\mu (\xi_1 W_{21} + \xi_2 W_{22}) + \cdots$$

with the four-momenta $Q = -(p^{\gamma 0} - p^{\gamma})/2$ and $K = (p^{\gamma 0} + p^{\gamma})/2$

Circular polarization: $$|T|^2_{\mathrm{circ}}/W_{00} = 1 + \xi_2 \frac{K_\mu S^\mu\, W_{12} + Q_\mu S^\mu\, W_{22}}{W_{00}}$$

Linear polarization: $$|T|^2_{\mathrm{lin}}/W_{00} = 1 + \xi_1 \frac{K_\mu S^\mu\, W_{11} + Q_\mu S^\mu\, W_{21}}{W_{00}} + \xi_3 \frac{W_{03}}{W_{00}}$$

The eight functions W_{ij} can be related to six structure functions A_i fulfilling each a unsubtracted dispersion relation.

Stokes vector $\vec{\xi}$: linear polarization $\xi_3 = \pm 1$ (para. / perp.), or $\xi_1 = \pm 1$ ($\pm 45°$), circular polarization $\xi_2 = \pm 1$ (right / left handed)
xz-scattering plane: $Q^\mu = -\frac{1}{2}\begin{pmatrix} E_{\gamma 0} - E_\gamma & -E_\gamma \sin\theta_\gamma & 0 & E_{\gamma 0} - E_\gamma \cos\theta_\gamma \end{pmatrix}^T$ and $K^\mu = \frac{1}{2}\begin{pmatrix} E_{\gamma 0} + E_\gamma & E_\gamma \sin\theta_\gamma & 0 & E_{\gamma 0} + E_\gamma \cos\theta_\gamma \end{pmatrix}^T$

(Double-)Polarized Compton Asymmetries

The six independent functions can be determined by the (double-)polarized Compton asymmetries, whereby $(\varepsilon_\parallel \quad \varepsilon_\perp) = \left(E_\gamma / E_{\gamma 0}\right) (\cos\theta_\gamma \quad \sin\theta_\gamma)$ was used.

Linear / circular beam ($i = 1, 2$), transverse target:

$$\vec{\xi} = \pm\vec{e}_i \,, S^\mu = \pm\vec{e}_x \qquad \Sigma_{ix} = \frac{\sigma_\uparrow - \sigma_\downarrow}{\sigma_\uparrow + \sigma_\downarrow} = -\frac{E_{\gamma 0}}{2\, W_{00}} \varepsilon_\perp (W_{1i} + W_{2i})$$

Linear / circular beam ($i = 1, 2$), longitudinal target:

$$\vec{\xi} = \pm\vec{e}_i \,, S^\mu = \pm\vec{e}_z \qquad \Sigma_{iz} = \frac{\sigma_\rightarrow - \sigma_\leftarrow}{\sigma_\rightarrow + \sigma_\leftarrow} = -\frac{E_{\gamma 0}}{2\, W_{00}} \varepsilon_\parallel (W_{1i} + W_{2i}) - \frac{E_{\gamma 0}}{2\, W_{00}} (W_{1i} - W_{2i})$$

$$\frac{1}{W_{00}} \begin{pmatrix} W_{1i} \\ W_{2i} \end{pmatrix} = -\frac{1}{E_{\gamma 0}} \begin{pmatrix} (1 - \varepsilon_\parallel)/\varepsilon_\perp & 1 \\ (1 + \varepsilon_\parallel)/\varepsilon_\perp & -1 \end{pmatrix} \begin{pmatrix} \Sigma_{ix} \\ \Sigma_{iz} \end{pmatrix}$$

Linear beam, unpolarized target:

$$\vec{\xi} = \pm\vec{e}_3 \,, S^\mu = 0 \qquad \Sigma_3 = \frac{\sigma_\parallel - \sigma_\perp}{\sigma_\parallel + \sigma_\perp} = \frac{W_{03}}{W_{00}}$$

Dispersion Relations from the Cauchy Integral

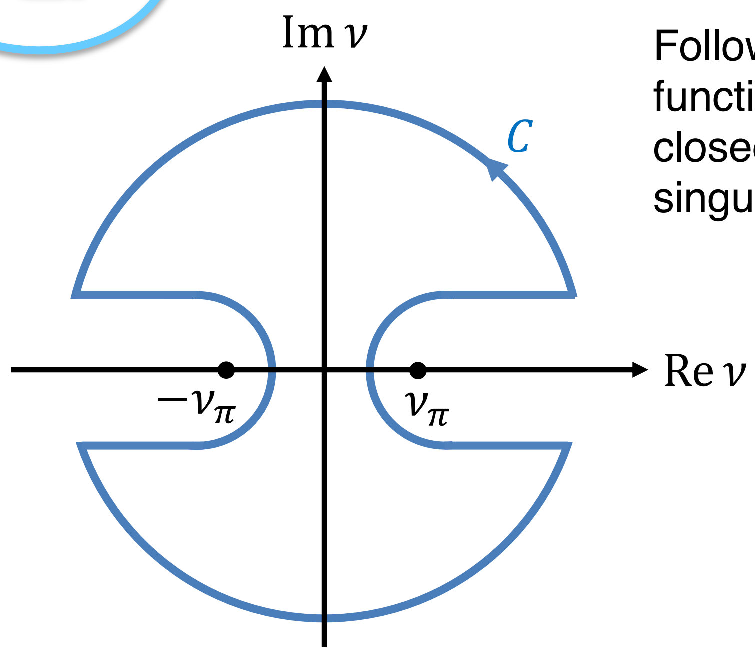

Following Cauchy's integral formula, a holomorphic function A is given by its integral over the border C of a closed disk. The integral simplifies for only real singularities ν_π with the Cauchy principal value $\mathcal{P}$.

$$A[\nu] = \frac{1}{2\pi\, i} \oint_C \mathrm{d}\nu' \, \frac{A[\nu']}{\nu' - \nu}$$

$$\overset{\nu_\pi \in \mathbb{R}}{=} \frac{1}{\pi\, i}\, \mathcal{P} \int_{-\infty}^{\infty} \mathrm{d}\nu' \, \frac{A[\nu']}{\nu' - \nu}$$

Splitting $A = \mathrm{Re}\, A[\nu] + i\, \mathrm{Im}\, A[\nu]$ in its real an imaginary part leads to the dispersion relations.

$$A[\nu] = \overbrace{\frac{1}{\pi}\, \mathcal{P} \int_{-\infty}^{\infty} \mathrm{d}\nu' \, \frac{\mathrm{Im}\, A[\nu']}{\nu' - \nu}}^{=\mathrm{Re}\, A[\nu]} + i \overbrace{\left(-\frac{1}{\pi}\, \mathcal{P} \int_{-\infty}^{\infty} \mathrm{d}\nu' \, \frac{\mathrm{Re}\, A[\nu']}{\nu' - \nu} \right)}^{=\mathrm{Im}\, A[\nu]}$$

Crossing-symmetric Dispersion Relations

The dispersion integrals can be expanded between the poles $\pm\nu_\pi$, exemplary:

$$\operatorname{Re} A[\nu] = \frac{1}{\pi}\,\mathcal{P}\int_{-\infty}^{-\nu_\pi} \mathrm{d}\nu' \,\frac{\operatorname{Im} A[\nu']}{\nu' - \nu} + \overbrace{\frac{1}{\pi}\,\mathcal{P}\int_{-\nu_\pi}^{\nu_\pi} \mathrm{d}\nu' \,\frac{\operatorname{Im} A[\nu']}{\nu' - \nu}}^{=0} + \frac{1}{\pi}\,\mathcal{P}\int_{\nu_\pi}^{\infty} \mathrm{d}\nu' \,\frac{\operatorname{Im} A[\nu']}{\nu' - \nu}$$

In case of crossing symmetry $A[\nu] \equiv A^*[-\nu]$, the integral is positive in ν.

$$\operatorname{Re} A[\nu] = \frac{1}{\pi}\,\mathcal{P}\int_{\nu_\pi}^{\infty} \mathrm{d}\nu' \,\frac{\operatorname{Im} A[\nu']}{\nu' + \nu} + \frac{1}{\pi}\,\mathcal{P}\int_{\nu_\pi}^{\infty} \mathrm{d}\nu' \,\frac{\operatorname{Im} A[\nu']}{\nu' - \nu} = \frac{2}{\pi}\,\mathcal{P}\int_{\nu_\pi}^{\infty} \mathrm{d}\nu' \,\frac{\nu' \operatorname{Im} A[\nu']}{\nu'^2 - \nu^2}$$

The same appears for the corresponding dispersion relation.

$$\operatorname{Im} A[\nu] = -\frac{2\,\nu}{\pi}\,\mathcal{P}\int_{\nu_\pi}^{\infty} \mathrm{d}\nu' \,\frac{\operatorname{Re} A[\nu']}{\nu'^2 - \nu^2}$$

Transition Matrix from Dispersion Relations

The Compton T-matrix consists of six structure functions A_i, each fulfills a unsubtracted dispersion relation at fixed-t with the nucleon pole contribution of the Born terms A_i^{B}. A subtraction at $\nu = 0$ leads to convergence for all A_i.

$$\mathrm{Re}\, A_i = A_i^{\mathrm{B}} + \frac{2}{\pi}\, \mathcal{P} \int_{\nu_\pi}^{\infty} \mathrm{d}\nu' \, \frac{\nu' \, \mathrm{Im}_s \, A_i}{\nu'^2 - \nu^2} = A_i^{\mathrm{B}} + \left(A_i - A_i^{\mathrm{B}}\right)_{\nu=0} + \frac{2\,\nu^2}{\pi}\, \mathcal{P} \int_{\nu_\pi}^{\infty} \mathrm{d}\nu' \, \frac{\mathrm{Im}_s \, A_i}{\nu'(\nu'^2 - \nu^2)}$$

The constants a_i are the projections of the subtraction to zero-momentum transfer $t \to 0$:

$$\left(A_i - A_i^{\mathrm{B}}\right)_{\nu=0} = \overbrace{\left(A_i - A_i^{\mathrm{B}}\right)_{\nu=0,\; t=0}}^{\stackrel{\mathrm{def}}{=} a_i} + \cdots$$

The model dependence of extracting the (spin-)polarizabilities vanishes for $t \to 0$ since they are expressed as linear combinations of a_i.

$$\alpha_{\mathrm{E1}} = -\left(a_1 + a_3 + a_6\right)/4\pi \qquad \beta_{\mathrm{M1}} = \left(a_1 - a_3 - a_6\right)/4\pi$$

$$\gamma_{\mathrm{E1E1}} = \left(a_2 - a_4 + 2a_5 + a_6\right)/8\pi\, m_{\mathrm{N}} \qquad \gamma_{\mathrm{M1M1}} = -\left(a_2 + a_4 + 2a_5 - a_6\right)/8\pi\, m_{\mathrm{N}}$$

$$\gamma_{\mathrm{E1M2}} = \left(a_2 - a_4 - a_6\right)/8\pi\, m_{\mathrm{N}} \qquad \gamma_{\mathrm{M1E2}} = -\left(a_2 + a_4 + a_6\right)/8\pi\, m_{\mathrm{N}}$$

Mandelstam variable $s = \left(p^{\gamma_0} + p^{\mathrm{N}_0}\right)^2$, $t = (p^{\gamma_0} - p^{\gamma})^2$, $u = \left(p^{\gamma_0} - p^{\mathrm{N}}\right)^2$, Crossing-symmetric variable $\nu = (s-u)/4m = \left(E_{\gamma_0} + E_\gamma\right)/2$

See: B.Pasquini, D. Drechsel, M. Vanderhaeghen, Phys. Rev. C 76 (2007) 015203, R.E. Prange, Phys. Rev. 110 (1958) 240-252

Appendix – Partial Wave Analysis

An incoming plane wave ψ scatters off an potential V.

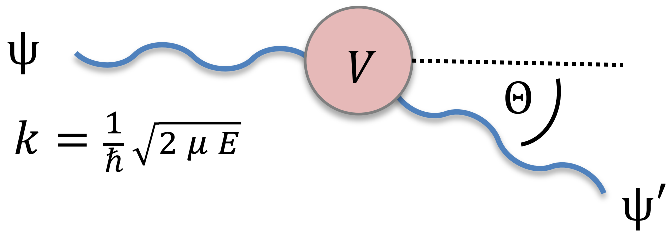

$$\left(-\frac{\hbar^2}{2\,\mu}\left(\vec{\nabla}^2 + k^2\right) + V\right)(\psi + \psi') = 0$$

The incoming wave is decomposed in partial waves with angular momentum l. Assuming the nucleon potential $V \equiv V[|\vec{r}|]$ as spherically symmetric, the asymptotic final state is a spherical wave ψ' with the scattering amplitude F.

$$\psi = \mathrm{e}^{\mathrm{i}\,k\,r} = \sum_{l=0}^{\infty} (2l+1)\,\mathrm{i}^l\, j_l[k\,r']\;P_l[\cos\Theta] \qquad \psi' = \frac{F[k,k',\Theta]}{r'}\,\mathrm{e}^{\mathrm{i}\,k\,r'}$$

Spherical Bessel $j_l[x] = (-x)^l\,(1/x\;\partial_x)^l\,\sin x/x$, Legendre polynomial $P_l^m[x] = 1/2^l l!\,\left(-\sqrt{1-x^2}\right)^m\,\partial_x^{l+m}\,(x^2-1)^l$
Spherical harmonics $Y_l^m[\Theta,\varphi] \propto \mathrm{e}^{\mathrm{i}\,m\varphi}P_l^m[\cos\Theta]$

Each outgoing partial wave is modified by scattering due to the partial wave amplitude f_l with the S-matrix element $S_l = \mathrm{e}^{2\mathrm{i}\,\delta_l}$ and the scattering phase δ_l.

$$F[k,k',\Theta] = \sum_{l=0}^{\infty}(2l+1)\,f_l[k,k']\,\mathcal{L}_l[\cos\Theta] \qquad f_l[k,k'] = \frac{1}{k}\,\frac{S_l-1}{2\mathrm{i}} = \frac{1}{k}\,\mathrm{e}^{\mathrm{i}\delta_l}\,\sin\delta_l$$

Maik Biroth, Institute of Nuclear Physics, Mainz, Germany
mbiroth@uni-mainz.de

Virtual States and Resonances in PWA

Virtual state

For δ_0 one obtains neutral scattering off a virtual state.

$$\delta_0 = -\tan^{-1} \lambda\, k'$$

S_0 shows a pole on the negative imaginary axis for a wave number $k' = \mathrm{i}/\lambda$ equal to one over the scattering length λ.

$$S_0 = -\,\frac{k' + \mathrm{i}/\lambda}{k' - \mathrm{i}/\lambda}$$

Example: Coherent scattering.

Resonance with angular momentum l

δ_l leads to a Breit-Wigner form of the differential cross-section if the background phase shift $\delta_{l,0}$ vanishes.

$$\delta_l = \delta_{l,0} + \tan^{-1} \frac{\Gamma_l/2}{E_l - E'}$$

S_l shows a pole for the resonance condition $E' \equiv E_l - \mathrm{i}\,\Gamma_l/2$.

$$S_l = \mathrm{e}^{2\mathrm{i}\,\delta_{l,0}} \frac{E' - (E_l + \mathrm{i}\,\Gamma_l/2)}{E' - (E_l - \mathrm{i}\,\Gamma_l/2)}$$

The lifetime τ_l is set by the width Γ_l.

$$\tau_l = -\hbar \frac{\mathrm{d}}{\mathrm{d}E'} \delta_l = \frac{2\,\hbar}{\Gamma_l} \left(1 + \left(\frac{E' - E_l}{\Gamma_l\,/\,2} \right)^2 \right)^{-1}$$

Differential and Total Cross-section in PWA

The differential cross-section $\mathrm{d}\sigma/\mathrm{d}\Omega$ is sensitive to interferences between partial waves.

$$\frac{\mathrm{d}\sigma}{\mathrm{d}\Omega}[k,\Theta] = |F[k,k',\Theta]|^2$$

The total cross-section σ is obtained by integration over the solid angle $\mathrm{d}\Omega$ and simplifies due to the orthogonality $\int \mathrm{d}\Omega\, P_l P_{l'} \equiv 4\pi\, \delta_{ll'}/(2l+1)$ of the Legendre polynomials. Interferences do not occur since coherence of partial waves is lost.

$$\sigma[k,k'] = 4\pi \sum_{l=0}^{\infty}(2l+1)\,|f_l[k,k']|^2 = \frac{4\pi}{k^2}\sum_{l=0}^{\infty}(2l+1)\ \sin^2\delta_l$$

The imaginary part of the forward scattering amplitude is related to the total cross-section by the optical theorem and implies particle conservation.

$$\frac{k}{4\pi}\,\sigma[k,k'] = \mathrm{Im}\,F[k,k',0] = \frac{1}{k}\sum_{l=0}^{\infty}(2l+1)\sin^2\delta_l$$